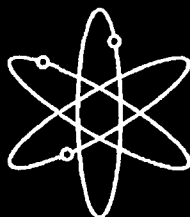


# Environmentally Assisted Cracking in Light Water Reactors



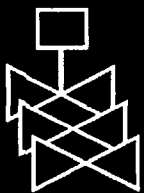
**Annual Report  
January—December 2004**



**Argonne National Laboratory**



**U.S. Nuclear Regulatory Commission  
Office of Nuclear Regulatory Research  
Washington, DC 20555-0001**



## AVAILABILITY OF REFERENCE MATERIALS IN NRC PUBLICATIONS

### NRC Reference Material

As of November 1999, you may electronically access NUREG-series publications and other NRC records at NRC's Public Electronic Reading Room at <http://www.nrc.gov/reading-rm.html>. Publicly released records include, to name a few, NUREG-series publications; *Federal Register* notices; applicant, licensee, and vendor documents and correspondence; NRC correspondence and internal memoranda; bulletins and information notices; inspection and investigative reports; licensee event reports; and Commission papers and their attachments.

NRC publications in the NUREG series, NRC regulations, and *Title 10, Energy*, in the Code of *Federal Regulations* may also be purchased from one of these two sources.

1. The Superintendent of Documents  
U.S. Government Printing Office  
Mail Stop SSOP  
Washington, DC 20402-0001  
Internet: [bookstore.gpo.gov](http://bookstore.gpo.gov)  
Telephone: 202-512-1800  
Fax: 202-512-2250
2. The National Technical Information Service  
Springfield, VA 22161-0002  
[www.ntis.gov](http://www.ntis.gov)  
1-800-553-6847 or, locally, 703-605-6000

A single copy of each NRC draft report for comment is available free, to the extent of supply, upon written request as follows:

Address: U.S. Nuclear Regulatory Commission  
Office of Administration  
Mail, Distribution and Messenger Team  
Washington, DC 20555-0001

E-mail: [DISTRIBUTION@nrc.gov](mailto:DISTRIBUTION@nrc.gov)  
Facsimile: 301-415-2289

Some publications in the NUREG series that are posted at NRC's Web site address <http://www.nrc.gov/reading-rm/doc-collections/nuregs> are updated periodically and may differ from the last printed version. Although references to material found on a Web site bear the date the material was accessed, the material available on the date cited may subsequently be removed from the site.

### Non-NRC Reference Material

Documents available from public and special technical libraries include all open literature items, such as books, journal articles, and transactions, *Federal Register* notices, Federal and State legislation, and congressional reports. Such documents as theses, dissertations, foreign reports and translations, and non-NRC conference proceedings may be purchased from their sponsoring organization.

Copies of industry codes and standards used in a substantive manner in the NRC regulatory process are maintained at—

The NRC Technical Library  
Two White Flint North  
11545 Rockville Pike  
Rockville, MD 20852-2738

These standards are available in the library for reference use by the public. Codes and standards are usually copyrighted and may be purchased from the originating organization or, if they are American National Standards, from—

American National Standards Institute  
11 West 42<sup>nd</sup> Street  
New York, NY 10036-8002  
[www.ansi.org](http://www.ansi.org)  
212-642-4900

Legally binding regulatory requirements are stated only in laws; NRC regulations; licenses, including technical specifications; or orders, not in NUREG-series publications. The views expressed in contractor-prepared publications in this series are not necessarily those of the NRC.

The NUREG series comprises (1) technical and administrative reports and books prepared by the staff (NUREG-XXXX) or agency contractors (NUREG/CR-XXXX), (2) proceedings of conferences (NUREG/CP-XXXX), (3) reports resulting from international agreements (NUREG/IA-XXXX), (4) brochures (NUREG/BR-XXXX), and (5) compilations of legal decisions and orders of the Commission and Atomic and Safety Licensing Boards and of Directors' decisions under Section 2.206 of NRC's regulations (NUREG-0750).

**DISCLAIMER:** This report was prepared as an account of work sponsored by an agency of the U.S. Government. Neither the U.S. Government nor any agency thereof, nor any employee, makes any warranty, expressed or implied, or assumes any legal liability or responsibility for any third party's use, or the results of such use, of any information, apparatus, product, or process disclosed in this publication, or represents that its use by such third party would not infringe privately owned rights.

# Environmentally Assisted Cracking in Light Water Reactors

Annual Report  
January—December 2004

---

---

Manuscript Completed: September 2005  
Date Published: November 2006

Prepared by  
B. Alexandreanu, O. K. Chopra, H. M. Chung,  
E. E. Gruber, W. K. Soppet, and W. J. Shack

Argonne National Laboratory  
9700 South Cass Avenue  
Argonne, IL 60439

W. H. Cullen, Jr., NRC Project Manager

Prepared for  
Division of Fuel, Engineering and Radiological Research  
Office of Nuclear Regulatory Research  
U.S. Nuclear Regulatory Commission  
Washington, DC 20555-0001  
NRC Job Code Y6388



## Previous Documents in Series

---

*Environmentally Assisted Cracking in Light Water Reactors Semiannual Report*  
April–September 1985, NUREG/CR-4667 Vol. I, ANL-86-31 (June 1986).  
October 1985–March 1986, NUREG/CR-4667 Vol. II, ANL-86-37 (September 1987).  
April–September 1986, NUREG/CR-4667 Vol. III, ANL-87-37 (September 1987).  
October 1986–March 1987, NUREG/CR-4667 Vol. IV, ANL-87-41 (December 1987).  
April–September 1987, NUREG/CR-4667 Vol. V, ANL-88-32 (June 1988).  
October 1987–March 1988, NUREG/CR-4667 Vol. 6, ANL-89/10 (August 1989).  
April–September 1988, NUREG/CR-4667 Vol. 7, ANL-89/40 (March 1990).  
October 1988–March 1989, NUREG/CR-4667 Vol. 8, ANL-90/4 (June 1990).  
April–September 1989, NUREG/CR-4667 Vol. 9, ANL-90/48 (March 1991).  
October 1989–March 1990, NUREG/CR-4667 Vol. 10, ANL-91/5 (March 1991).  
April–September 1990, NUREG/CR-4667 Vol. 11, ANL-91/9 (May 1991).  
October 1990–March 1991, NUREG/CR-4667 Vol. 12, ANL-91/24 (August 1991).  
April–September 1991, NUREG/CR-4667 Vol. 13, ANL-92/6 (March 1992).  
October 1991–March 1992, NUREG/CR-4667 Vol. 14, ANL-92/30 (August 1992).  
April–September 1992, NUREG/CR-4667 Vol. 15, ANL-93/2 (June 1993).  
October 1992–March 1993, NUREG/CR-4667 Vol. 16, ANL-93/27 (September 1993).  
April–September 1993, NUREG/CR-4667 Vol. 17, ANL-94/26 (June 1994).  
October 1993–March 1994, NUREG/CR-4667 Vol. 18, ANL-95/2 (March 1995).  
April–September 1994, NUREG/CR-4667 Vol. 19, ANL-95/25 (September 1995).  
October 1994–March 1995, NUREG/CR-4667 Vol. 20, ANL-95/41 (January 1996).  
April–December 1995, NUREG/CR-4667 Vol. 21, ANL-96/1 (July 1996).  
January 1996–June 1996, NUREG/CR-4667 Vol. 22, ANL-97/9 (June 1997).  
July 1996–December 1996, NUREG/CR-4667 Vol. 23, ANL-97/10 (October 1997).  
January 1997–June 1997, NUREG/CR-4667 Vol. 24, ANL-98/6 (April 1998).  
July 1997–December 1997, NUREG/CR-4667 Vol. 25, ANL-98/18 (September 1998).  
January 1998–June 1998, NUREG/CR-4667 Vol. 26, ANL-98/30 (December 1998).  
July 1998–December 1998, NUREG/CR-4667 Vol. 27, ANL-99/11 (October 1999).  
January 1999–June 1999, NUREG/CR-4667 Vol. 28, ANL-00/7 (July 2000).  
July 1999–December 1999, NUREG/CR-4667 Vol. 29, ANL-00/23 (November 2000).  
January 2000–June 2000, NUREG/CR-4667 Vol. 30, ANL-01/08 (June 2001).  
July 2000–December 2000, NUREG/CR-4667 Vol. 31, ANL-01/09 (April 2002).  
*Environmentally Assisted Cracking in Light Water Reactors Annual Report*  
January–December 2001, NUREG/CR-4667 Vol. 32, ANL-02/33 (June 2003).  
January–December 2002, NUREG/CR-4667 Vol. 33, ANL-03/36 (June 2005).  
January–December 2003, NUREG/CR-4667 Vol. 34, ANL-05/17 (May 2006).

## Abstract

This report summarizes work performed from January to December 2004 by Argonne National Laboratory on fatigue and environmentally assisted cracking (EAC) in light water reactors (LWRs). Topics that have been investigated include: (a) environmental effects on fatigue crack initiation in carbon and low-alloy steels and austenitic stainless steels (SSs), (b) irradiation-assisted stress corrosion cracking (IASCC) of austenitic SSs in boiling water reactors (BWRs), (c) causes and mechanisms of irradiation-assisted cracking of austenitic SS in pressurized water reactors (PWRs), and (d) cracking in Ni alloys and welds.

The existing fatigue strain vs. life data are used to establish the effects of various material and loading parameters, such as steel type, material heat treatment, strain range, strain rate, temperature, dissolved-oxygen (DO) level in water, and flow rate, on the fatigue lives of the steels. Statistical models are presented for estimating the fatigue curves as a function of material, loading, and environmental parameters. Methods are described for incorporating environmental effects into the fatigue evaluations of the American Society of Mechanical Engineers (ASME) Code.

The susceptibility of austenitic SSs and their welds to IASCC as a function of the fluence level, water chemistry, material chemistry, and fabrication history is being evaluated. The slow strain rate tensile test results obtained in the present study on steels irradiated to  $\approx 0.45$ , 1.35, and 3.0 dpa are compared with data available in the literature. The bulk S content provided the only good correlation with the susceptibility to IGSCC in 289°C water. A two-dimensional map of bulk S and C contents is presented to show the range in which austenitic SSs are either susceptible or resistant to IASCC. Based on the results of this study, an IASCC model has been proposed.

Crack growth rate (CGR) data are presented on Types 304L and 304 SS weld specimens from the heat affected zone (HAZ) before and after they were irradiated to a fluence of  $\approx 0.75$  dpa. Tests were conducted under cyclic loading and long hold-time trapezoidal loading in simulated BWR environments on Type 304L SS HAZ of the H5 weld from the Grand Gulf reactor core shroud and on Type 304 SS HAZ of a laboratory-prepared weld. The effects of material composition, irradiation, and water chemistry on growth rates are discussed.

Crack growth rate data, obtained in PWR environment, are also presented for Alloy 600 removed from the control rod drive mechanism (CRDM) nozzle #3 from the Davis-Besse reactor and Alloys 182 and 82 from the nozzle-to-pipe weld of the V. C. Summer reactor. The experimental CGRs under cyclic and constant load are compared with the existing CGR data for Alloy 600 to determine the relative susceptibility of these alloys to EAC. A detailed characterization of the material microstructure, tensile properties, and fracture morphology is given.

---

**NUREG/CR-4667, Volume 35, has been  
reproduced from the best available copy.**

---

## Foreword

---

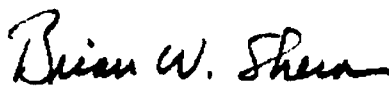
For more than 34 years, Argonne National Laboratory (ANL) has served the U.S. Nuclear Regulatory Commission (NRC), Office of Nuclear Regulatory Research (RES), as a prime contractor for studies of the environmental degradation of structural materials in light-water reactor environments. As Volume 35 in the NUREG/CR-4667 series, this document represents the annual report of ANL program studies for Calendar Year 2004. The program is divided into four tasks:

- Task 1 focuses on the environmental degradation of fatigue life of pressure boundary materials.
- Task 2 addresses irradiation-assisted stress corrosion cracking (IASCC) of stainless steels in boiling-water reactor (BWR) environments, while the parallel program in Task 3 addresses IASCC of stainless steels in pressurized-water reactor (PWR) environments.
- Task 4, the study of crack growth rates in nickel-base alloys typically used in vessel penetrations, is currently focused on testing Alloy 600 and its associated weld metals, Alloys 82 and 182.

Studies of the degradation of fatigue life of pressure boundary materials was concluded this year, with the final emphasis on the evaluation of surface roughness of stainless, carbon, and low-alloy steels on their fatigue life in high-temperature air and simulated reactor coolants. The activity in the future will consist of finalizing the equations describing the proposed design curves, developing appropriate mathematical expressions of the environmental correction factors for each material and environment combination, and presenting these conclusions to the stakeholders. The equations for the design curves are presented and justified in this annual report.

The evaluation of the effects of irradiation on mechanical properties, stress corrosion cracking, and fracture toughness of stainless steels and nickel-base alloys used in reactor core internal structures is an important aspect of the ANL program. Crack growth rate testing of Type 304 and Type 304L stainless steel heat-affected zones continued to establish the threshold for IASCC as functions of materials composition, water chemistry, and irradiation damage. Future stress corrosion cracking tests will be conducted in simulated PWR coolant chemistry on stainless steels with greater irradiation damage, and the IASCC tests will be augmented by microstructural characterization of such materials, to assess the effects of radiation-induced segregation of the alloy constituents.

Evaluation of the stress corrosion crack growth resistance of nickel-base alloys continued during this period, and will continue for the foreseeable future. Emphasis in this area is shifting toward the testing of specimens taken from discarded or replaced reactor components, to assist in root cause analysis, and to assess any effects of aging under normal operating reactor conditions. In future years, the stress corrosion crack studies of nickel-base alloys will begin to focus more on Alloy 690 and its associated weld metal, Alloy 152, including cold-worked and heat-affected zone forms of the wrought material.



---

Brian W. Sheron, Director  
Office of Nuclear Regulatory Research  
U.S. Nuclear Regulatory Commission





## Contents

---

Abstract.....	iii
Foreword .....	v
Executive Summary.....	xvii
Acknowledgments .....	xix
Abbreviations .....	xxi
1 Introduction.....	1
2 Effect of LWR Coolant Environments on Fatigue Crack Initiation in Carbon and Low–Alloy Steels and Austenitic Stainless Steels .....	5
2.1 Introduction.....	5
2.2 Mechanism of Fatigue Crack Initiation.....	6
2.3 Fatigue $\epsilon$ –N Data in LWR Environments .....	7
2.3.1 Carbon and Low–Alloy Steels.....	7
2.3.2 Austenitic Stainless Steels .....	10
2.4 Statistical Model .....	13
2.5 Incorporation of Environmental Effects.....	14
2.5.1 Fatigue Design Curves .....	14
2.5.2 Fatigue Life Correction Factor .....	15
2.6 Margins in ASME Code Fatigue Design Curves.....	15
3 Irradiation–Assisted Stress Corrosion Cracking of Austenitic Stainless Steel in BWRs .....	19
3.1 Irradiation Assisted Stress Corrosion Cracking of Austenitic Stainless Steels from Halden Phase I Irradiations .....	19
3.1.1 Introduction.....	19
3.1.2 Review of SSRT Test Results.....	20
3.1.3 An IASCC Model.....	25
3.1.4 Role of Carbon.....	27
3.2 Crack Growth Rate Test of Austenitic Stainless Steels Irradiated in the Halden Reactor .....	27
3.2.1 Introduction.....	27

3.2.2	Experimental .....	28
3.2.3	Crack Growth Tests on Irradiated Stainless Steels in BWR Environments .....	32
3.2.3.1	Specimen GG5T-A of Type 304L SS HAZ, Test CGRI-15 .....	32
3.2.3.2	Specimen GG5T-B of Type 304L SS HAZ, Test CGRI-16 .....	34
3.2.3.3	Specimen 85-1A-TT of Type 304 SS HAZ, Test CGRI-18 .....	37
3.2.3.4	Specimen 85-7A of Type 304 SS HAZ, Test CGRI-20 .....	44
3.2.4	CGRs of Austenitic SS Weld HAZ under Continuous Cycling .....	46
3.2.6	CGRs of Austenitic SS Weld HAZ under Constant Load or Cycling with Long Hold Periods .....	48
3.2.7	Fracture Toughness of Irradiated Austenitic SS Weld HAZ in High-Purity Water at 288°C .....	49
3.2.8	Metallographic Examination of the Fracture Surface of CGR Test Specimen C3-C .....	50
4	Causes and Mechanisms of Irradiation-Assisted Cracking of Austenitic Stainless Steel in PWRs .....	57
4.1	Introduction .....	57
4.2	Irradiation of Austenitic Stainless Steels in the BOR-60 Reactor .....	57
4.3	Assessment of Void Swelling in Austenitic Stainless Steel Core Internals .....	58
5	Cracking of Nickel Alloys and Welds .....	63
5.1	Introduction .....	63
5.2	Crack Growth Rates of Alloy 600 from the Davis-Besse CRDM Nozzle #3 in PWR Environment .....	65
5.2.1	Experimental .....	65
5.2.1.1	Material and Specimen Geometry .....	65
5.2.1.2	Material Characterization .....	66
5.2.1.3	Crack Growth Test Facility and Procedure .....	67
5.2.2	Results .....	68
5.2.2.1	Tensile Strength in Air .....	68
5.2.2.2	Crack Growth Rates in PWR Environment .....	68

5.2.2.3	Fracture Morphology .....	71
5.2.2.3	Crack Growth Rates under Cyclic Loading.....	73
5.2.2.4	SCC Growth Rates .....	73
5.3	Crack Growth Rates of A182 and A82 Alloys from the Vessel Nozzle-to-Pipe Weld of V.C. Summer Reactor .....	75
5.3.1	Experimental .....	75
5.3.1.1	Material and Specimen Geometry.....	75
5.3.1.2	Crack Growth Test Facility and Procedure .....	77
5.3.2	Results .....	78
5.3.2.1	Crack Growth Rates in PWR Environment.....	78
5.3.2.2	Crack Growth Rates under Cyclic Loading.....	82
5.3.2.3	SCC Growth Rates .....	82
6	Summary .....	87
6.1	Environmental Effects on Fatigue $\epsilon$ -N Behavior.....	87
6.2	Irradiation-Assisted Stress Corrosion Cracking of Austenitic Stainless Steel in BWRs ..	87
6.3	Irradiation-Assisted Cracking of Austenitic Stainless Steel in PWRs.....	89
6.4	Environmentally Assisted Cracking of Alloys 600 and 690 in LWR Water .....	89
	References .....	91



## Figures

---

1.	Schematic illustration of growth of short cracks in smooth specimens as a function of fatigue life fraction and crack velocity as a function of crack length.....	6
2.	Crack growth rates plotted as a function of crack depth for A533-Gr B low alloy steel and Type 304 SS in air and LWR environments. ....	7
3.	Effect of surface roughness on the fatigue life of A106-Gr B carbon steel and A533-Gr B low-alloy steel in air and high-purity water at 289°C.....	9
4.	Effect of water flow rate on fatigue life of A333-Gr 6 carbon steel in high-purity water at 289°C and strain amplitude and strain rates of 0.3% and 0.01%/s and 0.6% and 0.001%/s, respectively. ....	9
5.	Effect of strain rate on the fatigue life of Type 304 and Type 316NG SS in water environments at 288°C.....	11
6.	Effect of material heat treatment on the fatigue life of Type 304 SS in air, BWR, and PWR environments at 289°C.....	11
7.	Micrographs showing sites of crack initiation on fracture surfaces of sensitized Type 304 SS tested in BWR and PWR environments at 289°C. ....	11
8.	Effect of surface roughness on the fatigue life of Type 316NG and Type 304 SS in air and LWR environments at 289°C.....	12
9.	Fatigue data for carbon and low-alloy steel and Type 304 stainless steel components. ....	16
10.	Fracture surface morphology of high-S, low-Mn Type 304 SS Specimen L13-03B produced during bending in 23°C air without previous exposure to water or H charging.....	22
11.	Schematic illustration of proposed IASCC model. ....	26
12.	Configuration of compact-tension specimen for this study. ....	29
13.	Crack-length-vs.-time plots for irradiated H5 weld HAZ Specimen GG5T-A in high-purity water at 289°C during test periods precracking-3, 4-6, and 7-8.....	33
14.	Crack-length-vs.-time plots for irradiated H5 weld HAZ Specimen GG5T-B in high-purity water at 289°C during test periods precracking-3, 4-7, and 8-10.....	35
15.	Change in crack length and ECP of Pt and SS electrodes when the DO level in feedwater was decreased from $\approx 350$ to $< 30$ ppb. ....	36
16.	Photomicrograph of the fracture surface of Specimen GG5T-B. ....	37
17.	Change in crack length and ECP of Pt and SS electrodes when the DO level in feedwater was decreased from $\approx 250$ to $< 30$ ppb. ....	38
18.	Photomicrograph of the fracture surface of Specimen 85-1A-TT.....	38

19.	Micrograph of the fracture surface of Specimen 85-1A-TT tested in BWR environments. ....	39
20.	Crack-length-vs.-time plots for irradiated SMA weld HAZ Specimen 85-1A-TT in high-purity water at 289°C during test periods 1-2, 3-5, and 6-7. ....	39
21.	Micrographs showing the fracture surface of Specimen 85-1A-TT at positions A and B in Fig. 19. ....	41
22.	Micrographs showing the fracture surface of Specimen 85-1A-TT at position C in Fig. 19. ....	41
23.	Micrographs showing the fracture surface of Specimen 85-1A-TT at positions D and E in Fig. 19. ....	42
24.	Photomicrographs showing a slice of the entire length of the fracture surface and high-magnification photomicrographs of the fracture surface at positions A, B, C, and D. ....	43
25.	Load vs. load-line displacement curve for irradiated SMA weld HAZ Specimen 85-1A-TT in high-purity water at 289°C. ....	44
26.	Fracture toughness J-R curve for irradiated SMA weld HAZ Specimen 85-1A-TT in high-purity water at 289°C. ....	44
27.	Crack-length-vs.-time plots for irradiated SMA weld HAZ Specimen 85-7A in high-purity water at 289°C during test periods 1-3, 4-5, and 6-8. ....	45
28.	Photomicrograph of the fracture surface of Specimen 85-7A. ....	46
29.	CGR for irradiated and nonirradiated specimens of laboratory-prepared Type 304 SS SMA weld HAZ and Type 304L SA weld HAZ from the Grand Gulf core shroud under continuous cycling in high-purity water at 289°C. ....	47
30.	CGR under constant load with periodic partial unloads for nonirradiated and irradiated SS weld HAZ specimens in high-purity water at 289°C. ....	49
31.	Fracture toughness $J_{Ic}$ as a function of neutron exposure at 288°C for austenitic SSs in air and SS SMA weld HAZ in high-purity water. ....	50
32.	Crack growth rate under constant load for irradiated austenitic SSs in high-purity water at 289°C. ....	51
33.	Plots of crack length and $K_{max}$ vs. time for Specimen C3-C in high-purity water at 289°C during test periods 6 and 7. ....	51
34.	Side view of the first slice cut from Specimen C3-C. ....	52
35.	A photograph of the entire crack extension for the first slice of Specimen C3-C and high-magnification micrographs of the surface at locations 2 and 1, respectively. ....	53
36.	Photograph of the fracture surface of the second slice of Specimen C3-C and high-magnification micrographs of the surface at locations D, C, B, and A. ....	54
37.	Range of irradiation temperature and dose for which void swelling data have been reported for PWR core internals. ....	59

38.	Void swelling of PWR internals plotted as a function of dose.....	60
39.	Density change in CW Type 316 SS fuel hex can irradiated in reflector region of EBR-II at 376-460°C to 5-80 dpa.....	61
40.	Photograph of the ring from Davis-Besse CRDM Nozzle #3.....	65
41.	Configuration of the cylindrical tensile specimen.....	66
42.	Configuration of the 1/4-T compact tension specimen.....	66
43.	Orientation and location of the test specimens taken from the Davis-Besse CRDM nozzle.....	66
44.	Typical microstructure observed along longitudinal or circumferential planes for Alloy 600 from D-B CRDM nozzle #3.....	67
45.	Engineering stress-vs.-strain curve at 316°C for Alloy 600 from D-B CRDM nozzle #3.....	69
46.	Micrograph of the fracture surface of Specimen N3CL-1.....	70
47.	Micrograph of the fracture surface of Specimen N3CC-2.....	71
48.	Micrograph of the fracture surface of Specimen N3CC-3.....	71
49.	Examples of transition from a transgranular to an intergranular fracture in Specimen N3CL-1.....	72
50.	Fracture surface of Specimen N3CC-2, and high-magnification micrographs at locations A and B.....	72
51.	CGR data for D-B CRDM nozzle Alloy 600 in PWR water at 316°C under cyclic loading.....	73
52.	CGR data for D-B CRDM nozzle Alloy 600 in PWR water at 316°C under constant load.....	74
53.	Log-normal distribution of constant $\alpha$ in Eq. 32 for 26 heats of Alloy 600.....	74
54.	Configuration of the 1/2-T compact tension specimen.....	75
55.	Orientation and location of the test specimens taken from the V.C. Summer piece.....	76
56.	Microstructure of the V.C. Summer Alloy 82 weld and Alloy 182 butter.....	76
57.	Defects found in the V.C. Summer weld and butter alloys: precipitates in the butter, grain boundary sliding at the weld-pipe interface, and cracks in the weld.....	77
58.	Micrograph of the fracture surface of Specimen WCR-01.....	80
59.	Micrographs of a portion of the fracture surface of specimen WCR-01 and higher magnification of position 1 and position 2.....	80
60.	Micrograph of the fracture surface of Specimen BCR-01.....	81
61.	Micrographs of the fracture surface of Specimen BCR-01 at locations 1 and 2 in Fig. 60.....	81
62.	Fatigue CGR data for Ni-alloy welds in PWR environment plotted as a function of the growth rate for Alloy 600 in air under the same loading conditions.....	82

63.	Crack growth data for the V. C. Summer alloys and laboratory-prepared welds in PWR environment at 320°C under constant load as a function of applied $K_{max}$ compared with the proposed disposition curve for Alloy 182.....	83
64.	Crack growth data in PWR environment under constant load for the V. C. Summer weld alloys obtained in the present study and by Jacko et al.....	84



## Tables

---

1.	Factors to be applied to mean $\epsilon$ -N curve.....	17
2.	Composition of Type 304 stainless steels investigated.....	29
3.	Tensile properties of the austenitic stainless steels irradiated in the Halden reactor. ....	30
4.	Crack growth results for Specimen GG5T-A of Type 304L HAZ in high-purity water at 289°C.....	33
5.	Crack growth results for Specimen GG5T-B of Type 304L HAZ in high-purity water at 289°C.....	35
6.	Crack growth results for Specimen 85-1A-TT of Type 304 SS SMA weld HAZ in high-purity water at 289°C.....	37
7.	Crack growth data for Specimen 85-7A of SS SMA weld HAZ in high-purity water at 289°C.....	45
8.	Crack growth results for Specimen C3-C of Type 304 SS in high-purity water at 289°C.....	51
9.	Chemical composition and tensile properties of Alloy 600 from D-B Nozzle #3.....	65
10.	Tensile test results at 316°C for Alloy 600 from D-B CRDM nozzle #3. ....	68
11.	Crack growth results for 1/4-T CT Specimen N3CL-1 of Alloy 600 in PWR water at 316°C..	69
12.	Crack growth data for 1/4-T CT Specimen N3CC-2 of Alloy 600 in PWR water at 316°C.....	70
13.	Crack growth data for 1/2-T CT Specimen N3CC-3 of Alloy 600 in PWR water at 316°C.....	70
14.	Crack growth results for Specimen WCR-01 of Alloy 82 SMA weld in PWR water at 320°C.	78
15.	Crack growth data for Specimen BCR-01 of Alloy 182 SMA weld in PWR water at 320°C....	79



## Executive Summary

---

The fatigue lives of carbon and low-alloy steels and austenitic SSs are decreased in LWR environments; the magnitude of the reduction depends on temperature, strain rate, DO level in water, and, for carbon and low-alloy steels, S content in steel. The threshold values of the critical parameters and the effects of other parameters, e.g., water conductivity, water flow rate, and material heat treatment, on the fatigue life of the steels are summarized. Statistical models are presented for estimating the fatigue life of carbon and low-alloy steels and wrought and cast austenitic SSs as a function of material, loading, and environmental parameters. Two approaches are presented for incorporating the effects of LWR environments into ASME Section III fatigue evaluations.

Data available in the literature have been reviewed to evaluate the conservatism in the existing ASME Code fatigue evaluations. Much of the conservatism in these evaluations arises from current design procedures, e.g., stress analysis rules and cycle counting. However, alternative approaches, such as finite-element analyses, fatigue monitoring, and improved  $K_e$  factors, can significantly decrease the conservatism in the current fatigue evaluation procedures. Another possible source of conservatism is in the set of margins that are used to adjust the mean strain vs. life curves for laboratory test specimens to obtain fatigue design curves for actual components. Data available in the literature have been reviewed to evaluate the margins on cycles and stress that are needed to account for the differences and uncertainties between actual components and laboratory test specimens. The results indicate that the current ASME Code requirements of a factor of 2 on stress and 20 on cycle are quite reasonable, and do not contain excess conservatism that can be assumed to account for the effects of LWR environments.

The susceptibility of austenitic SSs and their welds to IASCC as a function of the fluence level, water chemistry, material chemistry, and fabrication history is being evaluated. Crack growth rate (CGR) tests and slow strain rate tests (SSRTs) have been conducted on various austenitic SSs irradiated at  $\approx 288^\circ\text{C}$  in a helium environment in the Halden boiling heavy water reactor. During the present reporting period, the results obtained in the present study on steels irradiated to  $\approx 0.45$ , 1.35, and 3.0 dpa were compared with data available in the literature. The bulk S content provided the only good correlation with the susceptibility to IGSCC in  $289^\circ\text{C}$  water. Good resistance to IASCC was observed in Type 304 and 316 steels that contain sulfur concentrations of  $\approx 0.002$  wt.% or less. The IASCC susceptibility of Type 304, 304L, 316, and 316L steels that contain  $>0.003$  wt.% S increased drastically. Also, at sufficiently low concentrations of S, a high concentration of C is beneficial. A two-dimensional map was developed in which susceptibility or resistance to IASCC is shown as a function of bulk concentrations of S and C. The map is helpful to predict relative IASCC susceptibility of Types 304 and 316 SS.

Based on the results of this study, an IASCC model has been developed. The model is based on several key steps known or postulated to occur at the grain boundary containing the crack tip, i.e., grain-boundary segregation of Ni and S, preferential oxidation of Cr and Fe atoms over Ni atoms by oxygen that diffuses along the grain boundary, formation of a Cr-Fe spinel oxide ahead of the crack tip, formation of Ni- and S-rich thin films and islands at the metal/spinel boundary, and melting or amorphization of the Ni- and S-rich thin films and islands.

Crack growth rate tests have been conducted in BWR environments on austenitic SS weld HAZ specimens that were irradiated to  $\approx 0.75$  dpa at  $\approx 288^\circ\text{C}$  in a helium environment in the Halden boiling heavy water reactor. The specimens were obtained from Type 304L SS HAZ of the H5 submerged arc (SA) weld of the Grand Gulf (GG) Reactor core shroud and Type 304 SS HAZ of a laboratory-prepared shielded metal arc (SMA) weld. In normal water chemistry (NWC) BWR environment at  $289^\circ\text{C}$ , the

cyclic CGRs of nonirradiated material of either the laboratory-prepared Type 304 or the GG Type 304L weld HAZ in the as-welded or thermally-treated condition are comparable. For both the GG SA weld HAZ and the laboratory-prepared SMA weld HAZ, irradiation to  $\approx 0.75$  dpa increased the CGRs marginally.

The SCC growth rates are somewhat different from the growth rates under fatigue loading. For nonirradiated GG Type 304L weld HAZ, the CGRs of as-welded and as-welded plus thermally-treated material are comparable. For both conditions, the CGRs are a factor of  $\approx 2$  lower than the NUREG-0313 curve for sensitized SSs in water with 8 ppm DO. The SCC growth rates for Type 304 SS SMA weld HAZ were not obtained. Irradiation to  $5.0 \times 10^{20}$  n/cm<sup>2</sup> ( $\approx 0.75$  dpa) increased the growth rates of all SS weld HAZ materials. The CGRs of irradiated HAZ specimens are a factor of 2–5 higher than those predicted by the NUREG-0313 disposition curve for sensitized SSs in high-DO water. Reducing the corrosion potential of the environment on growth rates had a beneficial effect for all materials that were tested in the BWR environment.

A comprehensive irradiation experiment in the BOR-60 Reactor is under way to obtain a large number of tensile and disk specimens irradiated under PWR-like conditions at  $\approx 325^\circ\text{C}$  to 5, 10, 20, and 40 dpa. Irradiation to  $\approx 5$ , 10, and 20 dpa has been completed. A total of 48 tensile-specimens irradiated to  $\approx 5$  and 10 dpa and 166 transmission electron microscopy (TEM) disk specimens irradiated to  $\approx 5$ , 10, and 20 dpa, have been received and are available for testing.

The available data on void swelling and density change of austenitic SSs was critically reviewed. Irradiation conditions, test procedures, and microstructural characteristics were carefully examined, and key factors that are important to determine the relevance of the database to PWR conditions were evaluated. Based on the information, swelling in thin-walled tubes and baffle bolts in a PWR is not considered a concern. Also, it is considered unlikely that void swelling in a reentrant corner will exceed the threshold level of  $\approx 4\%$  beyond which the swelling rate reaches the steady state rate of 1%/dpa.

The resistance of Ni alloys to EAC in simulated LWR environments is being evaluated. During the current reporting period, CGR tests were completed in the PWR environment on Alloy 600 from the Davis-Besse CRDM nozzle #3, and Alloys 82 and 182 from the V. C. Summer nozzle-to-pipe weld. The results are compared with the existing CGR data for Ni-alloys and welds to determine the relative susceptibility of these materials to environmentally enhanced cracking under a variety of loading conditions. The tensile properties, microstructure, and fracture morphology of the nozzle material have also been characterized.

The cyclic CGRs of the Davis Besse CRDM nozzle alloy show significant environmental enhancement of growth rates. The cyclic CGRs in PWR water at  $316^\circ\text{C}$  may be represented by the curve obtained for Alloy 600 in the NWC BWR environment at  $289^\circ\text{C}$ . Under constant load, the CGRs of the nozzle alloy are a factor of 4–8 higher than the median curve for Alloy 600. The growth rates correspond to  $\approx 95$  percentile of the various data sets used in developing the median curve, i.e., the nozzle material exhibits very high susceptibility to SCC.

The fatigue CGRs of both Alloy 82 weld and Alloy 182 butter from the V. C. Summer weld spool piece are significantly lower than those typically observed for these alloys in air. The SCC growth rates of the two alloys are also lower than the proposed CGR curve for nickel-alloy welds. The relative susceptibility of the two alloys, e.g., Alloy 82 weld and Alloy 182 butter, to SCC cannot be determined accurately because they were tested in different orientations.

## **Acknowledgments**

---

The authors thank T. M. Galvin, E. Listwan, L. A. Knoblich, R. W. Clark, and J. Tezak for their contributions to the experimental effort. This work is sponsored by the Office of Nuclear Regulatory Research, U.S. Nuclear Regulatory Commission, under Job Code Y6388; Program Manager: William H. Cullen, Jr.



## Abbreviations

---

ANL	Argonne National Laboratory
ASME	American Society of Mechanical Engineers
ASTM	American Society for Testing and Materials
BWR	Boiling Water Reactor
CGR	Crack Growth Rate
CIR	Cooperative IASCC Research
CLEE	Cyclic Life Environmental Effects
CRDM	Control Rod Drive Mechanism
C	Circumferential
CT	Compact Tension
CUF	Cumulative Usage Factor
CW	Cold Worked
DB	Davis-Besse
DO	Dissolved Oxygen
EAC	Environmentally Assisted Cracking
ECP	Electrochemical Potential
EDM	Electro-discharged Machined
EDS	Energy Dispersive Spectroscopy
EPR	Electrochemical Potentio-dynamic Reactivation
GBE	Grain Boundary Engineered
GB	Grain Boundary
GBC	Grain Boundary Coverage
GBCD	Grain Boundary Character Distribution
GBO	Grain Boundary Optimized
GG	Grand Gulf
HAZ	Heat Affected Zone
HWC	Hydrogen Water Chemistry
IAC	Irradiation Assisted Cracking
IASCC	Irradiation Assisted Stress Corrosion Cracking
IG	Intergranular
IGC	Intergranular Cracking
IML	Irradiated Materials Laboratory
L	Longitudinal
LWR	Light Water Reactor
MSC	Microstructurally Small Crack

NRC	Nuclear Regulatory Commission
NRR	Nuclear Reactor Regulation
NWC	Normal Water Chemistry
PVRC	Pressure Vessel Research Council
PWR	Pressurized Water Reactor
RIAR	Research Institute of Atomic Reactors
SA	Submerged Arc
SEM	Scanning Electron Microscopy
SCC	Stress Corrosion Cracking
SHE	Standard Hydrogen Electrode
SMA	Shielded Metal Arc
SS	Stainless Steel
SSRT	Slow Strain Rate Tensile
TEM	Transmission Electron Microscopy
TG	Transgranular



# 1 Introduction

---

Since 1967, the Nuclear Regulatory Commission (NRC) and its predecessor the Atomic Energy Commission have conducted research programs that address aging of reactor components. The results of this research have been used to evaluate and establish regulatory guidelines to ensure acceptable levels of reliability for light water reactor (LWR) components. The products of this program, i.e., technical reports, methodologies for evaluating licensee submittals, and other inputs to the regulatory process, have led to the resolution of regulatory issues, as well as the development, validation, and improvement of regulations and regulatory guides. The research on the effects of the environment on component cracking was initiated in response to the determination that environmental effects were critical to several important cracking phenomena in LWR components. A major research program at Argonne National Laboratory (ANL) was initiated in 1979 to address pipe-cracking problems in boiling water reactors (BWRs). Since that time, in response to needs for additional research to support the Office of Nuclear Reactor Regulation (NRR) in assessing cracking problems in aging reactors, the focus of the project has shifted to address other problems in environmental cracking of LWR components. In recent years this activity has been supplemented by NRC participation in the Cooperative Irradiation Assisted Stress Corrosion Cracking Research (CIR) Program, a proprietary activity in which groups in several countries contribute money that is used to support research on irradiation-assisted stress corrosion cracking (IASCC) problems of common interest.

This project consists of several tasks with differing objectives, so the objectives are best described on a task-by-task basis:

## Task 1: Environmental Effects on Fatigue Crack Initiation.

The objective of this task is to provide information on the effects of LWR coolant environments on fatigue crack initiation in carbon and low-alloy steels and austenitic stainless steels (SSs) and to develop procedures for incorporating environmental effects into the ASME Code fatigue evaluations. The contractor will review and evaluate issues related to environmental effects on fatigue as required by the NRC, and participate in American Society of Mechanical Engineers (ASME) Code committees to incorporate the effects of LWR environments in fatigue life analyses.

## Task 2: Evaluation of the Causes and Mechanisms of IASCC in BWRs.

The objectives of this task are to (a) investigate the effects of material chemistry and irradiation level on the susceptibility of SSs to IASCC, (b) develop technical information needed to assure that selected inspection intervals are adequate to assure structural integrity, and (c) verify the effectiveness of industry-proposed mitigative measures. This task will evaluate the susceptibility of austenitic SSs and their welds to IASCC as a function of fluence level, water chemistry, material chemistry, welding process, and fabrication history. It will provide data and technical support required for determination of inspection intervals, to help NRC address various issues that arise in license renewal or other licensee submittals. Crack growth rate (CGR) tests and slow strain rate tests (SSRTs) have been completed on model SSs irradiated up to  $2.0 \times 10^{21}$  n/cm<sup>2</sup> ( $E > 1$  MeV) ( $\approx 3.0$  dpa) during Halden Phase-I experiment (carried out under NRC FIN W6610). Crack growth tests are currently being conducted on submerged arc (SA) and shielded metal arc (SMA) welds of Types 304L and 304 SS irradiated up to  $1.2 \times 10^{21}$  n/cm<sup>2</sup> during Halden Phase II experiment. Also, SSRTs tests are being carried out on grain-boundary-optimized (GBO) model

SS alloys to study the effect of grain boundary geometry on IASCC and investigate the prospect of using grain boundary optimization as a mitigative measure. Models and codes developed under CIR and from industry sources will be benchmarked and used in conjunction with this work.

Industry-developed crack growth models will be analyzed and assessed. Also, the effectiveness of mitigative water chemistry measures, e.g., hydrogen water chemistry, will be assessed. Much of this assessment will depend on data provided by industry, data available in the literature, and data developed as part of this task. However, for CGR models for irradiated materials, it is anticipated that relatively few data will be available because of the expense and difficulty of testing.

#### Task 3: Evaluation of Causes and Mechanisms of IASCC of Austenitic SS in PWRs.

The current database and mechanistic understanding of IASCC under the PWR conditions of higher temperature and higher fluence are very limited. This task will evaluate (a) the effects of high fluence characteristic of PWR components near or beyond end-of-life on IASCC, (b) neutron irradiation embrittlement, e.g., loss of fracture toughness, and (c) void swelling behavior in austenitic SSs. Tests will be conducted on materials irradiated in the BOR-60 reactor in Russia. The test matrix includes a total of 80 tensile specimens and 222 TEM disk specimens of, (a) cold-worked and solution-annealed heats of Types 304, 304L, 316, 316 LN, 347 SS, (b) CF-3 and CF-8 cast austenitic SSs, (c) grain-boundary-optimized Types 304 and 316 SS and Alloy 690, and (d) several laboratory and commercial heats of austenitic SSs that contain low or high concentrations of S or O. Irradiation to  $\approx 5$  and 10 dpa for the tensile specimens and  $\approx 5$ , 10, and 20 dpa for the TEM disks has been completed; irradiation to 40 dpa is in progress.

Microstructural studies will be conducted to characterize the void swelling behavior of irradiated disk specimens in terms of chemical composition, heat treatment, and microstructure of the material. Ball punch or disk bend tests will also be conducted on the disk or coupon specimens to obtain mechanical or fracture properties of the material as a function of neutron damage (dpa). Slow-strain-rate-tensile (SSRT) tests will be conducted

#### Task 4: Cracking of Nickel Alloys and Welds.

The objective of this task is to provide the NRC with technical data on the implications of cracks in Ni-alloy components and welds for residual life, inspection, and repair. Many reactor vessel internal components and their attachment welds, vessel penetrations, and piping butt welds are made of alloys, such as Alloy 600, Alloy X750, and Alloy 182, which are susceptible to primary water stress corrosion cracking (PWSCC). The causes and mechanisms of this cracking and the implications of microstructure, microchemistry, and surface finish for component life are also not well understood, and thus lead to greater uncertainty in licensee submissions that address issues such as damage accumulation and inspection intervals. The NRC research program will address these issues and provide data required to support staff assessment of industry CGR models, and potential crack detection and mitigation measures. This task will evaluate (a) the effects of material and environmental parameters on the susceptibility of nickel alloys and their welds to PWSCC and (b) to develop crack growth data on these alloys in PWR environments to assure that selected inspection intervals are adequate to assure structural integrity.

Task 5: Investigation of Other Modes of Degradation in High-Fluence Materials in PWR Environments.

Research at Saclay, France, has shown that gas generation in high fluence materials can produce unexpected changes in material behavior. Because studies on materials at high fluences and at temperatures of interest to LWRs are relatively limited, it is possible that additional degradation phenomena beyond those studied in detail in the other tasks could occur. The work in this task would seek to study, in cooperation with the CIR and other industry groups, the potential for other degradation phenomena. However, this task was not funded and no activity was planned for this task in FY 2004.



## 2 Effect of LWR Coolant Environments on Fatigue Crack Initiation in Carbon and Low-Alloy Steels and Austenitic Stainless Steels (O. K. Chopra and W. J. Shack)

---

### 2.1 Introduction

Cyclic loadings on a structural component occur because of changes in mechanical and thermal loadings as the reactor system goes from one load set (e.g., pressure, temperature, moment, and force loading) to another. For each load set, an individual fatigue usage factor is determined by the ratio of the number of cycles anticipated during the lifetime of the component to the allowable cycles. Figures I-9.1 through I-9.6 of Appendix I to Section III of the ASME Boiler and Pressure Vessel Code specify fatigue design curves that define the allowable number of cycles as a function of applied stress amplitude. The cumulative usage factor (CUF) is the sum of the individual usage factors, and the ASME Code Section III requires that the CUF at each location must not exceed 1.

The ASME Code fatigue design curves, given in Appendix I of Section III, are based on strain-controlled tests of small polished specimens at room temperature in air. The design curves have been developed from the best fit to the experimental fatigue-strain-vs.-life ( $\epsilon$ -N) data, which are expressed in terms of the Langer equation. The Code fatigue design curves are obtained from the best fit of the experimental data by first adjusting for the effects of mean stress on fatigue life and then reducing the fatigue life at each point on the adjusted curve by a factor of 2 on strain (or stress) or 20 on cycles, whichever is more conservative.

The factors of 2 and 20 are not safety margins but adjustment factors that need to be applied to small-specimen data to obtain reasonable estimates of the lives of actual reactor components. The factors were intended to account for data scatter (including material variability) and differences in surface condition and size between the test specimens and actual components. Subsection NB-3121 of Section III of the Code explicitly notes that the data used to develop the fatigue design curves did not include tests in the presence of corrosive environments that might accelerate fatigue failure. Article B-2131 in Appendix B to Section III states that the owner's design specifications should provide information about any reduction to fatigue design curves that is necessitated by environmental conditions. Existing fatigue  $\epsilon$ -N data illustrate potentially significant effects of LWR coolant environments on the fatigue resistance of carbon and low-alloy steels,<sup>1-10</sup> as well as austenitic SSs.<sup>10-18</sup> Under certain environmental and loading conditions, the fatigue lives of carbon and low-alloy steels can be a factor of 70 lower in the coolant environment than in air.<sup>2,8</sup> Therefore, the margins in the ASME Code may not be adequate to account for the effect of LWR coolant environments on the fatigue lives of these steels.

The objective of this task is to review and evaluate issues related to environmental effects on fatigue crack initiation and to develop procedures for incorporating environmental effects into the ASME Code fatigue evaluations. This report reviews the existing fatigue  $\epsilon$ -N data for carbon and low-alloy steels and wrought and cast austenitic stainless steels in LWR environments. These data are used to define the effects of key material, loading, and environmental parameters on the fatigue lives of these steels. Statistical models are presented for estimating fatigue life as a function of material, loading, and environmental parameters. Methods for incorporating environmental effects into ASME Section III fatigue evaluations are described. Also, the conservatism in the existing ASME Code fatigue evaluations is assessed.

## 2.2 Mechanism of Fatigue Crack Initiation

The formation of surface cracks and their growth to an engineering size (3–mm deep) constitute the fatigue life of a material, which is represented by the fatigue  $\epsilon$ - $N$  curves. Fatigue life has conventionally been divided into two stages: initiation, expressed as the number of cycles required to form microcracks on the surface; and propagation, expressed as cycles required to propagate the surface cracks to engineering size. During cyclic loading of smooth test specimens, surface cracks 10  $\mu\text{m}$  or longer form quite early in life (i.e., <10% of life) at surface irregularities either already in existence or produced by slip bands, grain boundaries, second-phase particles, etc.<sup>8,19</sup> Thus, fatigue life may be considered to consist of the propagation of cracks from 10 to 3000  $\mu\text{m}$  long. Fatigue damage in a material is the current size of the fatigue crack, and damage accumulation is the rate of crack growth.<sup>20</sup>

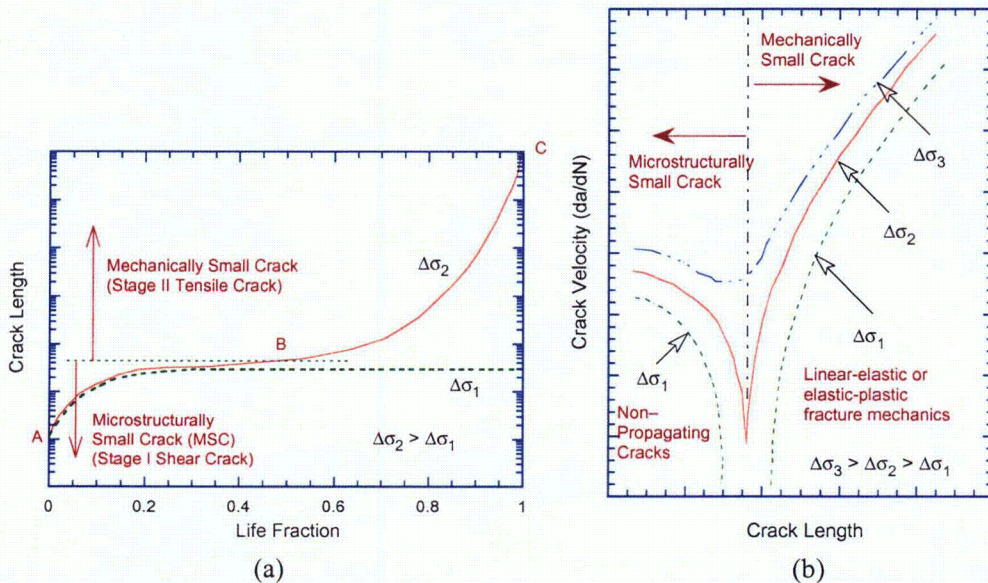


Figure 1. Schematic illustration of (a) growth of short cracks in smooth specimens as a function of fatigue life fraction and (b) crack velocity as a function of crack length.

A schematic illustration of the initiation and propagation stages of fatigue life is shown in Fig. 1. The initiation stage involves growth of “microstructurally small cracks” (MSCs), characterized by decelerating crack growth (AB in Fig. 1a). The propagation stage involves growth of “mechanically small cracks,” characterized by accelerating crack growth (BC in Fig. 1a). The growth of the MSCs is very sensitive to microstructure.<sup>19</sup> Fatigue cracks greater than a critical length show little or no influence of microstructure, and are termed mechanically small cracks. Mechanically small cracks correspond to Stage II (tensile) cracks, which are characterized by striated crack growth, with the fracture surface normal to the maximum principal stress. Various criteria, summarized in Ref. 10, have been used to define the crack length for transition from microstructurally to mechanically small crack. The transition crack length is a function of applied stress ( $\sigma$ ) and microstructure of the material; actual values may range from 150 to 250  $\mu\text{m}$ . At low enough stress levels ( $\Delta\sigma_1$ ), the transition from MSC growth to accelerating crack growth does not occur. This circumstance represents the fatigue limit for the smooth specimen. Although cracks can form below the fatigue limit, they can grow to engineering size only at stresses greater than the fatigue limit. The fatigue limit for a material is applicable only for constant loading conditions. Under variable loading conditions, MSCs can grow at high stresses ( $\Delta\sigma_3$ ) to lengths larger than the transition crack length and then can continue to grow at stress levels below the fatigue limit.

Studies on the formation and growth characteristics of short cracks in smooth fatigue specimens in LWR environments indicate that the decrease in fatigue life in LWR environments is caused primarily by the effects of the environment on the growth of MSCs (i.e., cracks <200  $\mu\text{m}$  deep) and to a lesser extent, on the growth of mechanically small cracks.<sup>8,18</sup> Crack growth rates measured in smooth cylindrical fatigue specimens of A533-Gr B low-alloy steel and austenitic Type 304 SSs in LWR environments and air are shown in Fig. 2. The results indicate that in LWR environments, the period spent in the growth of MSCs (region ABC in Fig. 1a) is decreased. For the A533-Gr B steel, only 30–50 cycles are needed to form a 100- $\mu\text{m}$  crack in high-DO water, whereas  $\approx 450$  cycles are required to form a 100- $\mu\text{m}$  crack in low-DO water and more than 3000 cycles in air. These values correspond to average growth rates of  $\approx 2.5$ , 0.22, and 0.033  $\mu\text{m}/\text{cycle}$ , respectively, in high-DO water, low-DO water, and air. Relative to air, CGRs for A533-Gr B steel in high-DO water are nearly two orders of magnitude higher for crack sizes <100  $\mu\text{m}$ , and one order of magnitude higher for crack sizes >100  $\mu\text{m}$ .

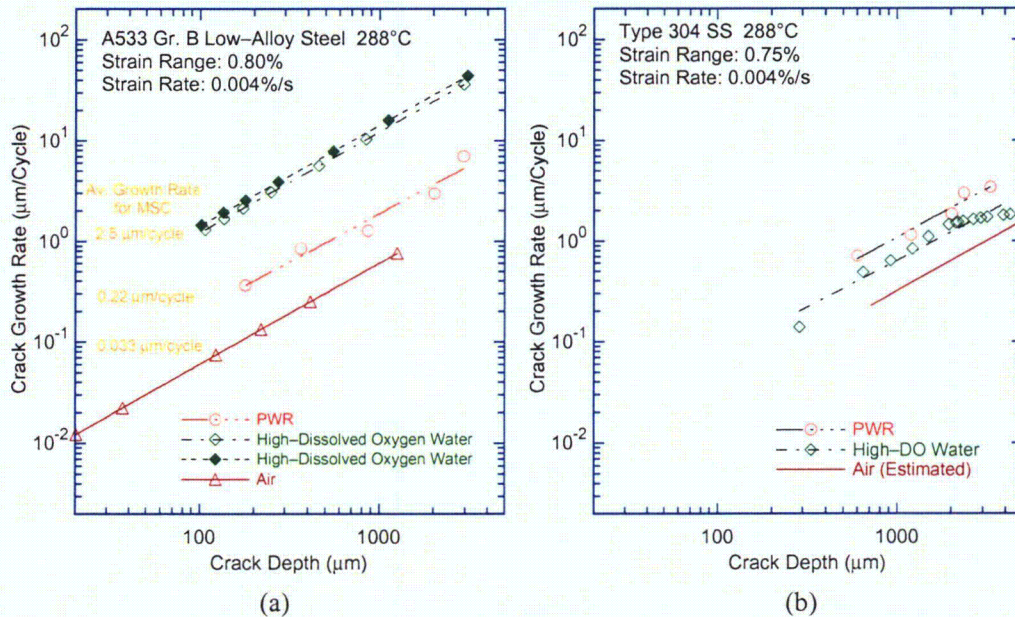


Figure 2. Crack growth rates plotted as a function of crack depth for (a) A533-Gr B low alloy steel and (b) Type 304 SS in air and LWR environments.

## 2.3 Fatigue $\epsilon$ - $N$ Data in LWR Environments

The existing fatigue  $\epsilon$ - $N$  data developed at various establishments and research laboratories worldwide have been compiled and categorized according to different test conditions. The fatigue data were obtained on smooth specimens tested under a fully reversed loading condition, i.e., load ratio  $R = -1$ . Tests on notched specimens or at values of  $R$  other than  $-1$  were excluded. In nearly all tests, fatigue life is defined as the number of cycles,  $N_{25}$ , for tensile stress to drop 25% from its peak or steady-state value.

### 2.3.1 Carbon and Low-Alloy Steels

In air, the fatigue lives of carbon and low-alloy steels depend on steel type, temperature, orientation (rolling or transverse), and strain rate.<sup>8-10</sup> The fatigue life of carbon steels is a factor of  $\approx 1.5$  lower than that of low-alloy steels. For both steels, life is decreased by a factor of  $\approx 1.5$  when temperature is

increased from room temperature to 288°C (550°F). In the temperature range of dynamic strain aging [200–370°C (392–698°F)], these steels show negative sensitivity to strain rate, i.e., cyclic stresses increase with decreasing strain rate. The effect of strain rate on fatigue life is not clear; with decreasing strain rate, for some heats life may be unaffected or decrease, but may increase for other heats. The ASME mean curve for low-alloy steels is in good agreement with the experimental data. The corresponding curve for carbon steels is somewhat conservative, especially at strain amplitudes <0.2%.

The fatigue lives of carbon and low-alloy steels are reduced in LWR environments. Although the microstructures and cyclic-hardening behavior of carbon steels and low-alloy steels are significantly different; the effects of the environment on the fatigue life of these steels are very similar. The magnitude of the reduction depends on temperature, strain rate, DO level in water, S content of the steel, and flow rate. The decrease is significant only when the strain amplitude, temperature, and DO in water are above certain threshold values, and the strain rate is below a threshold value. For both steels, only a moderate decrease in life (by a factor of <2) is observed when any one of the threshold conditions is not satisfied. The S content in the steel is also important. Its effect on life appears to depend on the DO level in water. The threshold values and the effects of the critical parameters on fatigue life are summarized below.

*Strain:* The results indicate that the environmental effect on fatigue life occurs primarily during the tensile-loading cycle. A minimum total applied strain is required above which environmental effects on life are significant.<sup>8–10</sup> Even within a given loading cycle, environmental effects are only significant at strain levels greater than this threshold value. Limited data suggest that the threshold value is ≈20% higher than the fatigue limit for the steel. Also, hold periods during peak tensile or compressive strain have little or no effect on the fatigue life of the steels.<sup>8</sup>

*Strain Rate:* When all other threshold conditions are satisfied, fatigue life decreases logarithmically with decreasing strain rate below 1%/s.<sup>2,3,5</sup> The effect of environment saturates at ≈0.001%/s.<sup>8–10</sup> When any one of the threshold conditions is not satisfied, e.g., DO <0.04 ppm or temperature <150°C (<302°F), the effects of strain rate are consistent with those observed in air.

*Temperature:* Experimental data indicate a threshold temperature of 150°C (302°F), below which environmental effects on life either do not occur or are insignificant. When other threshold conditions are satisfied, fatigue life decreases linearly with temperature above 150°C and up to 320°C (608°F).<sup>2,3,5</sup> For service conditions involving simple, well-defined transients, temperature may be represented by the average of the minimum temperature or 150°C, whichever is higher, and the maximum temperature.<sup>4</sup>

*Dissolved Oxygen in Water:* When the other threshold conditions are satisfied, fatigue life decreases logarithmically with DO above 0.04 ppm; the effect saturates at ≈0.5 ppm DO.<sup>3,5</sup> Only a moderate decrease in life, i.e., a factor of <2, is observed at DO levels below 0.04 ppm.

*Water Conductivity:* The fatigue life of low-alloy steels decreases when the conductivity is increased.<sup>21–23</sup> The fatigue life of WB36 low-alloy steel at 177°C (350°F) in water with ≈8 ppm DO decreased by a factor of ≈6 when the conductivity of water was increased from 0.06 to 0.5 μS/cm.<sup>22</sup>

*Surface Finish:* In air, the fatigue life of rough A106-Gr B specimens is a factor of 3 lower (triangles in Fig. 3a) compared with smooth specimens, and in high-DO water, it is the same.<sup>24</sup> In low-DO water, the fatigue life of the roughened A106-Gr B specimen is slightly lower than that of smooth specimens. The effect of surface roughness on the fatigue life of A533-Gr B steel, Fig. 3b, is similar to that for A106-Gr B steel; in high-DO water, the fatigue lives of both rough and smooth specimens are the same.



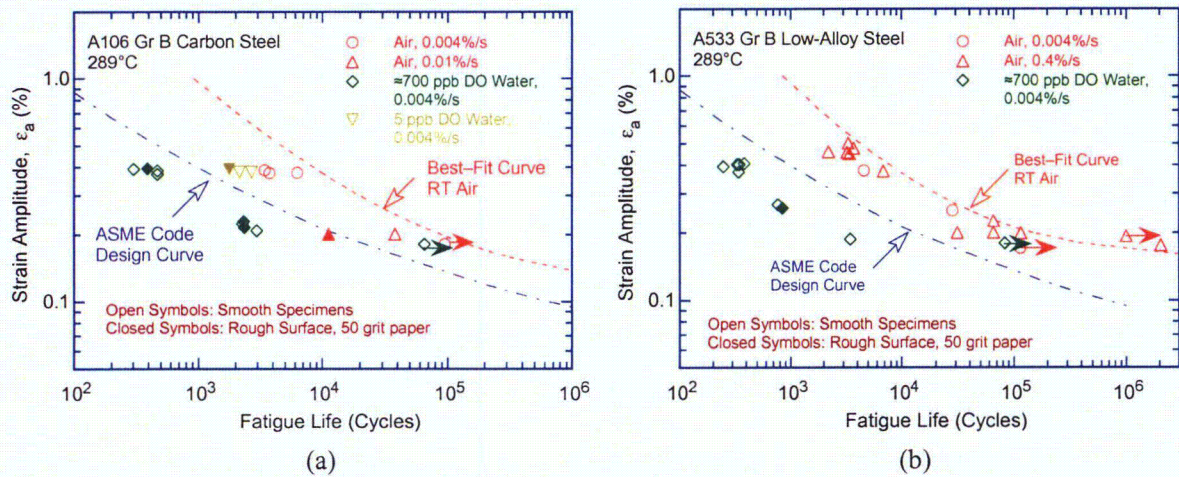


Figure 3. Effect of surface roughness on the fatigue life of (a) A106–Gr B carbon steel and (b) A533–Gr B low-alloy steel in air and high-purity water at 289°C.

*Sulfur Content of Steel:* The effect of S content on fatigue life appears to depend on the DO content of the water. When the threshold conditions are satisfied, the fatigue life decreases with increasing S content for DO levels  $\leq 1.0$  ppm. Limited data suggest that the effects of S on life saturate at an S content of  $\approx 0.015$  wt.%.<sup>8</sup>

*Flow Rate:* Under the environmental conditions typical of operating BWRs, environmental effects on the fatigue life of high-S (0.016 wt.%) carbon steels are a factor of at least 2 lower at high flow rates [7 m/s (23 ft/s)] than at 0.3 m/s (1 ft/s) or lower.<sup>25–28</sup> The beneficial effects of increased flow rate are greater at low strain rates, as shown in Fig. 4, and insignificant for low-S ( $< 0.008$  wt.% S) steel.<sup>25–27</sup> A factor of 2 increase in fatigue life has also been observed in tests on carbon steel tubing (0.025 wt.% S) with internal flow rates of up to 0.6 m/s.<sup>28</sup>

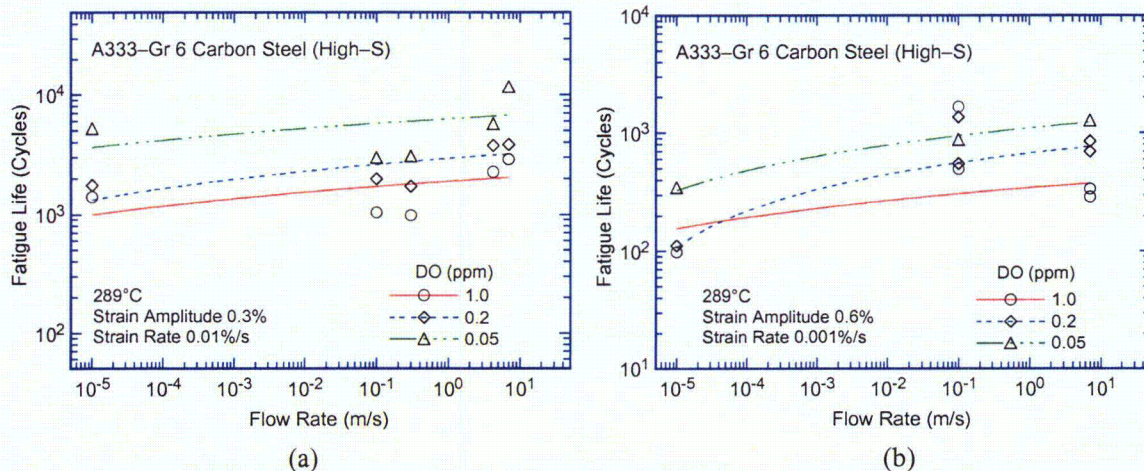


Figure 4. Effect of water flow rate on fatigue life of A333–Gr 6 carbon steel in high-purity water at 289°C and strain amplitude and strain rates of (a) 0.3% and 0.01%/s and (b) 0.6% and 0.001%/s, respectively.

### 2.3.2 Austenitic Stainless Steels

In an air environment, the fatigue lives of Types 304 and 316 SS are comparable. At high strain amplitudes, the life of Type 316NG is slightly higher than that of Types 304 and 316 SS. The results also indicate that the fatigue life of austenitic SSs in air is independent of temperature from room temperature to 427°C (800°F). Although the effect of strain rate on fatigue life is significant at temperatures above 400°C (752°F), variations in strain rate in the range of 0.4–0.008%/s have no effect on the fatigue lives of SSs at temperatures up to 400°C.<sup>29</sup> The fatigue behavior of cast CF–8 and CF–8M SSs is similar to that of wrought austenitic SSs.<sup>17</sup>

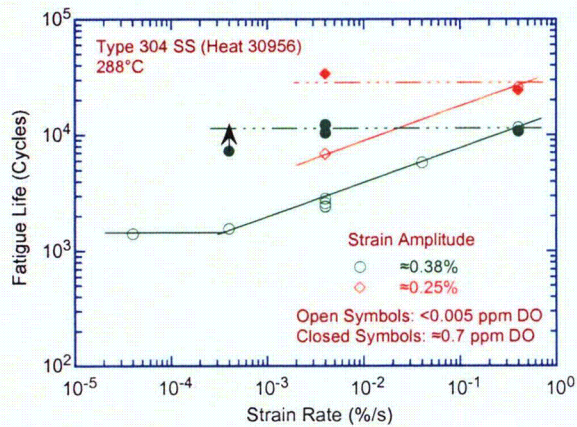
The ASME Code mean curve is not consistent with the existing fatigue  $\epsilon$ – $N$  data for austenitic SSs. At strain amplitudes <0.5%, the mean curve predicts significantly longer fatigue lives than those observed experimentally.<sup>17,30</sup>

The fatigue lives of austenitic SSs are also decreased in LWR environments. The magnitude of the reduction depends on strain amplitude, strain rate, temperature, DO level in the water, and the composition and heat treatment of the steel.<sup>10–18</sup> As in the case of the carbon and low–alloy steels, fatigue life is reduced significantly only when certain critical parameters meet certain threshold values. The critical parameters that influence fatigue life and the threshold values that are required for environmental effects to be significant are summarized below.

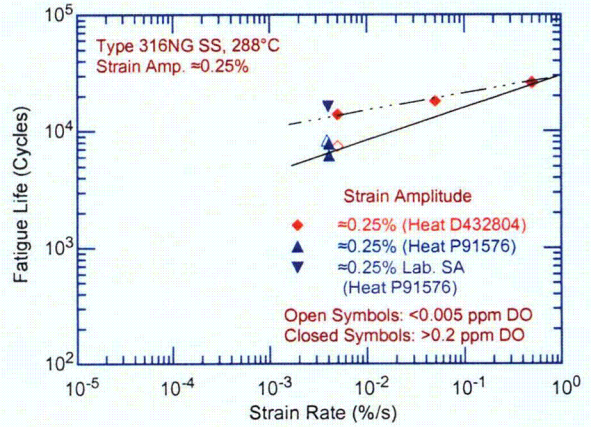
*Strain Amplitude:* As in the case of the carbon and low–alloy steels, the environmental effect occurs primarily during the tensile–loading cycle. Again, a minimum threshold strain is required for the environmentally induced decrease in fatigue lives of SS to occur. The threshold strain appears to be independent of material type (weld or base metal) and temperature in the range of 250–325°C and is related to the elastic strain range of the material.<sup>15</sup> Limited data indicate that hold periods during peak tensile or compressive strain have no effect on the fatigue life of austenitic SSs.<sup>11,31</sup>

*Dissolved Oxygen in Water:* In contrast to the behavior of carbon and low–alloy steels, in low–DO (<0.04 ppm) water, the fatigue lives of all compositions and heat treatment conditions of wrought austenitic SSs are decreased significantly. In high–DO water, the fatigue lives seem to be influenced by the composition and heat treatment of the steel.<sup>32</sup> For a heat of high–C Type 304 SS (Fig. 5a), fatigue life decreased linearly with decreasing strain rate in low–DO water, whereas in high–DO water, strain rate had no effect on fatigue life. For the low–C Type 316NG SS (Fig. 5b), a small effect of strain rate is observed in high–DO water for Heat D432804, and environmental effects are the same for Heat P91576 in low– and high–DO water.

The effect of heat treatment on the fatigue life of Type 304 SS in air, BWR, and PWR environments is shown in Fig. 6. Fatigue life is plotted as a function of the electrochemical potentiodynamic reactivation (EPR) value for various material conditions.<sup>32</sup> Heat treatment has little or no effect on the fatigue life in air and PWR environments. In a BWR environment, fatigue life is lower for the sensitized SSs; the decrease in life increases with increasing degree of sensitization. The fracture mode for the sensitized steel is also different in high–DO water (Fig. 7). In air and PWR environment, irrespective of the degree of sensitization, the fracture mode for crack initiation (i.e., crack lengths up to  $\approx 200 \mu\text{m}$ ) and crack propagation (i.e., crack lengths  $>200 \mu\text{m}$ ) was primarily transgranular (TG); some intergranular (IG) facets were observed in heavily sensitized steel (Fig. 7b). In BWR environment, the initial crack was IG under all heat–treated conditions (Fig. 7a), and changed within  $\approx 200 \mu\text{m}$  to a TG mode with cleavage–like facets and a well–defined river pattern.



(a)



(b)

Figure 5. Effect of strain rate on the fatigue life of (a) Type 304 and (b) Type 316NG SS in water environments at 288°C.

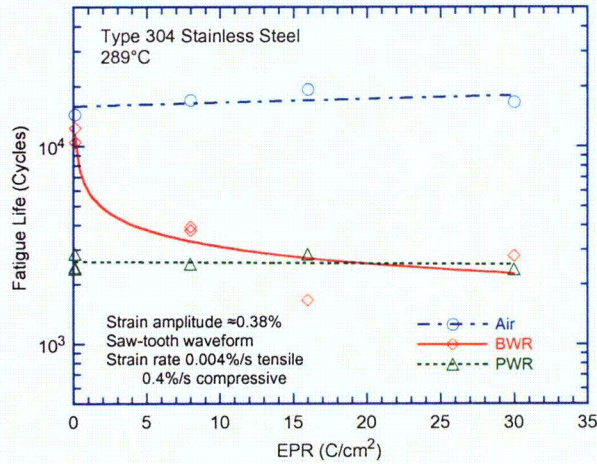
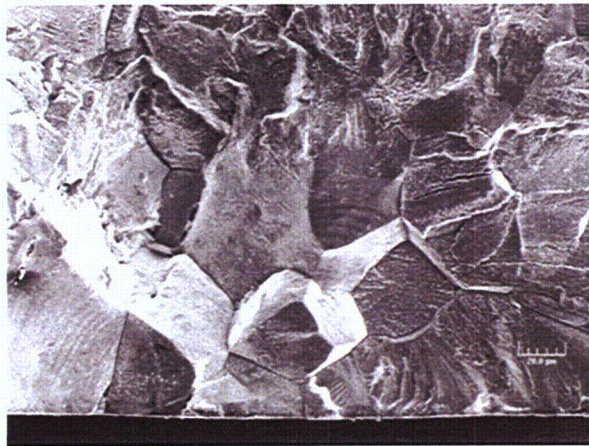
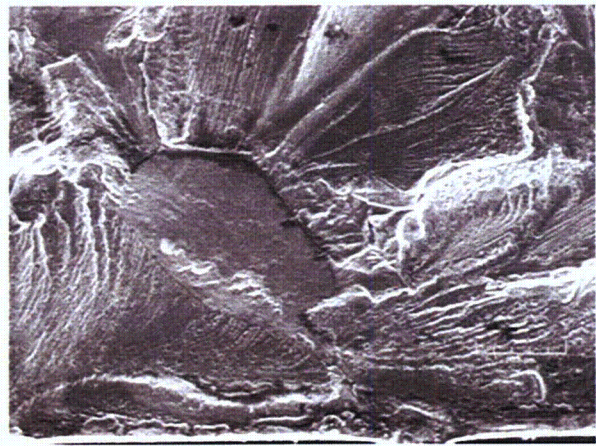


Figure 6. Effect of material heat treatment on the fatigue life of Type 304 SS in air, BWR, and PWR environments at 289°C.



(a)



(b)

Figure 7. Micrographs showing sites of crack initiation on fracture surfaces of sensitized Type 304 SS tested in (a) BWR and (b) PWR environments at 289°C.

In low-DO water, the fatigue lives of cast SSs are comparable to those for wrought SSs.<sup>13-17</sup> Limited data suggest that the fatigue lives of cast SSs in high-DO water are approximately the same as those in low-DO water.<sup>17</sup>

**Strain Rate:** In low-DO environments, fatigue life decreases logarithmically with decreasing strain rate below  $\approx 0.4\%/s$ ; the effect of environment on life saturates at  $\approx 0.0004\%/s$ .<sup>10-18</sup> Only a moderate decrease in life is observed at strain rates  $>0.4\%/s$ . In high-DO water, the effect of strain rate may be less pronounced than in low-DO water.

**Water Conductivity:** Similar to the behavior of carbon and low-alloy steels, the fatigue lives of austenitic SSs are also affected by the conductivity of water. In high-DO water, fatigue life decreases by a factor of  $\approx 2$  when the conductivity of water is increased from  $\approx 0.07$  to  $0.4 \mu S/cm$ .<sup>18</sup>

**Temperature:** The data suggest a lower threshold temperature of  $150^\circ C$  ( $302^\circ F$ ). Above this temperature the environment decreases life in low-DO water if the strain rate is below the threshold of  $0.4\%/s$ .<sup>7,11</sup> In the range of  $150-325^\circ C$  ( $302-617^\circ F$ ), the logarithm of fatigue life decreases linearly with temperature. Only a moderate decrease in life is observed in water at temperatures below the threshold value of  $150^\circ C$ . For variable loading conditions, temperature may be represented by the average of the maximum temperature and the minimum temperature or  $150^\circ C$ , whichever is greater.<sup>12</sup>

**Surface Finish:** For austenitic SSs, the fatigue life of roughened specimens is lower than that of the smooth specimens in air and low-DO water environments (Fig. 8).<sup>24</sup> In high-DO water, the fatigue life is the same for rough and smooth specimens.

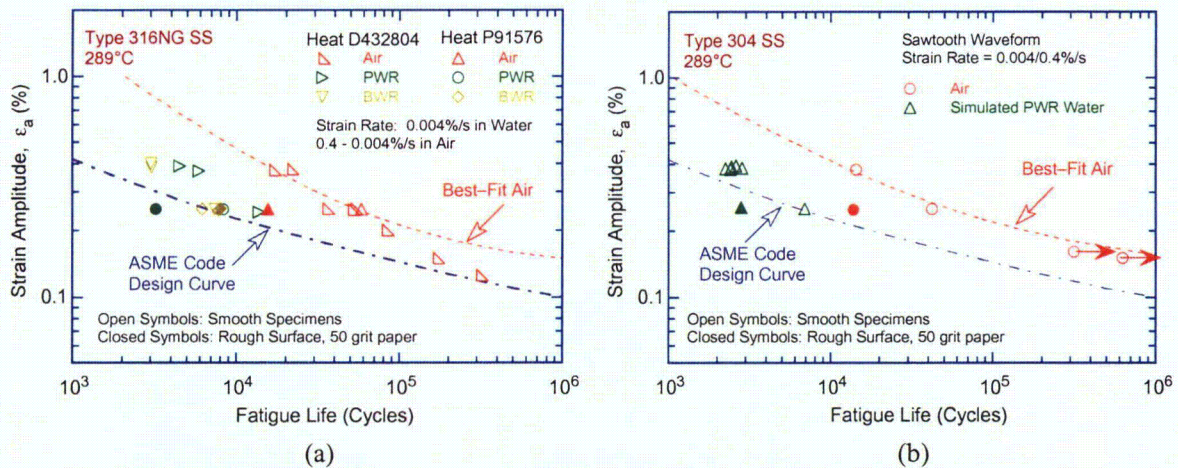


Figure 8. Effect of surface roughness on the fatigue life of (a) Type 316NG and (b) Type 304 SS in air and LWR environments at  $289^\circ C$ .

**Flow Rate:** Limited data indicate that the water flow rate has no effect on the fatigue life of austenitic SSs in high-purity water at  $289^\circ C$ . The fatigue lives of Type 316NG at  $0.6\%$  strain amplitude and  $0.001\%/s$  strain rate, in high-purity water with  $0.2$  or  $0.05$  ppm DO at  $289^\circ C$ , showed little or no change when the flow rate was increased from  $\approx 10^{-5}$  to  $10$  m/s.<sup>26, 27</sup> Fatigue lives of Type 304 SS under a flow rate of  $10$  m/s were, however, shorter than those under semi-stagnant conditions.<sup>27</sup>

## 2.4 Statistical Model

Statistical models based on the existing fatigue  $\epsilon$ - $N$  data have been developed at ANL for estimating the fatigue lives of carbon and low-alloy steels and wrought and cast austenitic SSs in air and LWR environments.<sup>8,10,17</sup> In room-temperature air, the fatigue life  $N$  of carbon steels is represented by

$$\ln(N) = 6.564 - 1.975 \ln(\epsilon_a - 0.113); \quad (1)$$

and that of low-alloy steels, by

$$\ln(N) = 6.627 - 1.808 \ln(\epsilon_a - 0.151), \quad (2)$$

where  $\epsilon_a$  is applied strain amplitude (%). In LWR environments, the fatigue life of carbon steels is represented by

$$\ln(N) = 6.010 - 1.975 \ln(\epsilon_a - 0.113) + 0.101 S^* T^* O^* \dot{\epsilon}^*; \quad (3)$$

and that of low-alloy steels, by

$$\ln(N) = 5.729 - 1.808 \ln(\epsilon_a - 0.151) + 0.101 S^* T^* O^* \dot{\epsilon}^*, \quad (4)$$

where  $S^*$ ,  $T^*$ ,  $O^*$ , and  $\dot{\epsilon}^*$  are transformed S content, temperature, DO level, and strain rate, respectively, defined as:

$$\begin{aligned} S^* &= 0.015 && (\text{DO} > 1.0 \text{ ppm}) \\ S^* &= S && (\text{DO} \leq 1.0 \text{ ppm and } S \leq 0.015 \text{ wt.}\%) \\ S^* &= 0.015 && (\text{DO} \leq 1.0 \text{ ppm and } S > 0.015 \text{ wt.}\%) \end{aligned} \quad (5)$$

$$\begin{aligned} T^* &= 0 && (T < 150^\circ\text{C}) \\ T^* &= T - 150 && (T = 150\text{--}350^\circ\text{C}) \end{aligned} \quad (6)$$

$$\begin{aligned} O^* &= 0 && (\text{DO} \leq 0.04 \text{ ppm}) \\ O^* &= \ln(\text{DO}/0.04) && (0.04 \text{ ppm} < \text{DO} \leq 0.5 \text{ ppm}) \\ O^* &= \ln(12.5) && (\text{DO} > 0.5 \text{ ppm}) \end{aligned} \quad (7)$$

$$\begin{aligned} \dot{\epsilon}^* &= 0 && (\dot{\epsilon} > 1\%/s) \\ \dot{\epsilon}^* &= \ln(\dot{\epsilon}) && (0.001 \leq \dot{\epsilon} \leq 1\%/s) \\ \dot{\epsilon}^* &= \ln(0.001) && (\dot{\epsilon} < 0.001\%/s). \end{aligned} \quad (8)$$

In air at temperatures up to 400°C, the fatigue data for Types 304 and 316 SS are best represented by

$$\ln(N) = 6.703 - 2.030 \ln(\epsilon_a - 0.126); \quad (9)$$

and those for Type 316NG, by

$$\ln(N) = 7.433 - 1.782 \ln(\epsilon_a - 0.126). \quad (10)$$

The results indicate that, in LWR environments, the fatigue data for Types 304 and 316 SS are best represented by

$$\ln(N) = 5.675 - 2.030 \ln(\epsilon_a - 0.126) + T' \dot{\epsilon}' O'; \quad (11)$$

and those of Type 316NG, by

$$\ln(N) = 7.122 - 1.671 \ln(\epsilon_a - 0.126) + T' \dot{\epsilon}' O', \quad (12)$$

where  $T'$ ,  $\dot{\epsilon}'$ , and  $O'$  are transformed temperature, strain rate, and DO level, respectively, defined as:

$$\begin{aligned} T' &= 0 && (T < 150^\circ\text{C}) \\ T' &= (T - 150)/175 && (150 \leq T < 325^\circ\text{C}) \\ T' &= 1 && (T \geq 325^\circ\text{C}) \end{aligned} \quad (13)$$

$$\begin{aligned} \dot{\epsilon}' &= 0 && (\dot{\epsilon} > 0.4\%/s) \\ \dot{\epsilon}' &= \ln(\dot{\epsilon}/0.4) && (0.0004 \leq \dot{\epsilon} \leq 0.4\%/s) \\ \dot{\epsilon}' &= \ln(0.0004/0.4) && (\dot{\epsilon} < 0.0004\%/s) \end{aligned} \quad (14)$$

$$O' = 0.281 \quad (\text{all DO levels}). \quad (15)$$

These models are recommended for predicted fatigue lives  $\leq 10^6$  cycles. Equations 11 and 13–15 should also be used for cast austenitic SSs such as CF-3, CF-8, and CF-8M. Although the statistical models do not include the effects of flow rate on the fatigue life, the limited data available on the effects of flow rate suggest that under the conditions typical of operating BWRs, environmental effects on the fatigue life of carbon and low-alloy steels are a factor of  $\approx 2$  lower at high flow rates (7 m/s) than very low flow rates (0.3 m/s or lower).<sup>25–28</sup> Flow rate appears to have little or no effect on the fatigue life of austenitic SSs.<sup>26,27</sup> Also, as noted earlier, because the influence of DO level on the fatigue life of austenitic SSs is not well understood, these models may be conservative for some SSs in high-DO water.

## 2.5 Incorporation of Environmental Effects

Two methods have been proposed for incorporating the effects of LWR coolant environments into the ASME Section III fatigue evaluations. In one case, new environmentally adjusted fatigue design curves are developed<sup>8–10,17</sup>; in the other, fatigue life correction factors  $F_{en}$  are used to adjust the fatigue usage values for environmental effects.<sup>7,16,33</sup>

### 2.5.1 Fatigue Design Curves

Fatigue design curves have been obtained from the statistical models, represented by Eqs. 1–8 for carbon and low-alloy steels, and by Eqs. 9, 11, 13–15 for austenitic SSs. Although the current Code fatigue design curve for austenitic SSs does not include a mean stress correction, studies by Wire et al.<sup>34</sup> indicate an apparent reduction of up to 26% in strain amplitude in the low- and intermediate-cycle regime (i.e.,  $< 10^6$  cycles) for a mean stress of 138 MPa. To be consistent with the current ASME Code philosophy, the best-fit curves are first adjusted for the effect of mean stress by using a modified Goodman relationship.<sup>32</sup> The adjusted curves are then decreased by a factor of 2 on stress and 20 on cycles to obtain design curves.

Examples of fatigue design curves for carbon steels, low-alloy steels, and austenitic SS in LWR environments have been presented elsewhere.<sup>24</sup> For the environmentally adjusted fatigue design curves, a minimum threshold strain is defined, below which environmental effects are modest. Based on the experimental data, the Pressure Vessel Research Council (PVRC) steering committee for Cyclic Life Environmental Effects (CLEE)<sup>35</sup> has proposed a linear variation for the threshold strain: a lower strain amplitude below which environmental effects are insignificant, a slightly higher strain amplitude above which environmental effects decrease fatigue life, and a linear variation of environmental effects between the two values. The two strain amplitudes are 0.07 and 0.08% for carbon and low-alloy steels, and 0.10 and 0.11% for wrought and cast SS.

### 2.5.2 Fatigue Life Correction Factor

The effects of reactor coolant environments on fatigue life have also been expressed in terms of a fatigue life correction factor  $F_{en}$ , which is defined as the ratio of life in air at room temperature to that in water at the service temperature. Values of  $F_{en}$  can be obtained from the statistical model given in Section 2.4, where

$$\ln(F_{en}) = \ln(N_{RTair}) - \ln(N_{water}). \quad (16)$$

From Eqs. 1–15, the fatigue life correction factor for carbon steels is given by

$$F_{en} = \exp(0.554 - 0.101 S^* T^* O^* \epsilon^*); \quad (17)$$

for low-alloy steels, by

$$F_{en} = \exp(0.898 - 0.101 S^* T^* O^* \epsilon^*); \quad (18)$$

and for austenitic SSs, by

$$F_{en} = \exp(1.028 - T^* \epsilon^* O^*). \quad (19)$$

Also defined is a strain threshold below which environmental effects are modest; the values are the same as those used in developing the fatigue design curves. To incorporate environmental effects into a Section III fatigue evaluation, the fatigue usage for a specific stress cycle based on the current Code fatigue design curve is multiplied by the correction factor.

## 2.6 Margins in ASME Code Fatigue Design Curves

Conservatism in the ASME Code fatigue evaluations may arise from (a) the fatigue evaluation procedures and (b) the fatigue design curves. The overall conservatism in ASME Code fatigue evaluations has been demonstrated in fatigue tests on components.<sup>36,37</sup> However, other studies on piping and components indicate that the Code fatigue design procedures do not always ensure large margins of safety.<sup>38,39</sup> In tests on carbon and low-alloy steels vessels,  $\approx 5$ -mm-deep cracks were initiated slightly above (a factor of  $< 2$ ) the number of cycles predicted by the ASME Code design curve (Fig. 9a). Tests on carbon steel pipe welds and on Type 304 SS pipe removed from the C-Reactor at the Savannah River site<sup>39</sup> showed that the number of cycles to produce a leak was lower, and in some cases significantly lower, than that expected from the ASME Code fatigue design curves (Fig. 9a and b).

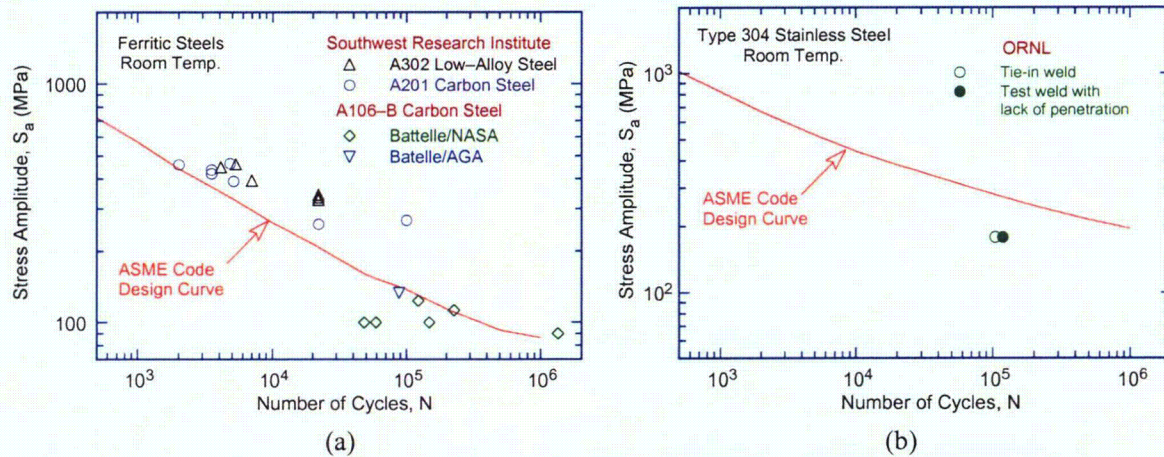


Figure 9. Fatigue data for (a) carbon and low-alloy steel and (b) Type 304 stainless steel components.

Much of the margin in the current evaluations arises from design procedures (e.g., stress analysis rules and cycle counting). However, the ASME Code permits new and improved approaches to fatigue evaluations (e.g., finite-element analyses, fatigue monitoring, and improved  $K_e$  factors) that can significantly decrease the conservatism in the current fatigue evaluation procedures.

The design margins of 2 and 20 on stress and cycles, respectively, were intended to cover the effects of variables that can influence fatigue life but were not investigated in the tests which provided the data for the Code design curves. It is not clear whether the particular values of 2 and 20 include additional conservatism that can account to some degree for environmental effects. The contributions of four groups of variables, namely, material variability and data scatter, size and geometry, surface finish, and loading sequence (Miner's rule), must be considered in developing fatigue design curves that are applicable to components. A study sponsored by the PVRC to assess the margins of 2 and 20 in fatigue design curves concluded that these margins should not be changed.<sup>40</sup> Independent reviews based on data available in the literature are presented in Refs. 10 and 24.

The subfactors that are needed to account for the effects of various material, loading, and environmental variables on fatigue life are summarized in Table 1. These subfactors can be combined to obtain a "total adjustment." The available data indicate that a factor of at least 12.5 on cycles with respect to the mean  $\epsilon$ - $N$  curve for laboratory test specimens in air is needed to account for the effects of data scatter, material variability, component size, surface finish, and loading history. In water, a factor of at least 19 on cycles with respect to the mean  $\epsilon$ - $N$  curve for laboratory test specimens in LWR environments is needed for austenitic SSs, and, because surface effects are insignificant, a factor of at least 10 on cycles is needed for carbon and low-alloy steels.

The factors on strain are needed primarily to account for the variation in the fatigue limit of the material caused by material variability, component size and surface finish, and load history. Because these variables affect life through their influence on the growth of short cracks ( $<100 \mu\text{m}$ ), the adjustment on strain to account for such variations is typically not cumulative, i.e., the portion of the life can only be reduced by a finite amount. Thus, the adjustment is controlled by the variable that has the largest effect on life. In relating the fatigue lives of laboratory test specimens to those of actual reactor components, a factor of  $\approx 1.7$  on strain with respect to the mean  $\epsilon$ - $N$  curve for laboratory test specimens is needed to account for the uncertainties associated with material variability, component size, surface finish, and load history.



These results suggest that the current ASME Code requirements of a factor of 2 on stress and 20 on cycle, to account for differences and uncertainties in fatigue life that are associated with material and loading conditions are quite reasonable, and do not contain excess conservatism that can be assumed to account for the effects of LWR environments. As is done currently for the development of design curves for an air environment, they should be applied to mean data curves for small specimens in LWR environments to obtain design curves.

Table 1. Factors to be applied to mean  $\epsilon$ -N curve.

Parameter	Factor on Life (Air)	Factor on Life (Water)		Factor on Strain or Stress
		Stainless Steels	Carbon/Low-Alloy Steels	
Material variability & experimental scatter	2.0	3.0	3.0	1.2-1.7
Size effect	1.4	1.4	1.4	1.25
Surface finish	3.0	3.0	1.6	1.6
Loading history	1.5-2.5	1.5-2.5	1.5-2.5	1.3-1.6
Total adjustment	12.5-21.0	19.0-31.0	10.0-17.0	1.6-1.7



### **3 Irradiation-Assisted Stress Corrosion Cracking of Austenitic Stainless Steel in BWRs**

---

The objectives of this task are to (a) investigate the effects of material chemistry and irradiation level on the susceptibility of SSs to IASCC, (b) develop technical information needed to assure that selected inspection intervals are adequate to assure structural integrity, and (c) verify the effectiveness of industry-proposed mitigative measures. Tests of CGR and SSRT are being conducted on model SSs, irradiated at  $\approx 288^\circ\text{C}$  in a helium environment in the Halden boiling heavy water reactor, to investigate the effects of material chemistry and irradiation level on the susceptibility of SSs to IASCC. Crack growth tests are currently being conducted on irradiated specimens of SA and SMA welds of Types 304 and 304L SS to establish the effects of fluence level, material chemistry, and welding process on IASCC. Models and codes developed under CIR and from industry sources will be benchmarked and used in conjunction with this work. However, for crack-growth rate models for irradiated materials, it is anticipated that relatively few data will be available because of the expense and difficulty of testing.

#### **3.1 Irradiation Assisted Stress Corrosion Cracking of Austenitic Stainless Steels from Halden Phase I Irradiations (H. M. Chung and W. J. Shack)**

##### **3.1.1 Introduction**

Some BWR and PWR core internal components have failed after accumulation of neutron fluences higher than  $\approx 0.5 \times 10^{21} \text{ n/cm}^2$  ( $E > 1 \text{ MeV}$ ) ( $\approx 0.75 \text{ dpa}$ ) in BWRs and at fluences approximately an order of magnitude higher in PWRs. The general pattern of the observed failures indicates that as nuclear plants age and fluence increases, various nonsensitized austenitic SSs become susceptible to IG failure. Failure of welded components (such as core shrouds fabricated from Type 304 or 304L SS) has also been observed in many BWRs, usually at fluence levels significantly lower than the threshold fluence for the solution-annealed base-metal components.

Although most failed components can be replaced, some safety-significant structural components (e.g., the BWR top guide, core shroud, and core plate) would be very difficult or costly to replace. Therefore, the structural integrity of these components has been a subject of concern, and extensive research has been conducted to provide an understanding of this type of degradation, which is commonly known as IASCC.<sup>41-70</sup>

Irradiation produces profound effects on local coolant water chemistry and component microstructure. Neutron irradiation causes alteration of microchemistry, microstructure, and mechanical properties of the core internal components, which are usually fabricated from American Society for Testing and Materials (ASTM) Types 304, 304L, 316, or 348 SS. It produces defects, defect clusters, and defect-impurity complexes in grain matrices and alters the dislocation and dislocation loop structures, leading to radiation-induced hardening, and in many cases, flow localization via dislocation channeling. It also leads to changes in the stability of second-phase precipitates and the local alloy chemistry near grain boundaries, precipitates, and defect clusters. Grain-boundary microchemistry significantly different from bulk composition can be produced in association with not only radiation-induced segregation, but also thermally driven equilibrium and nonequilibrium segregation of alloying and impurity elements.

Irradiation-induced grain-boundary depletion of Cr has been considered for many years to be the primary metallurgical process that leads to IASCC in BWRs. One of the most important factors that

seems to support the Cr-depletion mechanism is that the IGSCC of nonirradiated thermally sensitized material and the IASCC of BWR-irradiated solution-annealed material depend on water chemistry (i.e., oxidizing potential) in a similar way.<sup>41,44,45</sup> Many investigators have also suggested that radiation-induced segregation of ASTM-specified impurities such as Si and P and other minor impurities not specified in the ASTM specification<sup>48-63</sup> has a role in the IASCC process. However, the exact mechanism of IASCC remains unknown.

In general, IASCC is characterized by strong heat-to-heat variation in susceptibility, even among materials of virtually identical chemical compositions. This suggests that the traditional interpretation based on the role of grain-boundary Cr depletion alone may not completely explain the IASCC mechanism. An irradiation test program is being conducted to investigate systematically the effects of alloying and impurity elements (Cr, Ni, Si, P, S, Mn, C, N, and O) on the susceptibility of austenitic stainless steels to IASCC at several fluence levels.

In previous studies, SSRT tests and fractographic analysis were conducted on model austenitic SS alloys irradiated at 289°C to a “low-fluence” level of  $\approx 0.3 \times 10^{21}$  n/cm<sup>2</sup> ( $E > 1$  MeV)\* ( $\approx 0.43$  dpa), a “medium-fluence” level of  $\approx 0.9 \times 10^{21}$  n/cm<sup>2</sup> ( $\approx 1.3$  dpa),<sup>68,69</sup> and a “high-fluence” level of  $\approx 2.0 \times 10^{21}$  n/cm<sup>2</sup> ( $\approx 3.0$  dpa).<sup>70</sup> Ten of the 11 heats were austenitic SS, and one was austenitic-ferritic SS containing  $\approx 3$  vol.% ferrite of globular shape. The IASCC-resistant or -susceptible behavior of austenitic SSs has been represented in terms of a two-dimensional map of bulk S and C contents of the steels. This report presents an IASCC model for irradiated austenitic SSs.

### 3.1.2 Review of SSRT Test Results

The results of this investigation show that, as neutron fluence increases to a high level (e.g.,  $2.0 \times 10^{21}$  n/cm<sup>2</sup> or 3 dpa), the deleterious effect of S on IASCC susceptibility is dominant over the effects of other elements. The IG fracture surface morphology observed in commercial heats in this study was similar to that of field-cracked BWR core internals. This study also shows that a sufficiently low concentration of S (<0.002 wt.%) is the primary material factor necessary to ensure good resistance to IASCC. Even at slightly higher S concentrations of >0.003 wt.%, Types 304, 304L, 316, and 316L SSs were susceptible to IASCC at 3 dpa. This strong dependence on S concentration suggests that some kind of threshold phenomenon related to S is involved in IASCC.

Note that, for 304- and 316-type steels that contain a low concentration of C of <0.03 wt.% (e.g., Types 304L, 316L, and their high-purity counterparts), an S concentration of <0.002 wt.% is not a sufficient material condition to ensure good resistance to IASCC. This behavior is in distinct contrast to that of 304- and 316-type steels that contain high C concentrations of >0.03 wt.% and S concentration of <0.002 wt.%. The latter class of steels exhibited good resistance to IASCC. This contrasting behavior indicates that, for S concentration <0.002 wt.%, a high concentration of C plays a beneficial role. However, when S concentration is high, i.e., >0.002 wt.%, the deleterious effect of S is so pronounced that the effect of a high concentration of C is largely obscured.

At lower damage levels (i.e., <1 dpa), a high concentration of Si (i.e., 0.8-1.5 wt.%) has a beneficial effect. At higher damage levels, however, this effect appears to be obscured by the deleterious effect of S. Therefore, from the standpoint of BWR IASCC, which usually occurs at damage levels >2.5 dpa, we believe that the typical variation in Si concentration in Types 304 and 316 SS (i.e., 0.4 to 1.0 wt.%) is not

1. \_\_\_\_\_

\* All references to fluence levels are calculated for  $E \geq 1$  MeV.

an important factor. It is not clear if, in addition to a sufficiently low concentration of S (i.e., <0.002 wt.%) and a sufficiently high concentration of C (i.e., >0.03 wt.%), an unusually high concentration of Si (e.g., >1.5 wt.%) provides an extra benefit when fluence is high (e.g., >2.5 dpa). The two heats that belong in this category, i.e., 304 SS Heat L14 (S  $\approx$ 0.002 wt.%, C 0.107 wt.%, and Si 0.96 wt.%) and 316 SS heat L27 (S  $\approx$ 0.002 wt.%, C 0.057 wt.%, and Si 1.82 wt.%) exhibited good resistance at 3 dpa. On the other hand, 304 SS Heat C19, which contains a slightly higher S concentration (i.e., 0.003 wt.%) and a relatively low concentration of Si (i.e., 0.45 wt.%), exhibited a significant susceptibility at 3 dpa despite a high concentration of C (i.e., 0.06 wt.%). Also, 304 SS Heat L6, which contains 0.005 wt.% S and 0.096 wt.% C, exhibited a significant susceptibility at 3 dpa despite a high concentration of Si (i.e., 1.90 wt.%).

Most field-cracked LWR core internals and steels used in SSRT tests or evaluation of crack-growth behavior in the IASCC community contain S concentrations >0.002 wt.%. Therefore, it is not surprising to see that most of them were susceptible to IASCC in one way or another. For S concentrations >0.002 wt.%, the degree of IASCC susceptibility in this study varied significantly from heat to heat, and it was difficult to predict the degree quantitatively. This behavior, consistent with literature data, is not unexpected when one considers that, for a given fluence level, several factors can influence the degree of S segregation to grain boundaries, e.g., annealing and cooling history during fabrication, Mn content, precipitation of sulfides such as MnS and CuS, and solubility of the sulfides in BWR-like water.

The observation that steels that contain a very low or negligible amount of S are resistant to IASCC provides an important clue to the mechanism of IASCC. To understand the mechanism, we believe it is important to consider the following:

1. The strong dependence of IASCC susceptibility on fluence
2. The strong dependence of IASCC susceptibility on S concentration, and an indication of some kind of critical phenomenon involving S
3. Suppression of IASCC susceptibility at high concentration of C (>0.03 wt.%) and sufficiently low S concentrations (<0.002 wt.%), but not at S concentrations >0.003 wt.%
4. Very low solubility of S in austenitic SS at  $\approx$ 300°C
5. Segregation of S to grain boundary
6. Parallel grain-boundary Cr depletion and Ni segregation
7. Strong influence of water chemistry on BWR IASCC
8. Strong effect of strain rate on percent IGSCC from SSRT tests

Considering that the S effect is dominant at high fluence and the grain-boundary Cr depletion is in some respect a mirror image of grain-boundary Ni segregation, we believe it is important to understand the peculiar properties of Ni-S thin film reported by Heuer et al., who investigated the effect of ion-implanted S on disorder-induced amorphization of Ni.<sup>71</sup> Those authors also investigated the effect of thermal segregation of S on grain boundaries on the mechanical properties of nonirradiated binary Ni-S. In the latter investigation, they found that, as the grain boundary concentration of S exceeds  $\approx$ 10 at.%,

( $\approx 5.6$  wt.%), the mechanical properties of S-segregated Ni start to degrade drastically in 23°C air, i.e., there is a precipitous decrease in total elongation, tensile strength, modulus of toughness, reduction in area, and a sharp increase in percent intergranular cracking (IGC). This means that, at a sufficiently high level of S segregation, a grain boundary in the Ni-S system loses metallic strength and behaves more like clay. Okamoto and his coworkers also showed that the volume fraction of amorphization of S-ion-implanted specimens starts to increase drastically when the bulk S concentration exceeds  $\approx 5.6$  wt.%.<sup>71,72</sup> Based on these observations, they concluded that S-induced intergranular fracture in binary Ni-S is explained well by disorder-induced melting of a Ni-S-rich thin film that formed on grain boundaries. They proposed that this process is strongly influenced by S and H concentrations, stress, temperature, and irradiation damage. We believe that the results of Okamoto and his coworkers constitute a very useful framework that can shed light on the mechanistic understanding of IASCC.

Similar to the observation of Heuer et al.,<sup>71</sup> predominantly IG fracture was observed in one of our high-strain-rate bending tests in 23°C air, specifically, a Type 304 SS Heat L13 which contained an unusually high concentration of S (0.022 wt.%) and an unusually low concentration of Mn (0.36 wt.%). The specimen was neither exposed to water nor charged with hydrogen before the bending test. Therefore, the intergranular fracture in the specimen cannot be explained on the basis of H-induced embrittlement of grain boundaries. The high-magnification intergranular fractograph of the specimen, shown in Fig. 10, is characterized by a smooth grain boundary separation, a virtual absence of deformation steps, and an indication of significant grain encirclement. These features are similar to those of IASCC failures produced in 289°C water. Because the specimen was irradiated in high-purity helium, it is also difficult to explain the intergranular fracture by grain boundary oxidation or O segregation. The fracture behavior seems to differ from the limited amount of near-surface intergranular separation reported by Onchi and his coworker<sup>73,74</sup> for thermally sensitized and irradiated 304 SSs that were tested in inert gas at  $\approx 290^\circ\text{C}$ . Nevertheless, the experiment of Fig. 10 shows that purely mechanical intergranular failure similar to that reported in the nonirradiated Ni-S system can occur in a highly irradiated austenitic SS that contains an unusually high concentration of S.

Considering the observations discussed above, we believe that it is important to better understand the structure and properties of Ni- and S-rich thin films and islands that have been reported by Thomas

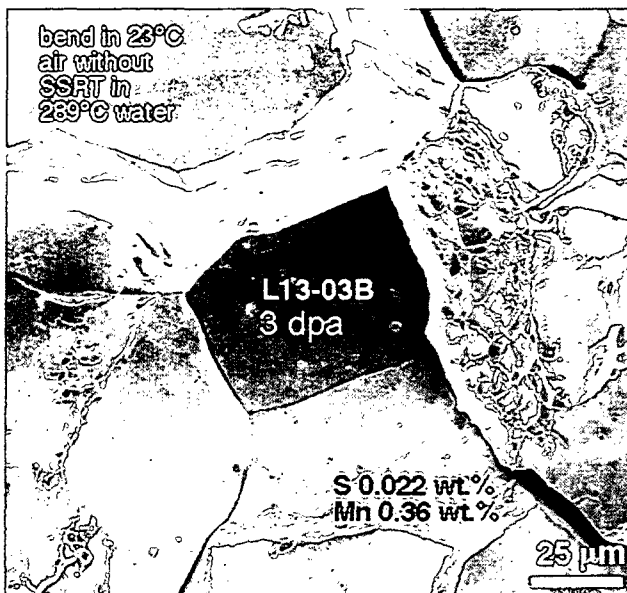


Figure 10. Fracture surface morphology of high-S, low-Mn Type 304 SS Specimen L13-03B (S, 0.022 wt.%; Mn, 0.36 wt.%;  $\approx 3$  dpa in helium at 289°C) produced during bending in 23°C air without previous exposure to water or H charging.

and Bruemmer<sup>75-77</sup> and Dumbill.<sup>78</sup> The former investigators conducted extensive studies on crack-tip microstructure and microchemistry of field-cracked BWR and PWR core internal components.<sup>76,77</sup> Similar studies were also performed by Dumbill<sup>78</sup> and Bruemmer and Thomas<sup>77</sup> on nonirradiated, thermally sensitized 304<sup>78</sup> and 316<sup>77</sup> SSs that were tested in sulfated<sup>78</sup> or deoxygenated<sup>77</sup> BWR-like water at 289°C.

In Ref. 76, Thomas and Bruemmer report extensively on the crack-tip grain boundary microstructural characteristics of a PWR baffle bolt and a BWR top guide, both of which cracked during service. A layer of Cr-Fe-type spinel oxide sandwiched between the two adjacent grain matrices was always observed ahead of an open crack tip. Such an oxide was fine-grained and contained tiny pores (diameter 2-10 nm). In the case of the BWR top guide, numerous irregularly shaped microcavities, as large as ≈100 nm in length and ≈50 nm in width, were observed, usually at the metal/oxide boundary and near the tip of the spinel oxide.

Direct evidence of Ni<sub>x</sub>S<sub>y</sub>-type thin films produced between such a spinel oxide and the metal matrix is observed in several photomicrographs, e.g., Figs. 3-10 and 3-13 in Ref. 76 for the PWR baffle bolt. Small islands of Ni or Ni<sub>x</sub>S<sub>y</sub>-type phase are also observed. The width of such Ni<sub>x</sub>S<sub>y</sub>-type thin film is extremely small, i.e., <7 nm, based on data from energy-dispersive spectroscopy (EDS), and <3 nm based on bright-field image. In the case of the BWR top guide, a similar type of thin film (thickness ≈3 nm), which exhibits the same imaging contrast, is observed at the boundary between the metal matrix and the spinel oxide, e.g., Figs. 4-11, 4-12, 4-14, 4-17, and 4-20 of Ref. 76.

Results of EDS analysis on the top guide indicate that such film contains a high concentration of Ni. However, data for S distribution near the film were not reported. The distance between EDS spots in the analysis was 5-25 nm, significantly larger than the width of such a thin film. Under such conditions, one can easily miss probing a spot correctly placed in the middle of a thin film that is only <3 nm wide. Therefore, it is not easy to measure the distribution of S near such a film. However, microstructural features such as spinel oxide, voids, cavities, the position and shape of an open crack, and Ni<sub>x</sub>S<sub>y</sub>-type thin film can be detected readily through bright-field imaging and tilting. A dark-field image of a <3-nm-wide Ni<sub>x</sub>S<sub>y</sub>-type thin film, which is a more valuable piece of information, would be very difficult to obtain in an irradiated core internal. Dumbill reported results of X-ray mapping that show a matching distribution of Ni and S for a crack tip in his nonirradiated sensitized 304 SS specimen.<sup>78</sup> The Ni- and S-rich thin film in his specimen was relatively thicker (i.e., width ≈100 nm), and a continuous EDS line scan and matching elemental mapping clearly showed the nature of such film.

Thomas and Bruemmer provided a comprehensive interpretation of the crack-tip microstructures observed in their studies.<sup>76,77</sup> They suggested that Cr- and Fe-rich spinel oxide, observed ahead of an open crack tip, was produced as a corrosion byproduct that filled the crack opening after the crack had advanced along the grain boundary. Thus, the spinel oxide tip was interpreted to be the same as the crack tip. Formation of Ni-rich thin films and islands were attributed to a mechanism of selective dissolution in which Cr and Fe atoms are dissolved preferentially over Ni atoms in the crack-tip water.

Nevertheless, photomicrographs and EDS data given in the reports of Thomas and Bruemmer<sup>75-77</sup> or Dumbill<sup>78</sup> shed light on several new clues that are helpful to the understanding of the metallurgical processes that occur near a crack tip. Thus, we thought that a more detailed, integrated evaluation is timely. Several important observations in the following discussion suggest a mechanism in which spinel oxide and Ni and Ni<sub>x</sub>S<sub>y</sub> thin films and islands visible near the crack tip were produced, not after the crack advanced to the position of the spinel oxide tip, but instead, before the crack advanced in association with internal grain-boundary oxidation, which occurred ahead of the crack tip.

The first observation is that a crack tip is often visible adjacent to a grain boundary rather than in line with the grain boundary. The offset distance between the line of crack advance and the grain boundary (imaged edge on) was  $\approx 20$  nm in the field-cracked BWR top guide; see Figs. 4-19 and 4-21 in Ref. 76. In the case of nonirradiated, thermally sensitized 304 and 316 SSs tested in deoxygenated BWR-like water, the offset distance was  $\approx 90$  nm and  $\approx 15$  nm, respectively.<sup>75</sup> This observation is difficult to explain on the basis of preferential dissolution of the grain-boundary metal; it is equally difficult to explain on the basis of the premise that the grain boundary itself shifts continuously ahead of an advancing crack tip. The offset distance is the same as the distance between the grain boundary and the metal/spinel boundary, in which a  $\text{Ni}_x\text{S}_y$ -type thin film and islands are present, often accompanied by high-density voids and cavities. More voids and cavities tend to appear in regions where thin films or islands of  $\text{Ni}_x\text{S}_y$ -type or Ni-rich phases occur. This observation suggests that the voids and cavities were products of localized melting of Ni- and S-rich films or islands. This view is essentially consistent with the results of experiments and the theory advanced by Okamoto and his coworkers on the behavior of S-rich thin film in the Ni-S binary system.<sup>71,72</sup>

The second observation is dark-field morphology of spinel oxide present ahead of an open crack tip. Such a dark-field image was reported in Ref. 75 for a crack tip in a nonirradiated, thermally sensitized 316 SS. In the image, extremely small particles of spinel oxide (diameter  $\approx 5$  nm) are observed decorating the grain boundary  $\approx 290$  to  $\approx 450$  nm ahead of the open crack tip, with twin boundaries  $\approx 350$  nm ahead of the crack tip. This observation provides direct evidence of internal oxidation on grain boundaries and twin boundaries in a BWR-like environment, and it is reasonable to expect a similar phenomenon in a BWR core internal. For ordinary grain boundaries (i.e., grain boundaries that are not involved in crack-tip advancement), evidence of grain-boundary internal oxidation has been reported only for the HAZ in BWR core shroud welds that were prepared by SMA or SA procedure.<sup>79,80</sup> Oxygen contamination in such a HAZ is pronounced, and because O solubility in the grain matrices is extremely low near room temperature, O atoms segregate to grain boundaries during cooling of the HAZ. Internal oxide particles produced by this process have been characterized by Auger electron spectroscopy in Refs. 79 and 80, and by transmission electron microscopy in Ref. 79.

The third observation is pores and voids that decorate previous twin boundaries located within a spinel oxide ahead of an open crack tip. Such a feature, visible in a top guide crack tip in Figs. 4-9 and 4-10 of Ref. 76, cannot be explained on the basis of the premise that the spinel oxide filled the crack opening up to the tip of the spinel oxide. Such a feature is, however, explained well by the premise that a grain boundary region that contains a twin was oxidized internally before the crack advanced to that particular location.

The fourth observation notes the tendency that more cavities are observed near the tip of the spinel oxide layer than near the metal/spinel boundary, e.g., the top guide crack-tip structure shown in Figs. 4-20 to 4-25 of Ref. 76. Also, more Ni and Ni-sulfide islands tend to be present near the tip of a spinel oxide, e.g., Figs. 3-14 (baffle bolt) and 4-18 (top guide) in Ref. 76. This behavior is not explained well by the premise that the spinel oxide filled the crack opening but is explained well by the premise that the spinel oxide extended its length via internal oxidation of the grain boundary. In the latter process, Cr and Fe atoms are expected to be selectively oxidized by the oxygen atoms that diffuse down the grain boundary, thereby gradually enriching the metal near the tip of the oxide with Ni. At the same time, S atoms are predicted to remain in the metal ahead of the spinel tip rather than to be incorporated in the spinel oxide in which their solubility is lower than in the metal.

The above observations lend strong support to a mechanism in which a spinel oxide layer and Ni- and S-rich thin films and islands are produced ahead of an advancing crack tip, and localized melting of



the Ni- and S-rich films and islands plays a primary role in crack propagation. The result of such melting is the production of voids and cavities at the metal/spinel boundary and near the tip of the spinel layer.

### 3.1.3 An IASCC Model

On the basis of several key observations in this study and elsewhere, and on the basis of the discussions above, we propose a new IASCC mechanism for irradiated austenitic SS. The model, initially reported in Ref. 81 and schematically illustrated in Fig. 11, is based on the following steps, some postulated and some supported by observations in this study or other investigations:

1. Many incipient cracks are nucleated in the brittle surface oxide layer that is in contact with water.
2. When one such incipient crack encounters a grain boundary, the metal in front of the crack tip is oxidized preferentially along the grain boundary, because stress and defects (crystallographic and irradiation-induced defects) are higher at the grain boundary. A grain boundary is a preferential path for faster diffusion of O from the water, especially in a highly irradiated steel.
3. The rate of O transport from water to grain-boundary metal is strongly influenced by the thickness and morphology of the Cr oxide layer that covers the crack-tip grain boundary. When grain boundary Cr depletion is significant, the Cr oxide layer is thinner and less protective, which allows a faster permeation and transport of O. If the Cr oxide layer that covers the crack-tip grain boundary is ruptured by twinning or dislocation channeling, O transport to the grain-boundary metal is facilitated.
4. The metal at the crack-tip grain boundary is gradually converted to Cr-Fe-type spinel oxide, because Cr and Fe atoms are preferentially (or selectively) oxidized over Ni atoms by the O atoms that diffused down the grain boundary. Nickel atoms are significantly more difficult to oxidize than Fe and Cr. The free energies of oxidation at  $\approx 300^\circ\text{C}$  of Ni, Fe, and Cr are, respectively,  $-92$ ,  $-111$ , and  $-155$  kcal/mole of  $\text{O}_2$ . Thus, most Ni atoms remain unoxidized in the metal matrix. The result is that Ni atoms, excluded from the growing Cr-Fe spinel oxide layer on the grain boundary, accumulate near the metal/spinel boundary and at the tip of the spinel oxide.
5. At the same time, S atoms segregated on the grain boundary are also pushed out of the spinel oxide, because the solubility of S is lower in the oxide than in the metal.
6. Eventually, Ni- and S-rich thin films or islands form at the metal/spinel boundary and at the tip of the growing spinel oxide layer. The Ni- and S-rich region can be in the shape of a continuous or discontinuous film or a small isolated island. Nickel and S atoms accumulate more at the tip of the long spinel oxide layer than at the metal/spinel boundary, because less oxidation occurs in the latter direction.
7. Some S ions accumulate in the crack tip water because of dissolution of soluble sulfides.<sup>82</sup> Some S atoms are released into the metal due to irradiation-induced instability of  $\text{MnS}$ <sup>83</sup> and subsequently diffuse to the thin region of metal that is in contact with the Ni- and S-rich film under the influence of high tensile stress.

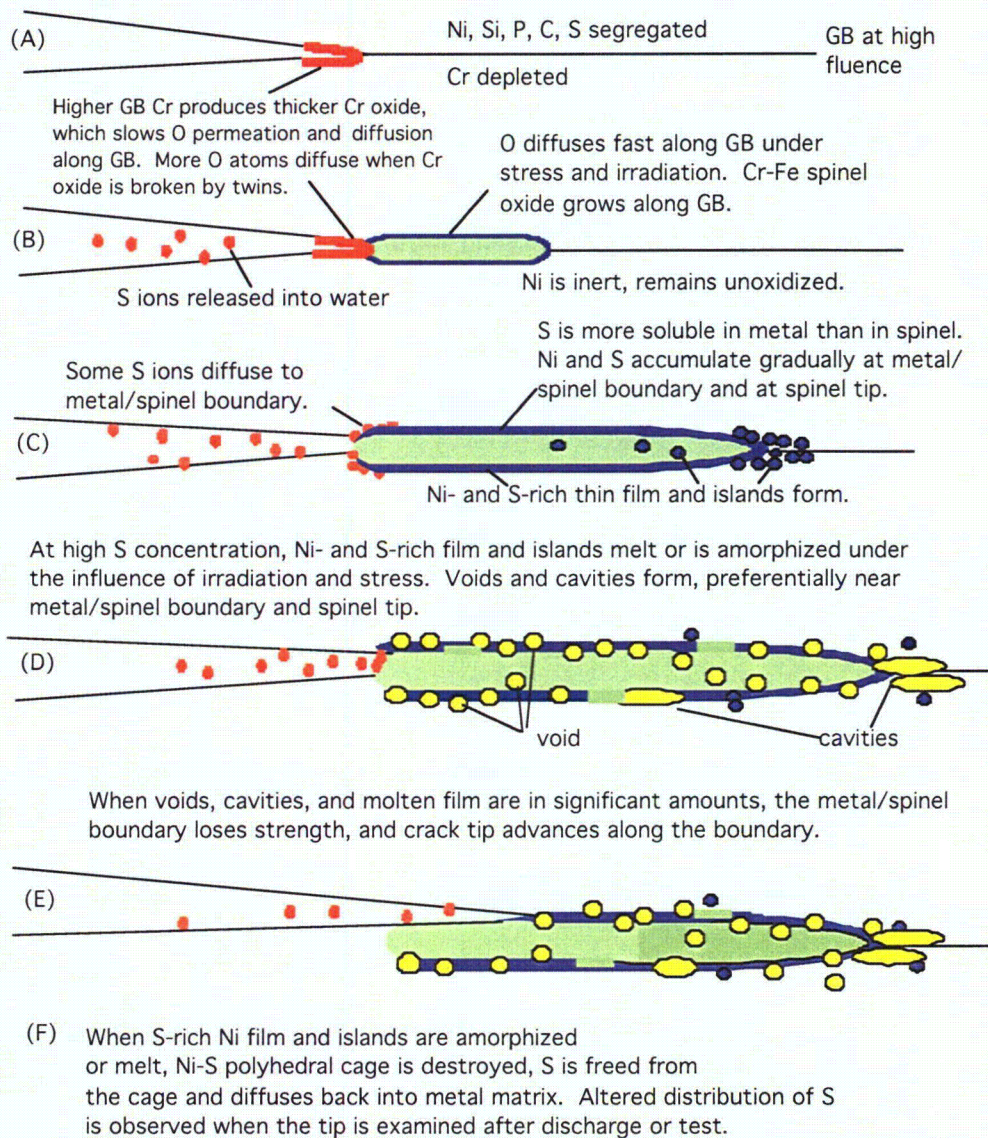


Figure 11. Schematic illustration of proposed IASCC model. (GB = grain boundary)

8. When the concentration of S in the Ni- and S-rich thin film or island exceeds a threshold level, the film or island melts or is amorphized, thereby losing its metallic strength. When the thin film or island melts, voids and cavities are formed near the metal/spinel boundary and at the tip of the spinel layer.
9. The crack tip then advances along the weakened metal/oxide boundary, i.e., along the thin region in which the Ni- and S-rich thin film and islands melt or are amorphized, thereby producing voids and cavities.
10. Voids and cavities tend to be produced more ahead of the spinel tip than at the metal/spinel boundary because of the factor described in Step 6. When a large cavity(ies) form at the spinel tip,

crack advance halts until a new spinel layer forms ahead of such a cavity(ies). At this time the line of crack advance can switch.

11. Once the Ni- and S-rich thin films or islands melt or are amorphized, they lose their crystalline structure. The polyhedral crystal structure of the phase, such as the cage structure described by Ashby and Spaegen,<sup>84</sup> is broken. Then, the S atoms incorporated in the polyhedral cages diffuse away into the metal matrix.
12. Depending on postcracking thermal history, the degree of such back-diffusion of S atoms varies. Then, the S-to-Ni ratio and the distribution of S and Ni near voids and cavities observed in a post-cracking examination may vary significantly.

#### **3.1.4 Role of Carbon**

The role of carbon, which tends to suppress IASCC susceptibility at very low concentrations of S ( $\leq 0.002$  wt.%), is not well understood at this time. However, an attractive model that can explain the beneficial effect is based on a postulation that C atoms are dissolved in significant amounts in the Ni- and S-rich thin film. As shown by Heuer et al., a Ni- and S-rich thin film loses metallic strength when the S content in the film exceeds a threshold level.<sup>71</sup> Such a loss of metallic strength is attributed to severe localization of free electrons by S atoms incorporated in the Ni-S-type film, i.e., trapping of free electrons by S. When deprived of free electrons, the film no longer exhibits metallic behavior or metallic strength. A simple consideration suggests that C atoms can easily occupy the same octahedral sites in the unit cell of Ni sulfide that would be normally occupied by S atoms. Thus, when C concentration is high near the Ni- and S-rich thin film that is formed at the crack-tip grain boundary, S and C atoms compete to occupy the same octahedral sites. Under such a situation, C dissolved in the film is expected to promote a strong covalent bonding with Ni, in effect, suppressing the effect of trapping free electrons by S. The limited information available (presented in NUREG/CR-4667, Vol. 34) indicates that the solubility of C in a CuS- and NiS-type thin film is significant, which is consistent with, but does not prove, the model outlined above. A further investigation is desirable to provide a better mechanistic understanding of the role of C atoms on BWR IASCC.

### **3.2 Crack Growth Rate Test of Austenitic Stainless Steels Irradiated in the Halden Reactor (E. E. Gruber and O. K. Chopra)**

#### **3.2.1 Introduction**

Austenitic SSs are used extensively as structural alloys in reactor pressure vessel internal components because of their high strength, ductility, and fracture toughness. However, exposure to neutron irradiation for extended periods changes the microstructure and degrades the fracture properties of these steels. Irradiation leads to a significant increase in yield strength and reduction in ductility and fracture resistance of austenitic SSs.<sup>85-88</sup> Radiation can exacerbate the corrosion fatigue and stress corrosion cracking (SCC) behavior of SSs<sup>85,89,90</sup> by affecting the material microchemistry, e.g., radiation-induced segregation; material microstructure, e.g., radiation hardening; and water chemistry, e.g., radiolysis.

The factors that influence SCC susceptibility of materials include neutron fluence, cold work, corrosion potential, water purity, temperature, and loading. The effects of neutron fluence on IASCC of austenitic SSs has been investigated for BWR control blade sheaths<sup>91-93</sup> and laboratory tests on BWR-

irradiated material;<sup>89,94-96</sup> the extent of intergranular SCC increases with fluence. Although a threshold fluence level of  $5 \times 10^{20}$  n/cm<sup>2</sup> ( $E > 1$  MeV)\* ( $\approx 0.75$  dpa) has been proposed for austenitic SSs in BWR environments based on early experimental results, intergranular cracking has been seen at fluences as low as  $\approx 2 \times 10^{20}$  n/cm<sup>2</sup> ( $\approx 0.3$  dpa).<sup>89,97</sup> The results also show the beneficial effect of reducing the corrosion potential of the environment,<sup>98,99</sup> which suggests that the threshold fluence for IASCC is higher under low potential conditions such as BWR hydrogen water chemistry (HWC) or PWR primary water chemistry. However, low corrosion potential does not provide immunity to IASCC if the fluence is high enough, e.g., intergranular SCC has been observed in cold-worked, irradiated SS baffle bolts in PWRs.

A program is being conducted at ANL on irradiated SSs to support the regulatory request to understand better the safety issues attendant to the cracking of BWR internals such as core shrouds. The susceptibility of austenitic SSs to IASCC is being evaluated as a function of the fluence level, material composition, and water chemistry. Crack growth rate tests are being conducted on Types 304 and 316 SS base metal and weld HAZ irradiated to fluence levels up to  $2.0 \times 10^{21}$  n/cm<sup>2</sup> (3.0 dpa) at  $\approx 288^\circ\text{C}$  ( $550^\circ\text{F}$ ). The CGR tests are conducted in normal water chemistry (NWC) and HWC BWR environments at  $\approx 289^\circ\text{C}$ .

Crack growth tests have been completed on Types 304L and 316L SS (Heats C3 and C16, respectively) irradiated to a fluence level of 0.3, 0.9, and  $2.0 \times 10^{21}$  n/cm<sup>2</sup> (0.45, 1.35, and 3.0 dpa). The results indicate significant enhancement of CGRs for irradiated steels in the NWC BWR environment.<sup>100</sup> The CGRs of Type 304L SS irradiated to 1.35 and 3.0 dpa and Type 316L SS irradiated to 3.0 dpa were comparable and a factor of  $\approx 5$  higher than the disposition curve proposed in NUREG-0313<sup>101</sup> for sensitized austenitic SSs in water with 8 ppm DO. Type 304L SS irradiated to 0.45 dpa showed very little enhancement of CGRs in high-DO water. Also, for these irradiation levels, the CGRs under constant load were below the NUREG-0313 disposition curve for sensitized SSs.

The results also indicated that in low-DO BWR environments, the CGRs of the irradiated steels decreased by an order of magnitude in some tests, e.g., Type 304L SS irradiated to 1.35 dpa and Type 316L SS irradiated to 3.0 dpa. As noted previously, the benefit of low DO appears to decrease with increasing fluence. The beneficial effect of decreased DO was not observed in a test on Type 304L SS Heat C3 irradiated to 3.0 dpa, although it is possible that this different behavior is associated with the loss of constraint in the specimen due to the high applied load.<sup>100</sup>

This annual report presents experimental CGR data in BWR environments at  $289^\circ\text{C}$  for SS weld HAZ specimens irradiated to  $0.5 \times 10^{21}$  n/cm<sup>2</sup> (0.75 dpa). The HAZ specimens were obtained from the H5 core-shroud weld of the cancelled GG reactor and an SMA weld prepared from a 30-mm plate of Type 304 SS (Heat 10285). Baseline data were obtained on nonirradiated SS weld HAZ specimens; the results were presented earlier.<sup>102</sup> Also, a detailed metallographic examination of the fracture surface of Type 304L SS specimen C3-C (irradiated to 3.0 dpa) was performed to determine whether the lack of beneficial effect of HWC observed for this specimen was associated with the possible loss of constraint due to the high applied load.

### 3.2.2 Experimental

The CGR tests were performed at  $\approx 289^\circ\text{C}$  on 1/4-T CT specimens in simulated BWR environments in accordance with ASTM E-647 and ASTM E-1681. The configuration of the specimens is shown in

1. \_\_\_\_\_

\* All references to fluence levels are calculated for  $E \geq 1$  MeV.

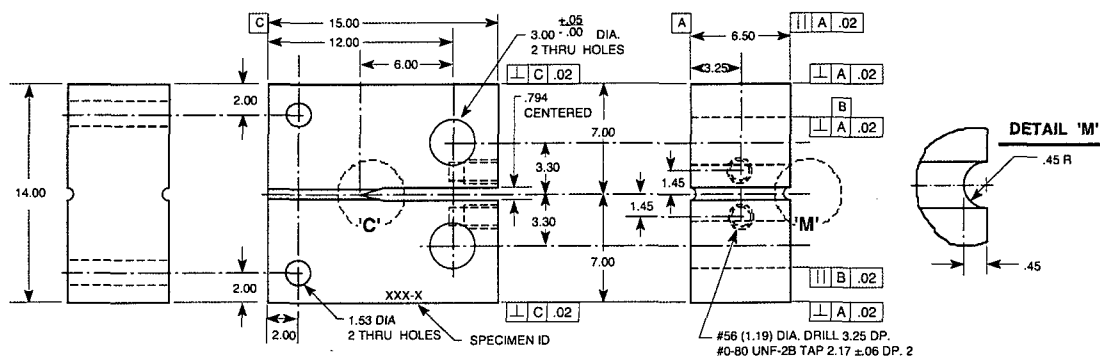


Figure 12. Configuration of compact-tension specimen for this study (dimensions in mm).

Table 2. Composition (wt.%) of Type 304 stainless steels investigated.

Steel												
Type	Heat ID	Analysis	Ni	Si	P	S	Mn	C	N	Cr	Mo	O
304	10285	Vendor	8.40	0.51	0.032	0.006	1.64	0.058	—	18.25	0.41	—
		ANL	8.45	0.60	0.015	0.007	1.90	0.070	0.084	18.56	0.51	0.013
304L	GG Top Shell	ANL	9.05	0.53	0.027	0.016	1.84	0.013	0.064	18.23	0.44	0.010
		GG Bottom Shell	ANL	8.95	0.55	0.023	0.008	1.80	0.015	0.067	18.62	0.31

Fig. 12. Crack extensions were determined by DC potential measurements. The GG H5 weld was fabricated from SA 240 Type 304L hot-rolled plate having a double-V joint design and welded by the SA method with ER308L filler metal. The SMA weld was prepared in the laboratory by welding two 70 x 178 mm (2.75 x 7.0 in.) pieces of 30-mm thick (1.18-in. thick) plate. The composition of the SSs used in the present study is presented in Table 2. The specimens were machined from 9.5-mm thick slices of the weld; before machining, some slices were thermally treated for 24 h at 500°C (932°F) to simulate long term aging during service. For all specimens, the machined notch was located in the HAZ of the weld. Each slice was etched, and the specimen orientation and notch location relative to the weld were clearly identified. Details regarding the facility and procedure for conducting the tests and material characterization were presented earlier.<sup>102</sup>

There are a few potential differences between the GG SA weld HAZ and laboratory-prepared SMA weld HAZ, e.g., microstructure and residual strain. The HAZ of high-C austenitic SS welds typically consists of a sensitized microstructure. The low-C grades of SSs are considered to be resistant to weld sensitization. A transmission electron microscopy (TEM) study of the HAZ in the GG Type 304L vertical core shroud weld revealed a few, very small Cr-rich precipitates at the grain boundaries about 1 and 3 mm from the fusion line; most boundaries showed no precipitates.<sup>103</sup> Thus, only the laboratory-prepared weld HAZ is likely to have a sensitized microstructure. The residual strain in various SS weld HAZs has been measured by the electron back scattered pattern technique.<sup>103-106</sup> The results indicate that the peak strains typically extend up to 5 mm from the fusion line and range from 8 to 20%. Residual strains up to 10% have been measured in the Type 304L vertical core shroud weld HAZ from the GG reactor.<sup>103</sup> Similar information for the laboratory-prepared weld HAZ is not available. Also, because the heat input per pass for SA welds is typically higher than for SMA welds of comparable geometry, the HAZ associated with a SA weld is wider than that associated with a SMA weld.

Table 3. Tensile properties (MPa) of the austenitic stainless steels irradiated in the Halden reactor.

Steel Type	Material Condition	Nonirradiated		Fluence $5 \times 10^{20}$ n/cm <sup>2</sup>	
		Yield	Ultimate	Yield	Ultimate
304 SS Heat 10285	Mill annealed	196	508	–	–
	MA + 10.5 h at 600°C	156	501	(531)	(680)
304L SS GG Core Shroud	Mill annealed	158	411	–	–
	MA + 10.5 h at 600°C	159	425	(533)	(610)

Estimated values within parentheses, yield stress determined from Eq. 20 and ultimate stress from data obtained on similar heats in Ref. 108. To convert MPa to ksi multiply by 0.145.

The tensile properties of the GG core shroud shell and Heat 10285, in the mill-annealed condition and after sensitization at 600°C (1112°F) for 10.5 h, are listed in Table 3. The tests were conducted on cylindrical specimens, 5.1-mm diameter and 20.3 mm gauge length, in air at 289°C and 0.008 %/s strain rate. The sensitization heat treatment had little effect on the tensile strength of the GG steel, whereas the strength of Heat 10285 was decreased. For the irradiated SSs, the yield stress was estimated from the correlation developed by Odette and Lucas<sup>107</sup>; the increase in yield stress (MPa) is expressed in terms of the fluence (dpa) by the relationship

$$\Delta\sigma_y = 670 [1 - \exp(-\text{dpa}/2)]^{0.5}. \quad (20)$$

The ultimate stresses for the irradiated steels were estimated from the data in Ref. 108. The tensile yield and ultimate stresses for the irradiated SSs are also given in Table 3. The tensile properties of the sensitized material were used to determine the K/size criterion for nonirradiated and irradiated HAZ specimens, both in the as-welded and as-welded plus thermally-treated conditions.

All specimens were fatigue precracked in the test environment at temperature and load ratio  $R = 0.2-0.3$ , frequency = 1–5 Hz, and  $K_{\text{max}} \approx 15 \text{ MPa m}^{1/2}$  (13.64 ksi in<sup>1/2</sup>). After 0.3–0.5 mm (12–20 mil) crack extension,  $R$  was increased incrementally to 0.7, and the loading waveform changed to a slow/fast sawtooth with rise times of 30–1000 s. The loading history was then changed to a trapezoidal waveform,  $R = 0.7$ , hold period at peak of 1 or 2 h, and unload/reload period of 24 s to measure SCC growth rates. For some specimens, CGRs were also obtained under constant load. During individual test periods,  $K_{\text{max}}$  was maintained approximately constant by periodic load shedding (less than 2% decrease in load at any given time).

Under cyclic loading, the CGR (m/s) can be expressed as the superposition of the rate in air (i.e., mechanical fatigue) and the rates due to corrosion fatigue and SCC, given as

$$\dot{a}_{\text{env}} = \dot{a}_{\text{air}} + \dot{a}_{\text{cf}} + \dot{a}_{\text{SCC}}. \quad (21)$$

The CGRs in air,  $\dot{a}_{\text{air}}$  (m/s), were determined from the correlations developed by James and Jones<sup>109</sup>; it is expressed as

$$\dot{a}_{\text{air}} = C_{\text{SS}} S(R) \Delta K^{3.3}/T_R, \quad (22)$$

where  $R$  is the load ratio ( $K_{\text{min}}/K_{\text{max}}$ ),  $\Delta K$  is  $K_{\text{max}} - K_{\text{min}}$  in  $\text{MPa m}^{1/2}$ ,  $T_R$  is the rise time (s) of the loading waveform, and function  $S(R)$  is expressed in terms of the load ratio  $R$  as follows:

$$\begin{array}{ll}
S(R) = 1.0 & R < 0 \\
S(R) = 1.0 + 1.8R & 0 < R < 0.79 \\
S(R) = -43.35 + 57.97R & 0.79 < R < 1.0.
\end{array} \tag{23}$$

Function  $C_{SS}$  is given by a third-order polynomial of temperature  $T$  ( $^{\circ}\text{C}$ ), expressed as

$$C_{SS} = 1.9142 \times 10^{-12} + 6.7911 \times 10^{-15} T - 1.6638 \times 10^{-17} T^2 + 3.9616 \times 10^{-20} T^3. \tag{24}$$

Environmental effects on fatigue crack growth of nonirradiated austenitic SSs have been investigated by Shack and Kassner.<sup>110</sup> In the absence of any significant contribution of SCC to growth rate, the CGRs in water with  $\approx 0.3$  ppm DO are best represented by the expression

$$\dot{a}_{env} = \dot{a}_{air} + 4.5 \times 10^{-5} (\dot{a}_{air})^{0.5}, \tag{25}$$

and in water with  $\approx 8$  ppm DO by the expression,

$$\dot{a}_{env} = \dot{a}_{air} + 1.5 \times 10^{-4} (\dot{a}_{air})^{0.5}. \tag{26}$$

The CGR (m/s) under SCC conditions is represented by the correlation given in the U.S. NRC report NUREG-0313, Rev. 2,<sup>101</sup>

$$\dot{a}_{SCC} = A (K)^{2.161}, \tag{27}$$

where  $K$  is the stress intensity factor ( $\text{MPa m}^{1/2}$ ), and the magnitude of constant  $A$  depends on the water chemistry and composition and structure of the steel. A value of  $2.1 \times 10^{-13}$  for constant  $A$  has been proposed in NUREG-0313 for sensitized SS in water chemistries with 8 ppm DO. The magnitude of constant  $A$  will be smaller in low-DO environments, such as HWC BWR or PWR environments.

All tests were started in high-purity water that contained 250–500 ppb DO (i.e., NWC BWR environment). The electrochemical potential (ECP) of a Pt electrode and a SS sample located at the exit of the autoclave was monitored continuously during the test; the water DO level and conductivity were determined periodically. After data were obtained for high-DO water, the DO level in the feedwater was decreased to  $< 30$  ppb by sparging the feedwater with pure  $\text{N}_2$  or  $\text{N}_2 + 5\% \text{H}_2$ . Because of the very low water flow rates, it took several days for the environmental conditions to stabilize for the in-cell tests. In general, the changes in ECP of the SS sample were slower than in the ECP of the Pt electrode. Because of higher flow rates, the changes in water chemistry for the out-of-cell tests were significantly faster.

After the test the final crack size was marked by fatigue cycling in air at room temperature. The specimens were then fractured, and the fracture surface of both halves of the specimen was photographed with a telephoto lens through the hot cell window. The fracture surfaces of the out-of-cell test specimens were examined by scanning electron microscopy (SEM). The final crack length of each half of the fractured specimen was determined from the optical or SEM photograph by the 9/8 averaging technique, i.e., nine measurements were taken across the width of the specimen at equal intervals, the two near-surface measurements were averaged, and the resultant value was averaged with the remaining seven measurements. The results were used to correct the crack length measurements, e.g., the crack extensions determined from the DC potential drop method were proportionately scaled to match the final optically measured crack length.

The CGR during each test period was determined from the slope of the corrected crack length vs. time plots; for cyclic loading, only the rise time was used to determine growth rate. The crack extension during each test period was at least 10 times the resolution of the DC potential drop method, i.e., typically 5  $\mu\text{m}$ . Thus, crack extensions were at least 50  $\mu\text{m}$ ; for test periods with very low CGRs, e.g., less than  $1 \times 10^{-11}$  m/s, smaller crack extensions were used to reduce testing time.

The CGR test results were validated in accordance with the specimen size criteria of ASTM E 1681 and E 647. These criteria require that the plastic zone at the tip of a fatigue crack is small relative to the specimen geometry. The ASTM specifications for specimen K/size criteria are intended to ensure applicability and transferability of the cracking behavior of a component or specimen of a given thickness under a specific loading condition to a crack associated with a different geometry, thickness, and loading condition. For constant load tests, ASTM E 1681 requires that

$$B_{\text{eff}} \text{ and } (W - a) \geq 2.5 (K/\sigma_{\text{ys}})^2, \quad (28)$$

where  $K$  is the applied stress intensity factor,  $\sigma_{\text{ys}}$  is the yield stress of the material,  $a$  is crack length,  $W$  is the specimen width, and specimen effective thickness  $B_{\text{eff}}$  is defined in terms of the specimen thickness  $B$  and net thickness  $B_{\text{N}}$  expressed as  $(B B_{\text{N}})^{0.5}$ . For high strain-hardening materials, i.e., materials with an ultimate-to-yield stress ratio  $(\sigma_{\text{ult}}/\sigma_{\text{ys}}) \geq 1.3$ , both criteria allow the use of the flow stress defined as  $\sigma_f = (\sigma_{\text{ult}} + \sigma_{\text{ys}})/2$  rather than the yield stress.

The K/size criteria were developed for materials that show work hardening and, therefore, may not be valid for materials irradiated to fluence levels where, on a local level, they do not strain harden. This lack of strain hardening, or strain softening, is most dramatic when dislocation channeling occurs, but may also occur at lower fluences. For moderate to highly irradiated material, an effective yield stress, defined as the average of the nonirradiated and irradiated yield stresses has been suggested<sup>11</sup>; this discounts the irradiation-induced increase in yield stress by a factor of 2. In the present study, because of the relatively low level of irradiation, flow stress was used to determine the allowed  $K_{\text{max}}$  for both nonirradiated and irradiated SS weld HAZ specimens.

### 3.2.3 Crack Growth Tests on Irradiated Stainless Steels in BWR Environments

Crack growth tests have been completed in BWR environments at 289°C on 1/4-T CT specimens of Types 304L and 304 SS HAZs irradiated to  $5.0 \times 10^{20}$  n/cm<sup>2</sup> ( $\approx 0.75$  dpa). The specimens for the tests were obtained from the top shell Type 304L SS HAZ of the GG core shroud H5 SA weld (Specimens GG5T-A and GG5T-B) and from the HAZ of a laboratory-prepared Type 304 SS SMA weld in two conditions, e.g., as-welded (Specimen 85-7A) and as-welded plus thermally-treated for 24 h at 500°C (Specimen 85-1A-TT). The significant results for the various tests are summarized below.

#### 3.2.3.1 Specimen GG5T-A of Type 304L SS HAZ, Test CGRI-15

The Specimen GG5T-A test was started in high-purity water with  $\approx 250$  ppb DO and  $\approx 10$  mL/min flow rate. The environmental and loading conditions, experimental CGRs, the allowed  $K_{\text{max}}$  from K/size criterion, and the margin between the applied  $K_{\text{max}}$  and the allowed value are given in Table 4. The changes in crack length and  $K_{\text{max}}$  with time during various test periods are shown in Fig. 13. Precracking was carried out at  $R \approx 0.2-0.3$ ,  $K_{\text{max}} = 12.5-13.5$  MPa m<sup>1/2</sup>, and triangular waveform with 1 Hz frequency. After  $\approx 0.2$ -mm extension,  $R$  was increased incrementally to 0.7, and the loading waveform changed to a slow/fast sawtooth with rise times of 60-1000 s. For this specimen, environmental enhancement occurred after  $\approx 200$  h during test period 3b (Fig. 13a).



Table 4. Crack growth results for Specimen GG5T-A<sup>a</sup> of Type 304L HAZ in high-purity water at 289°C.

Test Period <sup>b</sup>	Test Time, h	ECP, <sup>c</sup> mV (SHE) Pt Steel	O <sub>2</sub> Conc., <sup>c</sup> ppb	R Load Ratio	Rise Time, s	Down Time, s	Hold Time, s	K <sub>max</sub> , MPa·m <sup>1/2</sup>	ΔK, MPa·m <sup>1/2</sup>	Growth Rate, m/s	Allowed K <sub>max</sub> , MPa·m <sup>1/2</sup>	Margin in K <sub>max</sub> , <sup>d</sup> %	
1	69	212	205	250	0.17	0.5	0.5	0	13.1	10.8	1.71E-08	28.1	-54
2a	74	212	205	250	0.28	0.5	0.5	0	13.0	9.3	3.11E-09	28.0	-54
2b	144	214	201	250	0.30	0.5	0.5	0	13.4	9.4	2.70E-09	28.0	-52
2c	165	214	201	250	0.32	0.5	0.5	0	14.2	9.7	1.06E-08	27.8	-49
3a	194	213	195	250	0.52	60	4	0	15.0	7.2	4.30E-11	27.8	-46
3b*	215	213	195	250	0.52	60	4	0	16.2	7.8	1.61E-09	27.6	-42
4*	260	209	196	250	0.69	300	4	0	15.5	4.8	3.34E-10	27.5	-44
5*	305	207	196	250	0.69	1000	12	0	15.5	4.8	3.89E-10	27.4	-43
6	355	206	196	250	0.70	60	12	0	16.2	4.8	3.01E-11	27.3	-41
7	378	205	199	250	0.71	60	12	0	17.6	5.1	8.03E-11	27.2	-35
8	482	199	193	250	0.51	30	4	0	17.5	8.6	8.57E-11	27.2	-35

<sup>a</sup>Grand Gulf H5 SA weld top shell HAZ, irradiated to  $5.0 \times 10^{20}$  n/cm<sup>2</sup>.

<sup>b</sup>An asterisk indicates environmental enhancement of growth rates under cyclic loading.

<sup>c</sup>Represents values in the effluent. Conductivity was  $\approx 0.07$  and  $0.2 \mu\text{S/cm}$  in feedwater and effluent, respectively.

<sup>d</sup>Based on flow stress.

After 305 h, the specimen was overstrained to  $\approx 16.5 \text{ MPa m}^{1/2}$  due to a power bump. Although the loading systems are interlocked to shut down in case of a power failure, for the small specimens used in the irradiated tests, the internal pressure is sufficient to overload the specimen. The enhanced growth rates observed prior to the interruption could not be restored even after  $K_{\text{max}}$  was increased to  $16.6 \text{ MPa m}^{1/2}$ . The crack may have side branched due to overstrain, and the crack length and loading conditions may no longer be accurately characterized; therefore, the test was terminated after  $\approx 480$  h. Post-test measurements of the final crack front were not performed for this specimen. The specimen is intact and could potentially be used to continue the CGR test.

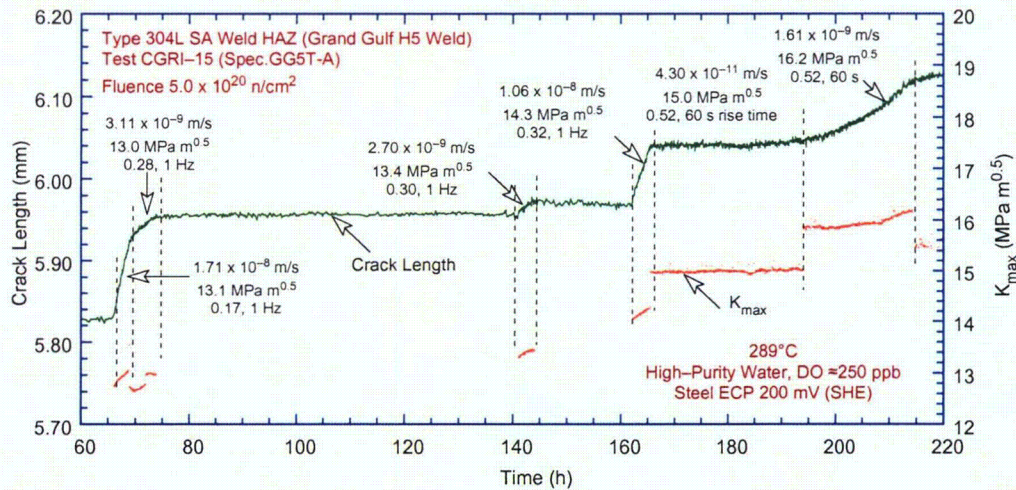


Figure 13. Crack-length-vs.-time plots for irradiated H5 weld HAZ Specimen GG5T-A in high-purity water at 289°C during test periods (a) precracking-3, (b) 4-6, and (c) 7-8.

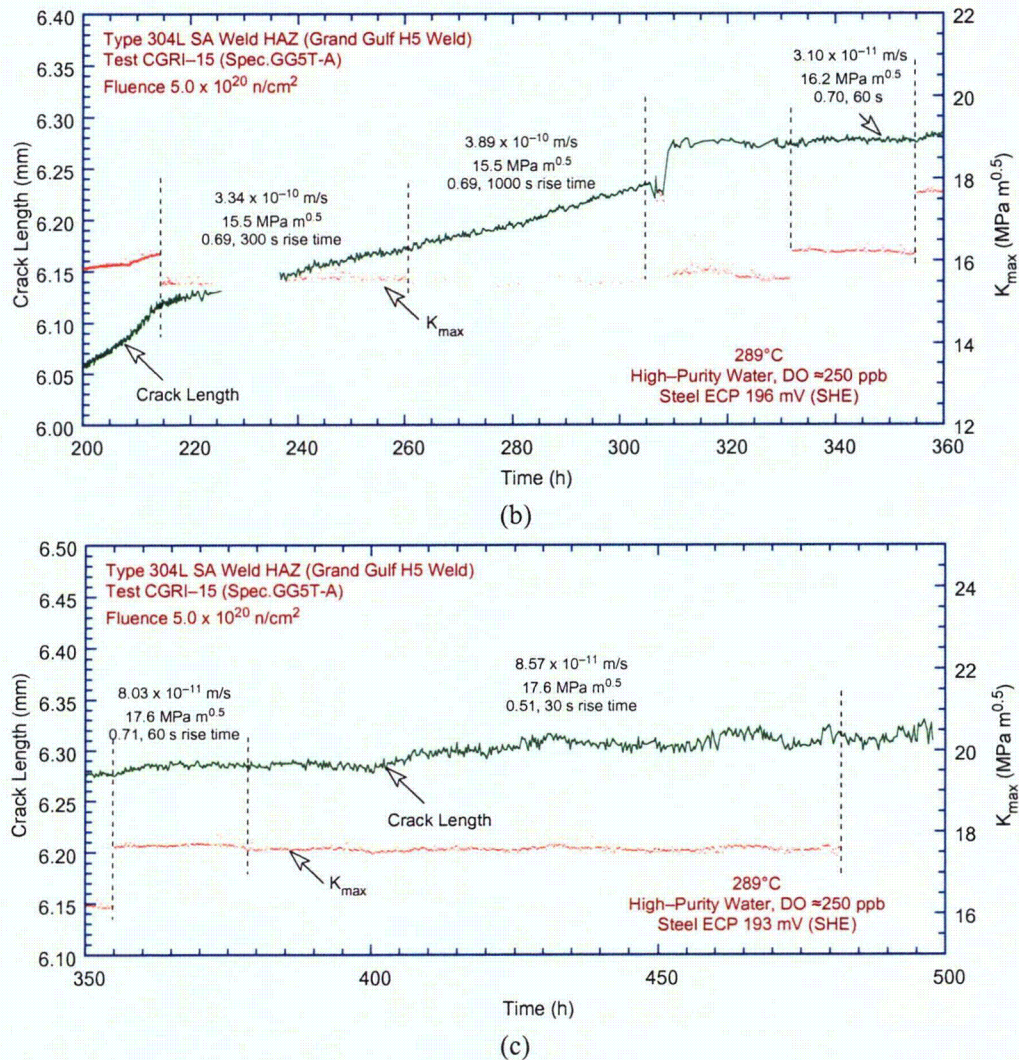


Figure 13 (Contd.)

### 3.2.3.2 Specimen GG5T-B of Type 304L SS HAZ, Test CGRI-16

The Specimen GG5T-B test was started in high-purity water with  $\approx 350$  ppb DO and  $\approx 10$  mL/min flow rate. The test conditions, experimental CGRs, the allowed  $K_{max}$  from K/size criterion, and the margin between the applied  $K_{max}$  and the allowed value are given in Table 5. The changes in crack length and  $K_{max}$  with time during various test periods are shown in Fig. 14. Precracking was carried out at  $R \approx 0.2-0.3$ ,  $K_{max} \approx 13.0$  MPa  $m^{1/2}$  (11.82 ksi in<sup>1/2</sup>), and triangular waveform with 1 Hz frequency. After  $\approx 0.2$ -mm extension,  $R$  was increased to 0.5, and the loading waveform was changed to a slow/fast sawtooth with rise times of 30-300 s. Finally,  $R$  was increased to 0.7. For this specimen environmental enhancement occurred after  $\approx 125$  h during test period 2b (Fig. 14a).

After  $\approx 575$  h, the DO level in the feedwater was decreased from  $\approx 350$  ppb to  $< 30$  ppb by sparging the feedwater tank with  $N_2$  plus 5%  $H_2$  gas mixture. The change in crack length and ECP of Pt and SS electrodes during the transient periods is shown in Fig. 15. The change in ECP was relatively fast; the ECP decreased to  $-400$  mV (SHE) in  $\approx 5$  h for the Pt electrode, and it decreased to approximately

Table 5. Crack growth results for Specimen GG5T-B<sup>a</sup> of Type 304L HAZ in high-purity water at 289°C.

Test Period <sup>b</sup>	Test Time, h	ECP, <sup>c</sup> mV (SHE)		O <sub>2</sub> Conc., <sup>c</sup> ppb	R Load Ratio	Rise Time, s	Down Time, s	Hold Time, s	K <sub>max</sub> , MPa·m <sup>1/2</sup>	ΔK, MPa·m <sup>1/2</sup>	Growth Rate, m/s	Allowed K <sub>max</sub> , MPa·m <sup>1/2</sup>	Margin in K <sub>max</sub> , <sup>d</sup> %
Pre	81	225	211	350	0.20	0.50	0.5	0	14.5	11.6	7.24E-09	28.1	-48
1	105	218	200	350	0.30	0.50	0.5	0	13.7	9.6	4.59E-09	28.0	-51
2a	122	216	206	350	0.50	60	4	0	13.4	6.7	negligible	28.0	-52
2b*	154	214	199	350	0.51	30	4	0	15.2	7.4	9.13E-10	27.8	-45
3*	221	211	199	350	0.49	300	4	0	15.5	7.9	2.82E-10	27.6	-44
4*	296	204	200	350	0.70	300	4	0	15.6	4.7	2.35E-10	27.4	-43
5*	362	229	200	350	0.68	1,000	12	0	15.5	5.0	2.98E-10	27.2	-43
6	433	201	176	350	0.69	300	12	3,600	15.6	4.8	6.75E-10	26.7	-42
7	530	220	204	350	1.00	-	-	-	15.9	0.0	4.24E-10	26.4	-40
8	584	215	202	350	0.69	300	12	9,700	16.1	5.0	5.62E-10	26.1	-38
9	724	-532	-285	350	0.69	300	12	9,700	15.8	4.9	negligible	26.0	-39
10	893	-533	-530	350	0.69	300	12	-	15.9	4.9	negligible	26.0	-39

<sup>a</sup>Grand Gulf H5 SA weld top shell HAZ, irradiated to  $5.0 \times 10^{20}$  n/cm<sup>2</sup>.

<sup>b</sup>An asterisk indicates environmental enhancement of growth rates under cyclic loading.

<sup>c</sup>Represents values in the effluent. Conductivity was  $\approx 0.07$  and  $0.2 \mu\text{S}/\text{cm}$  in feedwater and effluent, respectively.

<sup>d</sup>Based on flow stress.

-200 mV in 24 h and then gradually to -550 mV in the next  $\approx 300$  h for the SS electrode. In the low-DO environment, crack growth essentially stopped under both trapezoidal and saw-tooth loading waveforms.

After the test, the final crack size was marked by fatigue cycling at room temperature in air. The specimen was then fractured, and the fracture surface of both halves of the specimen was photographed with a telephoto lens through the cell window. A photomicrograph of the fracture surface of both halves of the specimen is shown in Fig. 16. The final crack length was measured from the photograph by the 9/8 averaging technique; the difference in measured and estimated crack lengths was  $<5\%$ .

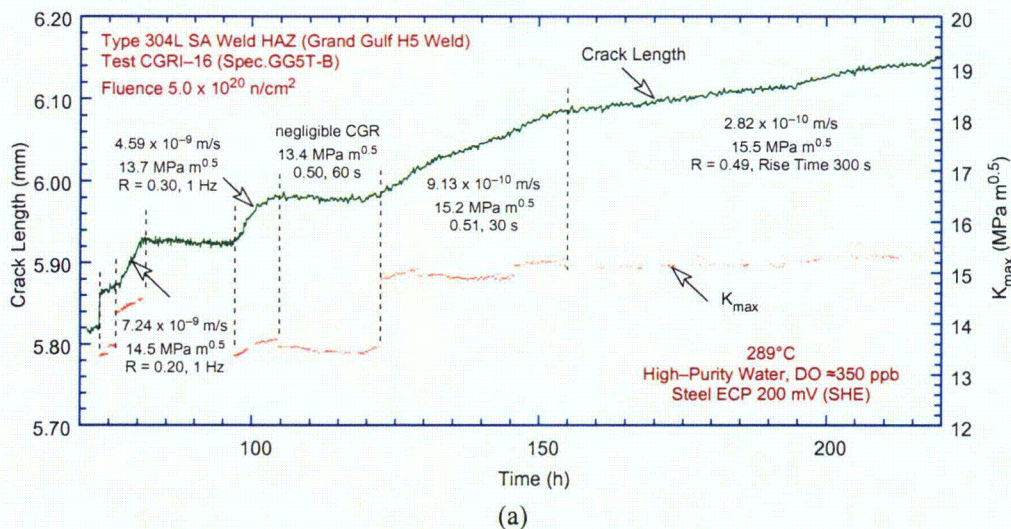
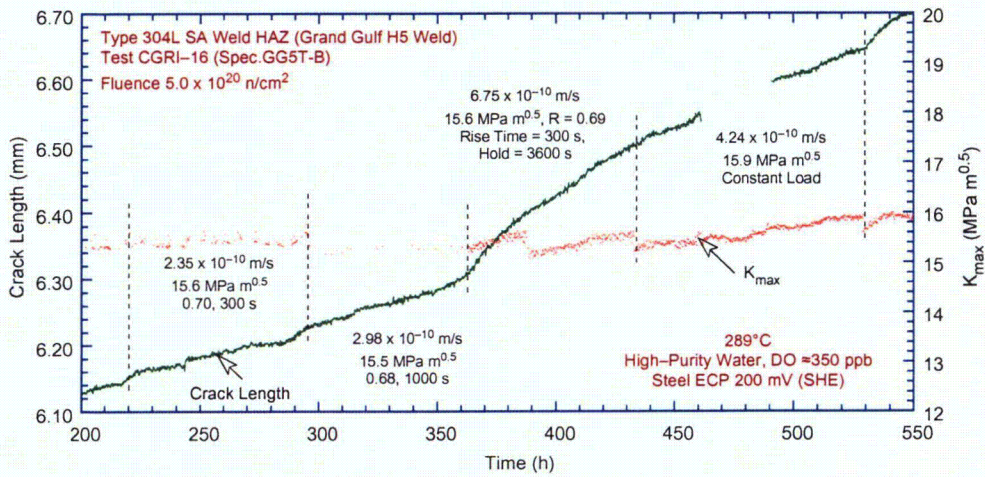
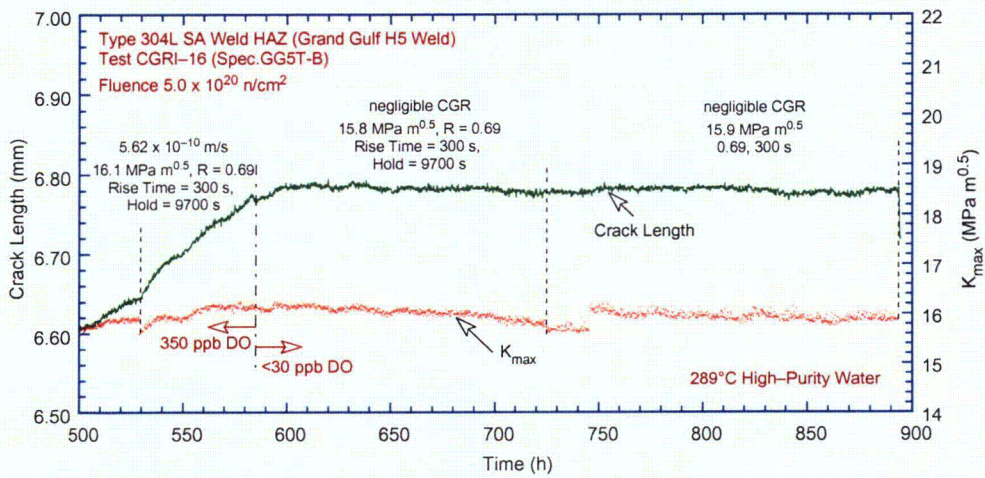


Figure 14. Crack-length-vs.-time plots for irradiated H5 weld HAZ Specimen GG5T-B in high-purity water at 289°C during test periods (a) precracking-3, (b) 4-7, and (c) 8-10.



(b)



(c)

Figure 14. (Contd.)

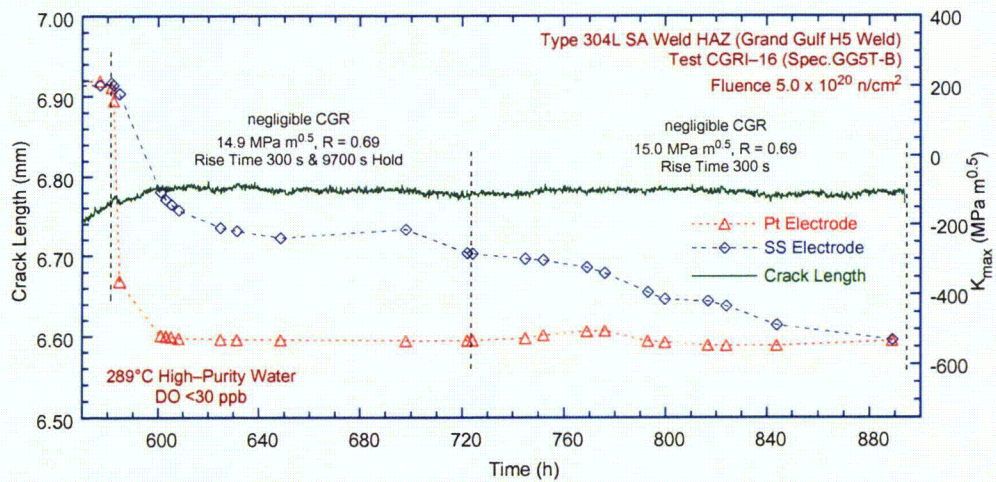


Figure 15. Change in crack length and ECP of Pt and SS electrodes when the DO level in feedwater was decreased from ≈350 to <30 ppb.

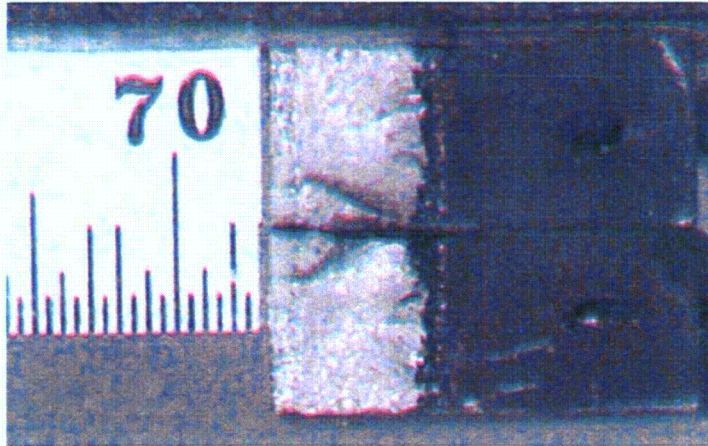


Figure 16.  
Photomicrograph of the fracture surface  
of Specimen GG5T-B.

### 3.2.3.3 Specimen 85-1A-TT of Type 304 SS HAZ, Test CGRI-18

The Specimen 85-1A-TT test was started in high-purity water with  $\approx 200$  ppb DO and flow rate of  $\approx 10.0$  mL/min. The test conditions, experimental CGRs, the allowed  $K_{\max}$  from the K/size criterion, and the margin between the applied and allowed values of  $K_{\max}$  are given in Table 6.

Precracking was carried out at  $R \approx 0.2$ ,  $K_{\max} \approx 13.5$  MPa  $m^{1/2}$  (12.27 ksi  $in^{1/2}$ ), and triangular waveform with 1 or 2 Hz frequency. After  $\approx 0.25$ -mm extension, R was increased to 0.7, and the loading waveform changed to a slow/fast sawtooth with rise times of 60–1000 s. After  $\approx 600$  h the feedwater cover gas was changed from a mixture of  $N_2 + 1\%$   $O_2$  to  $N_2 + 5\%$   $H_2$ . The changes in crack length and ECP of Pt and SS electrodes during the transient period are shown in Fig. 17. During test period 7, the ECP decreased to below  $-500$  mV (SHE) within 10 h for the Pt electrode and decreased to below  $-200$  mV (SHE) after  $\approx 48$  h for the SS sample. In low-DO water, the CGR, under the same loading condition, decreased by a factor of  $\approx 5$  relative to that in high-DO water.

Table 6. Crack growth results for Specimen 85-1A-TT<sup>a</sup> of Type 304 SS SMA weld HAZ in high-purity water at 289°C.

Test Period <sup>b</sup>	Test Time, h	ECP, <sup>c</sup> mV (SHE)		$O_2$ Conc., <sup>c</sup> ppb	R Load Ratio	Rise Time, s	Down Time, s	Hold Time, s	$K_{\max}$ , MPa $m^{1/2}$	$\Delta K$ , MPa $m^{1/2}$	Growth Rate, m/s	Allowed $K_{\max}$ , MPa $m^{1/2}$	Margin in $K_{\max}$ , <sup>d</sup> %
		Pt	Steel										
Pre a	98	229	163	200	0.17	0.25	0.25	0	14.7	12.2	2.64E-08	30.5	-52
Pre b	101	228	161	200	0.24	0.50	0.50	0	14.0	10.7	2.10E-08	30.3	-54
1a	145	213	166	200	0.50	60	4	0	15.4	7.7	negligible	30.3	-49
1b*	217	203	175	200	0.50	1,000	4	0	16.0	8.0	4.80E-10	30.2	-47
2*	262	201	178	200	0.70	300	4	0	17.0	5.1	3.55E-10	29.9	-43
3*	314	199	172	250	0.71	1,000	12	0	17.3	5.0	3.37E-10	29.8	-42
4	411	197	182	250	0.70	300	12	3,600	17.6	0.0	2.55E-10	29.5	-40
5	479	203	188	250	0.70	300	12	9,700	17.6	0.0	1.74E-10	29.4	-40
6	605	175	185	250	0.70	300	12	9,700	19.8	0.0	2.78E-10	29.1	-32
7	746	-526	-258	<30	0.70	300	12	9,700	20.5	0.0	5.73E-11	29.0	-30

<sup>a</sup>Laboratory-prepared Type 304 SS (Heat 10285) SMA weld HAZ, irradiated to  $5.0 \times 10^{20}$  n/cm<sup>2</sup>.

<sup>b</sup>An asterisk indicates environmental enhancement of growth rates under cyclic loading.

<sup>c</sup>Represents values in the effluent. Conductivity was  $\approx 0.07$  and  $0.2$   $\mu S/cm$  in feedwater and effluent, respectively.

<sup>d</sup>Based on flow stress.

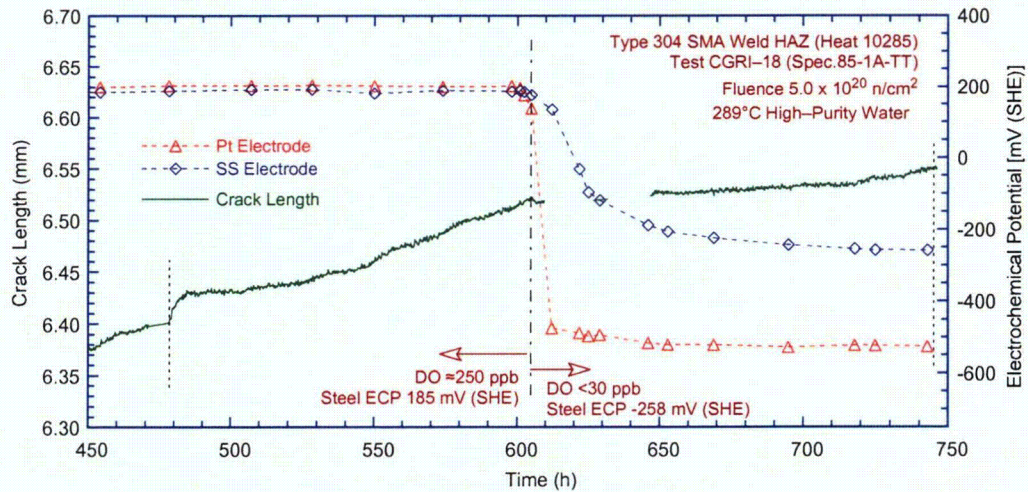


Figure 17. Change in crack length and ECP of Pt and SS electrodes when the DO level in feedwater was decreased from  $\approx 250$  to  $< 30$  ppb.

After the CGR test was completed, a J-R curve test was performed on the same specimen at  $289^{\circ}\text{C}$  in high-purity water with  $\approx 250$  ppb DO. The test was conducted at a constant extension rate in accordance with ASTM specification E 1737 for "J-Integral Characterization of Fracture Toughness." The test was interrupted periodically (by holding the specimen at constant strain) to measure the crack length by the DC potential drop method. Specimen extension was monitored and controlled outside the high-temperature zone.

After the J-R curve test, the final crack front was marked by fatigue cycling at room temperature in air. The specimen was then fractured, and the fracture surface of both halves of the specimen was photographed with a telephoto lens through the cell window (Fig. 18). The final crack length was measured from the photograph by the 9/8 averaging technique; the difference in measured and estimated crack lengths was  $< 5\%$ . The crack extensions estimated from the DC potential drop method were 0.71 and 0.82 mm for the CGR and J-R curve test portions, respectively.

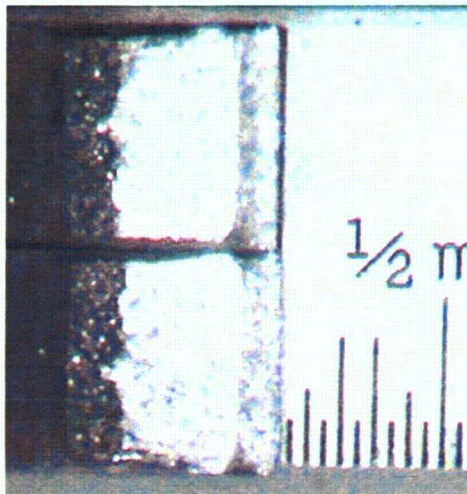


Figure 18. Photomicrograph of the fracture surface of Specimen 85-1A-TT.

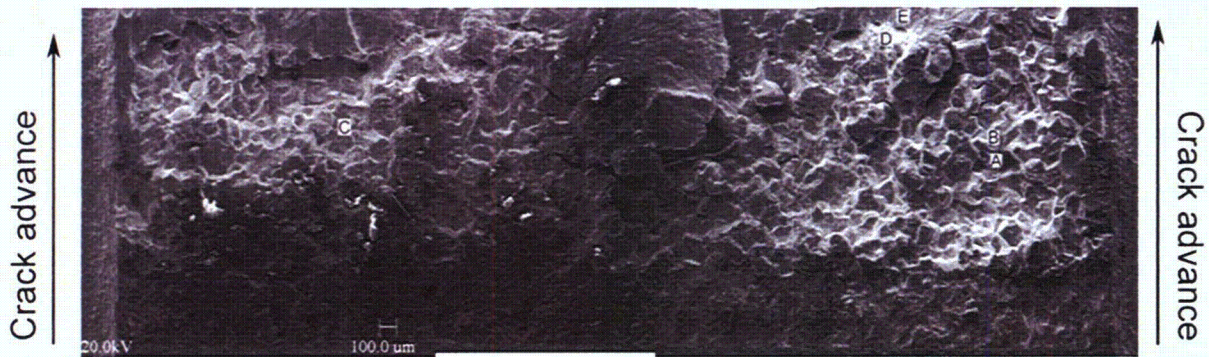
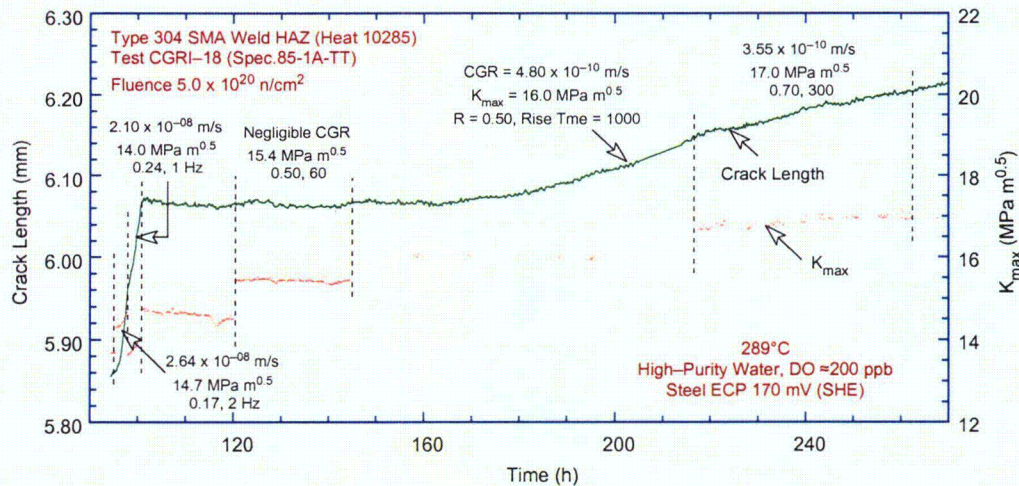


Figure 19. Micrograph of the fracture surface of Specimen 85-1A-TT tested in BWR environments.

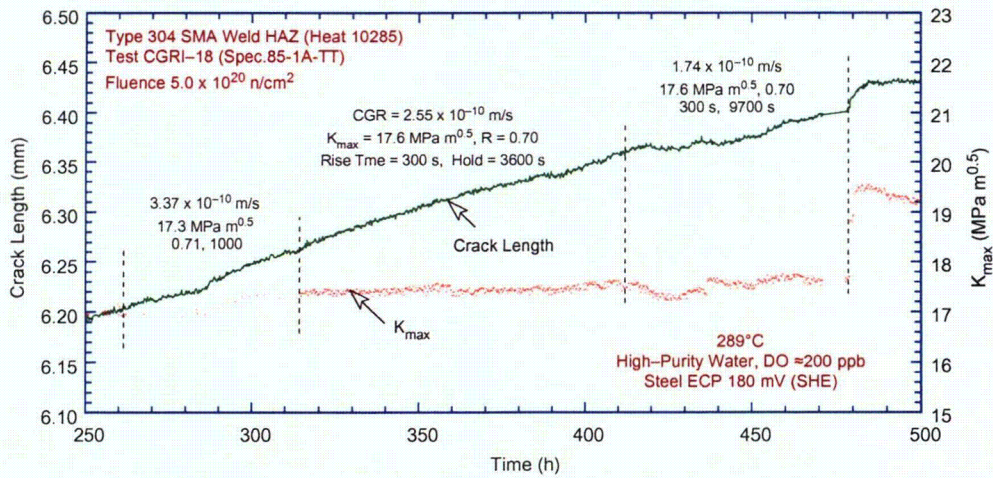
The fracture surface was also examined by SEM to verify the crack extensions during CGR and J-R tests and to characterize the fracture morphology. A micrograph of the entire crack extension, i.e., for both the CGR and J-R curve test, is shown in Fig. 19; high magnification micrographs of areas marked A–E are shown later in Figs. 21–23. Once again, the crack front is relatively straight. Measurements of the final crack length show very good agreement with the values estimated from the DC potential drop method and those measured earlier from photographs of the fracture surface; the difference in measured and estimated crack lengths was <5%.

The changes in crack length and  $K_{max}$  with time during various test periods are shown in Fig. 20. In general, the DC potential measurements show very little scatter; the fluctuations in  $K_{max}$  at 400–600 h were caused by changes in the system pressure. For this specimen, environmental enhancement occurred after  $\approx 190$  h during test period 1b (Fig. 20a). Also, the results in Table 6 indicate that for this specimen, the applied  $K_{max}$  during all test periods was within the values allowed by the K/size criterion.

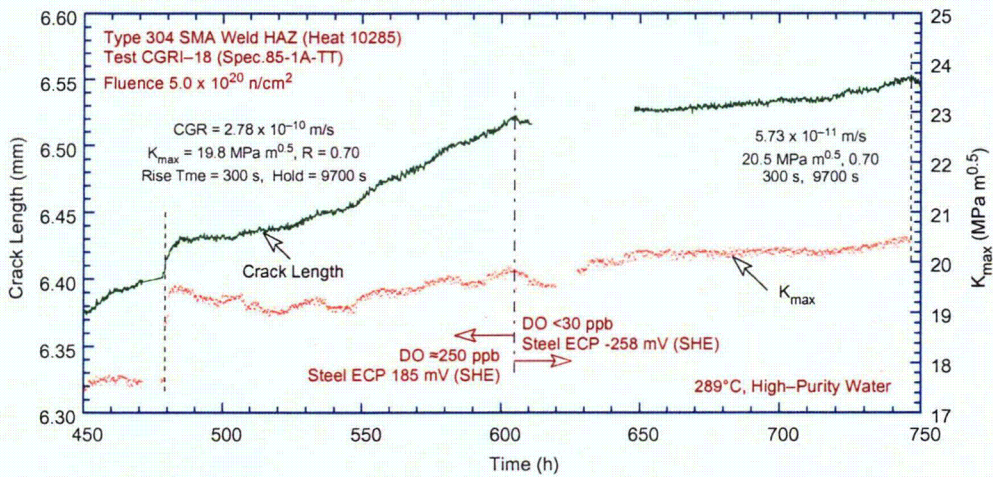


(a)

Figure 20. Crack-length-vs.-time plots for irradiated SMA weld HAZ Specimen 85-1A-TT in high-purity water at 289°C during test periods (a) 1–2, (b) 3–5, and (c) 6–7.



(b)



(c)

Figure 20 (Contd.)

A significant feature of the fracture surface is the essentially intergranular (IG) nature of the fracture during the J-R curve test in high-DO water, in contrast to the ductile fracture morphology expected in a J-R test in air. High magnification micrographs at locations A-E in Fig. 19 are shown in Figs. 21-23. These locations correspond to the portion of the fracture surface associated with the J-R curve test. All except location E, which is near the end of the test, show predominantly IG fracture. Some facets show an increased degree of deformation (e.g., Fig. 21), and occasional TG areas occur with stepped or terrace-like fracture planes.

A section of the entire crack extension is shown in Fig. 24a, and high-magnification micrographs of select locations of the fracture surface, designated A-D in Fig. 24a, are shown in Figs. 24b-e. A measurement bar is also included in Fig. 24a to help define the approximate position of the crack front after the various test periods. The micrographs of locations A-C in Figs. 24b-d are from the CGR test region, and location D in Fig. 24e is from the J-R curve test. For the CGR test, the fracture morphology is TG initially and changes to IG beyond  $\approx 0.27$  mm (Fig. 24a). These results show good agreement with the measured CGRs; an environmental enhancement of growth rates occurred after  $\approx 0.26$ -mm crack extension.



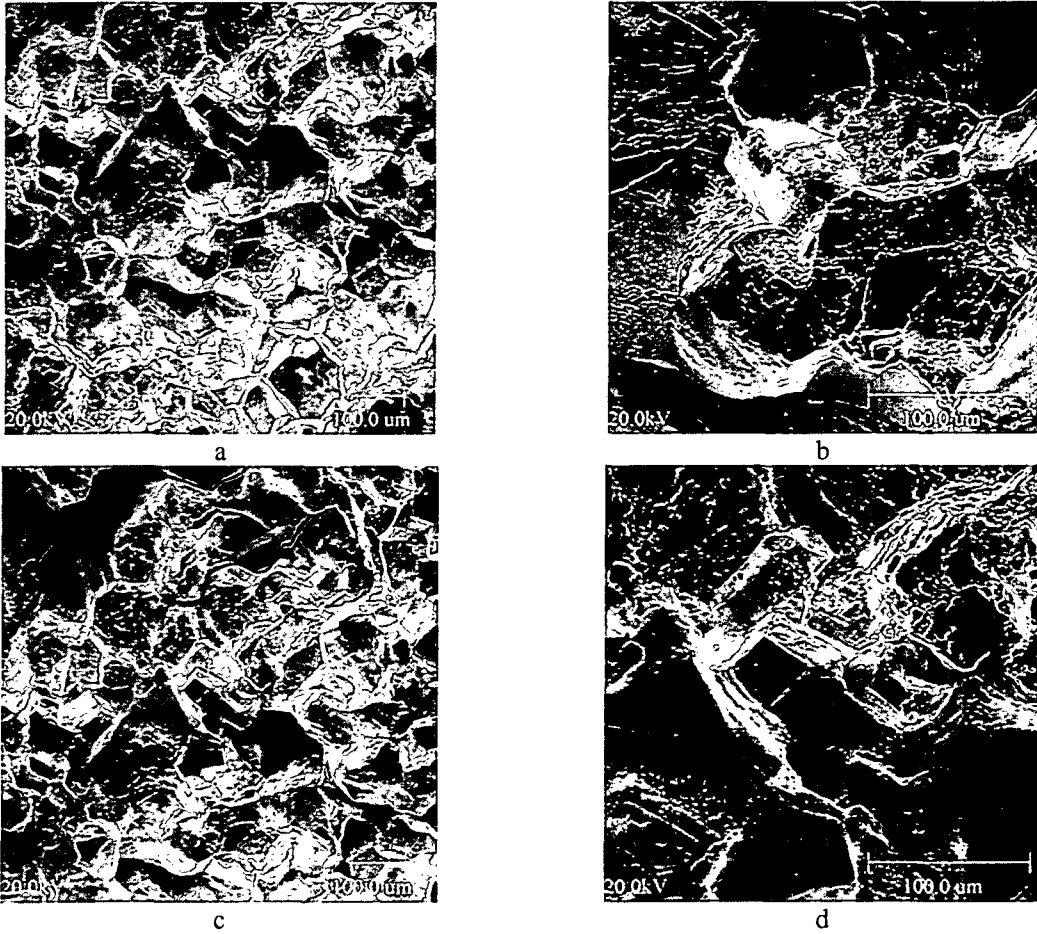


Figure 21. Micrographs showing the fracture surface of Specimen 85-1A-TT at positions A and B in Fig. 19. Figures b and d are high magnification of a and c.

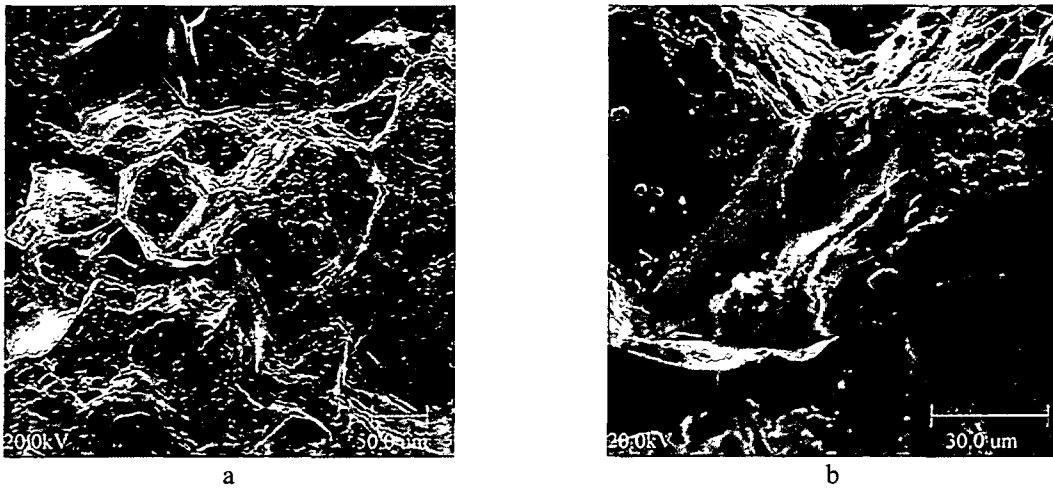


Figure 22. Micrographs showing the fracture surface of Specimen 85-1A-TT at position C in Fig. 19. Figure b is high magnification of a.

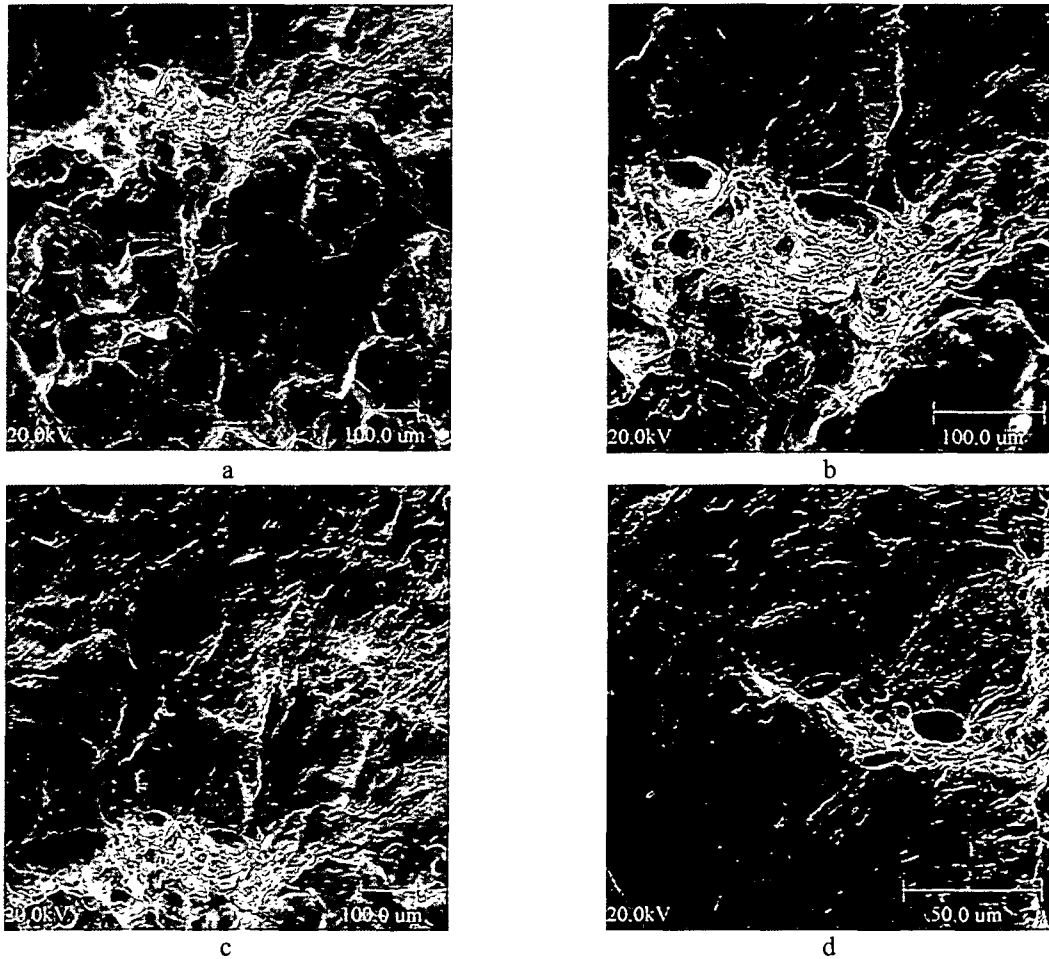


Figure 23. Micrographs showing the fracture surface of Specimen 85-1A-TT at positions D and E in Fig. 19. Figures b and d are high magnification of a and c.

The experimental results from the J-R curve test were analyzed in accordance with ASTM E-1737 to obtain the fracture toughness J-R curve for Specimen 85-1A-TT in BWR water. The displacement of load pins was determined by subtracting the extension of the load train from the measured extension. The load train extension was determined as a function of applied load using a very stiff specimen. The blunting line was defined by the relationship  $\Delta a = J/(4\sigma_f)$ , where  $\sigma_f$  is the effective flow stress.

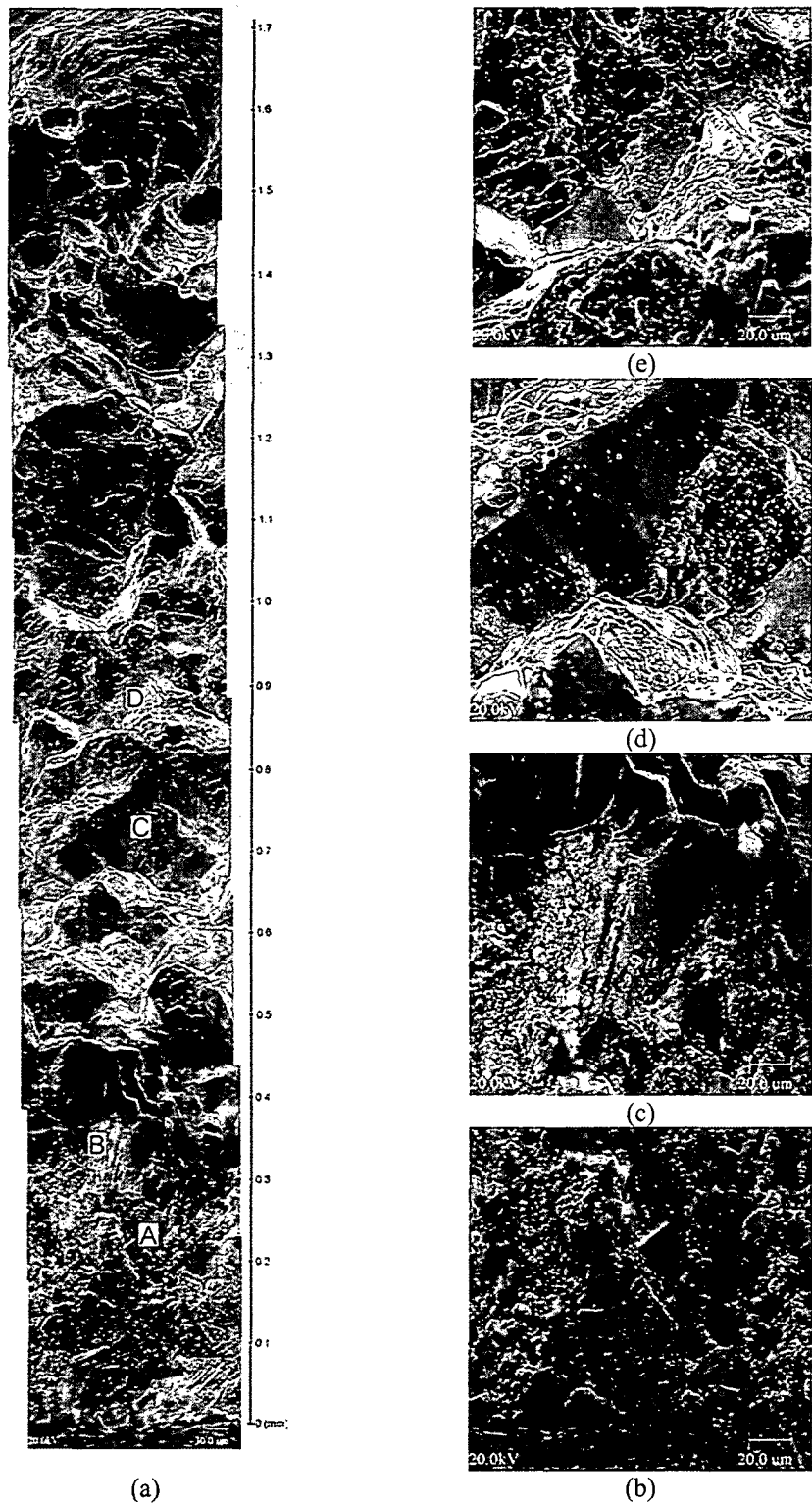


Figure 24. Photomicrographs showing (a) a slice of the entire length of the fracture surface and high-magnification photomicrographs of the fracture surface at positions (a) A, (b) B, (c) C, and (d) D.

The curves for load-vs.-load-line displacement and the fracture toughness of Specimen 85-1A-TT are shown in Figs. 25 and 26, respectively. The results yield a  $J_{IC}$  value of  $\approx 345 \text{ kJ/m}^2$  ( $1970 \text{ in-lb/in}^2$ ) for the material. This value is lower than those observed earlier<sup>112</sup> for other heats of austenitic SS in air; the  $J_{IC}$  values were 368 and  $378 \text{ kJ/m}^2$  ( $2101$  and  $2158 \text{ in-lb/in}^2$ ), respectively, for Type 304 and Type 316L SS irradiated to  $0.9 \times 10^{21} \text{ n/cm}^2$ .

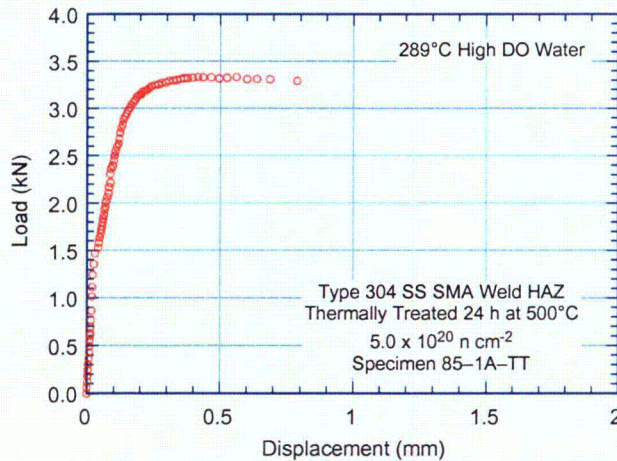


Figure 25.  
Load vs. load-line displacement curve for irradiated SMA weld HAZ Specimen 85-1A-TT in high-purity water at 289°C.

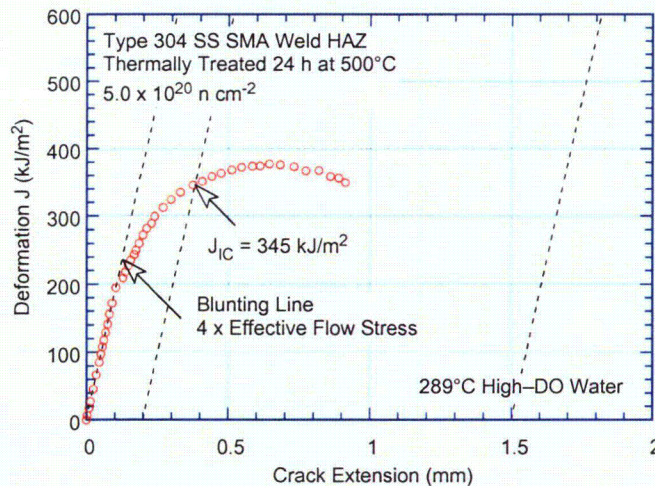


Figure 26.  
Fracture toughness J-R curve for irradiated SMA weld HAZ Specimen 85-1A-TT in high-purity water at 289°C.

### 3.2.3.4 Specimen 85-7A of Type 304 SS HAZ, Test CGRI-20

The test conditions, experimental CGRs, the allowed  $K_{max}$  from K/size criterion, and the margin between the applied and allowed values of  $K_{max}$  are given in Table 7 for Specimen 85-7A. The test was started in high-purity water with  $\approx 500$  ppb DO and flow rate of  $\approx 10.0 \text{ mL/min}$ . The ECP of a Pt electrode and a SS sample located at the exit of the autoclave was monitored continuously during the test, while the water DO and conductivity were determined periodically. Precracking was carried out at  $R = 0.2$ ,  $K_{max} = 15.5 \text{ MPa m}^{1/2}$  ( $14.1 \text{ ksi in}^{1/2}$ ), and triangular waveform with 1-Hz frequency. After  $\approx 0.1 \text{ mm}$  (3.9 mil) crack growth the load ratio was increased to 0.5, and the rise time increased to 60–1000 s to begin the transition from TG fatigue crack growth to IG SCC growth. The changes in crack length and  $K_{max}$  with time during various test periods are shown in Fig. 27. For this specimen, significant environmental enhancement of growth rates occurred during test period 5 (Fig. 27b).

Table 7. Crack growth data for Specimen 85-7A of SS SMA weld HAZ in high-purity water<sup>a</sup> at 289°C.

Test Period <sup>b</sup>	Test Time, h	ECP, <sup>c</sup> mV (SHE)		O <sub>2</sub> Conc., <sup>c</sup> ppb	R Load Ratio	Rise Time, s	Down Time, s	Hold Time, s	K <sub>max</sub> , MPa·m <sup>1/2</sup>	ΔK, MPa·m <sup>1/2</sup>	Growth Rate, m/s	Allowed K <sub>max</sub> , MPa·m <sup>1/2</sup>	Margin in K <sub>max</sub> , <sup>d</sup> %
Pre	166	261	224	500	0.23	0.5	0.5	0	16.7	12.9	2.77E-08	29.7	-44
1	187	258	225	500	0.50	60	4	0	16.6	8.3	negligible	29.7	-44
2	428	244	219	500	0.51	300	4	0	16.5	8.1	2.09E-11	29.6	-44
3	499	245	221	500	0.50	1000	12	0	17.2	8.6	negligible	29.6	-42
4	608	234	211	500	0.53	1000	12	0	18.1	8.5	4.65e-11	29.6	-39
5*	763	229	209	500	0.50	1000	12	0	19.3	9.6	4.28e-10	29.1	-34
6*	788	231	212	500	0.50	1000	12	3600	19.7	9.8	9.51e-10	28.8	-32
7	845	221	214	500	1.00	-	-	-	20.5	0.0	9.46e-10	28.3	-28
8	1100	-527	-252	<50	1.00	-	-	-	21.0	0.0	1.55E-11	28.0	-25

<sup>a</sup>Laboratory-prepared SMA weld HAZ, irradiated to  $0.5 \times 10^{21}$  n/cm<sup>2</sup>.

<sup>b</sup>An asterisk indicates environmental enhancement of growth rates under cyclic loading.

<sup>c</sup>Represents values in the effluent. Conductivity was  $\approx 0.07$  and  $0.3 \mu\text{S}/\text{cm}$  in feedwater and effluent, respectively.

<sup>d</sup>Based on flow stress.

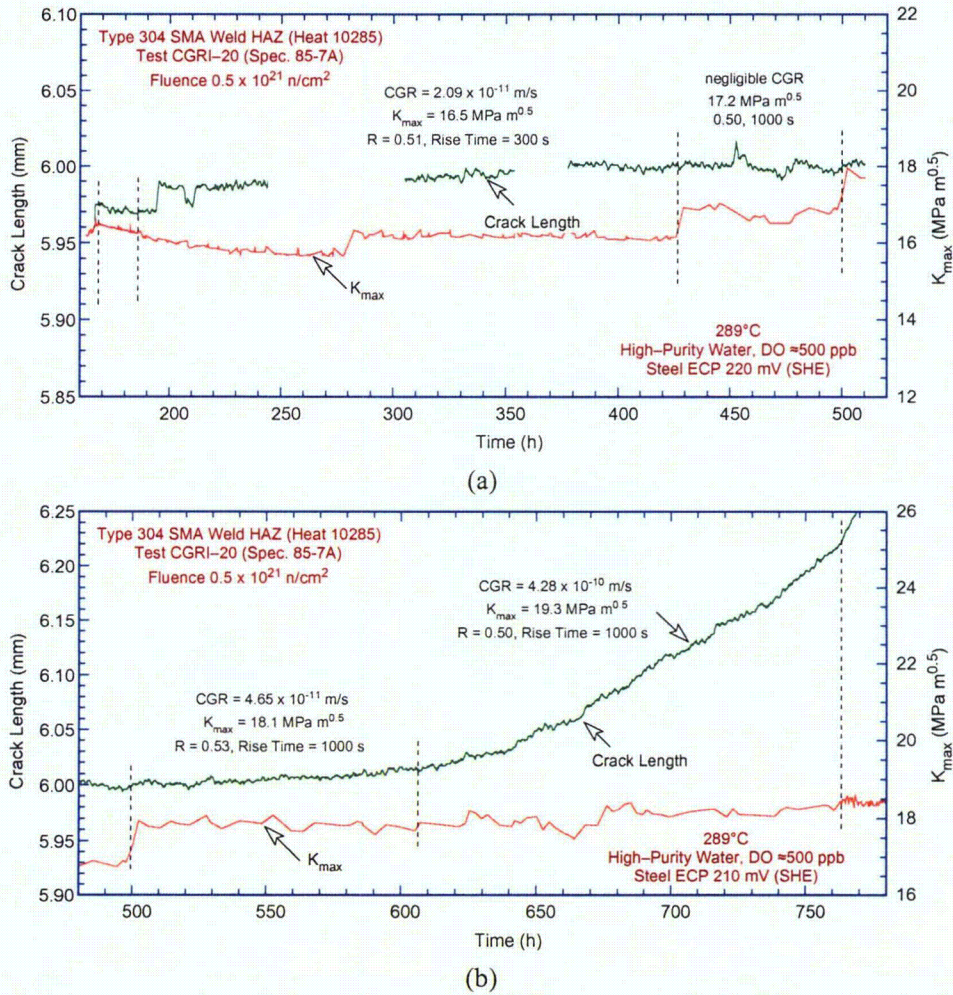


Figure 27. Crack-length-vs.-time plots for irradiated SMA weld HAZ Specimen 85-7A in high-purity water at 289°C during test periods (a) 1-3, (b) 4-5, and (c) 6-8.

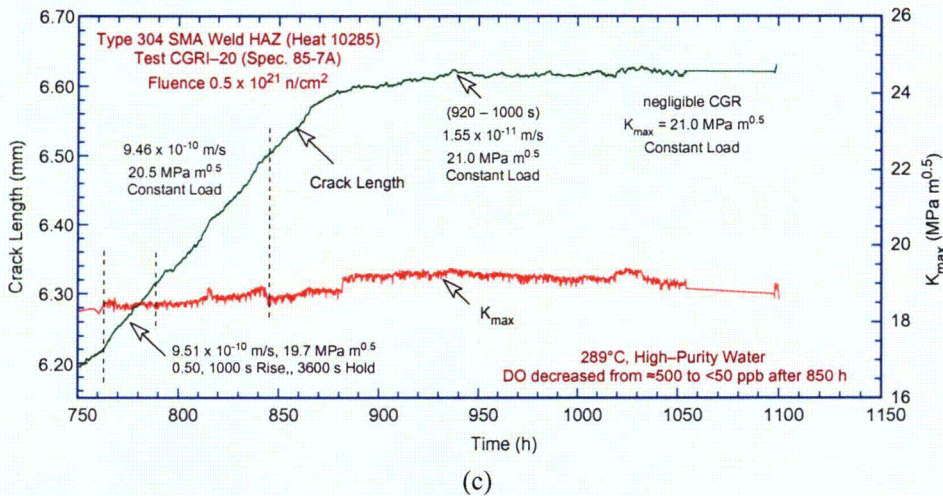


Figure 27. (Contd.)

After the CGR test, the final crack front was marked by fatigue cycling at room temperature in air. The specimen was then fractured, and the fracture surfaces of both halves of the specimen were photographed with a telephoto lens through the cell window (Fig. 28). The actual crack extension was  $\approx 80\%$  greater than the value determined from the DC potential measurements. Crack extensions estimated from the DC potential drop method were scaled proportionately; the corrected values of  $K_{\max}$  and growth rates are listed in Table 7. For this specimen, loading conditions for the entire test satisfy the  $K/\text{size}$  criterion.

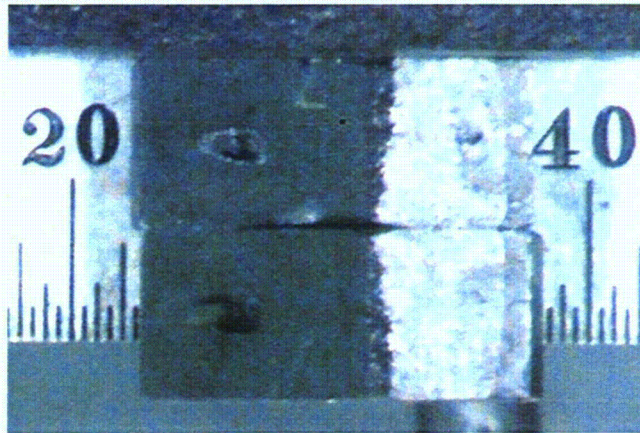


Figure 28. Photomicrograph of the fracture surface of Specimen 85-7A.

### 3.2.4 CGRs of Austenitic SS Weld HAZ under Continuous Cycling

For continuous cyclic loading, the experimental CGRs for irradiated SS weld HAZ specimens in high-DO environment and those predicted in air for the same loading conditions are plotted in Fig. 29. Results from tests performed earlier on nonirradiated material are also included in the figures.<sup>102</sup> The curve represents the Shack/Kassner model for nonirradiated austenitic SSs in high-purity water with 8 ppm DO (Eq. 26) and is included to provide a comparison with the irradiated CGR data. The CGRs in air,  $\dot{a}_{\text{air}}$  (m/s), were determined from the correlations developed by James and Jones<sup>109</sup> (Eqs. 22–24). In

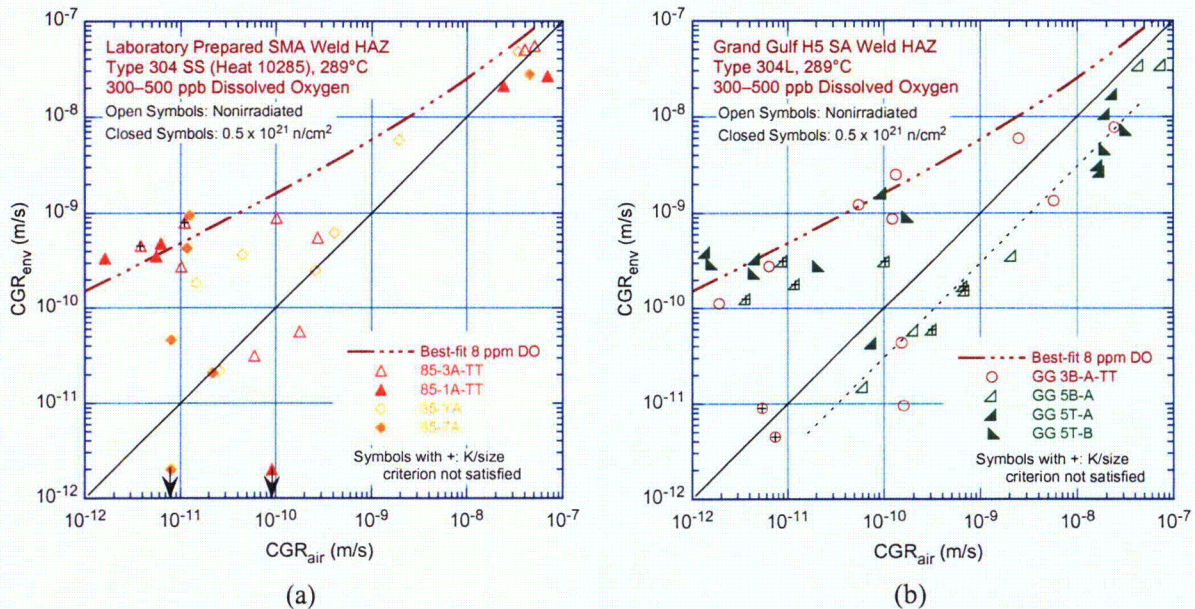


Figure 29. CGR for irradiated and nonirradiated specimens of (a) laboratory-prepared Type 304 SS SMA weld HAZ and (b) Type 304L SA weld HAZ from the Grand Gulf core shroud under continuous cycling in high-purity water at 289°C.

Fig. 29, the loading conditions for the data points shown with a “+” did not satisfy the  $K_{\max}$  criterion of ASTM E-647.

In these figures, the data points that lie along the diagonal represent predominantly mechanical fatigue, and those that lie close to the Shack/Kassner model indicate environmentally enhanced crack growth. For both irradiated and nonirradiated specimens, enhancement of CGR did not occur readily when the load ratio and rise time were increased. For example, a large number of data points lie along the diagonal in Fig. 29, particularly for the GG Type 304L weld HAZ. The applied  $K_{\max}$  had to be increased for enhanced growth rates.

The results indicate that under mechanical fatigue loading (i.e., no environmental enhancement), the CGRs for the GG Type 304L SA weld HAZ are lower than those for the Type 304 SMA weld HAZ, e.g., the CGRs for laboratory-prepared weld HAZ (Fig. 29a) show good agreement with those predicted by Eqs. 22–24, while those for the GG weld HAZ are a factor of  $\approx 3$  lower (dashed line in Fig. 29b). Also, under this type of loading, thermal treatment of the material for 24 h at 500°C or irradiation to  $5.0 \times 10^{20}$  n/cm<sup>2</sup> ( $E > 1$  MeV) ( $\approx 0.75$  dpa) has little or no effect on growth rates.

In the high-DO NWC BWR environment (under environmentally enhanced condition), the CGRs of the laboratory-prepared Type 304 SS SMA weld HAZ (Fig. 29a) and those of the GG Type 304L SA weld HAZ (Fig. 29b) are comparable. Also, thermal treatment of the material for 24 h at 500°C has little or no effect on growth rates. The results for nonirradiated GG weld HAZ are in good agreement with the data obtained by Andresen et al.<sup>105</sup> for GG Type 304L weld HAZ in high-DO water (2000 ppb DO) at 288°C. For example, Andresen obtained a CGR of  $3.4 \times 10^{-10}$  m/s at  $R = 0.7$ ,  $K_{\max} = 27.4$  MPa m<sup>1/2</sup>, and triangular waveform with 500-s rise time.

For both the GG and laboratory-prepared weld HAZs, irradiation to  $\approx 0.75$  dpa appears to increase the CGRs marginally. In high-DO NWC BWR water, the CGRs for irradiated and nonirradiated thermally-treated HAZ and irradiated as-welded HAZ may be represented by the Shack/Kassner model for nonirradiated austenitic SSs in high-purity water with 8 ppm DO.

Metallographic examination of the fractured specimens indicates that under environmentally enhanced growth conditions (i.e., the data points that lie close to the Shack/Kassner model), an IG fracture morphology is observed for both the irradiated and nonirradiated laboratory-prepared Type 304 SS weld HAZ (Fig. 19). Transgranular fracture morphology is observed under conditions that show little or no environmental enhancement (i.e., data points that lie close to the diagonal in Fig. 29a) and is predominantly due to mechanical fatigue. Although metallographic examination of the irradiated GG Type 304L HAZ has not been completed, the results obtained earlier for the nonirradiated material indicate that the fracture morphology of GG Type 304L HAZ is different from that for Type 304 SMA weld HAZ. For example, in the GG Type 304L HAZ, a TG fracture morphology with a well-defined river pattern is observed under all loading conditions, even where growth is environmentally enhanced. Intergranular fracture morphologies are usually observed in cold-worked SSs, whether initially annealed or sensitized.<sup>103,105,106</sup> Because of the residual strain associated with the welding process, the observed TG fracture morphology is not expected in SS weld HAZ, especially for a case in which the environment enhancement is substantial. The reasons for this unexpected behavior are unclear.

### 3.2.6 CGRs of Austenitic SS Weld HAZ under Constant Load or Cycling with Long Hold Periods

For CGR tests under constant load or a trapezoidal waveform with long hold periods (i.e., constant load with periodic partial unloading), the experimental CGRs for irradiated SS weld HAZ specimens in high- and low-DO BWR environments are shown in Fig. 30b and those for nonirradiated SS weld HAZ specimens in Fig. 30a. Because of relatively low flow stress of the nonirradiated materials, the applied  $K_{\max}$  for most of the test periods did not satisfy the  $K/\text{size}$  criterion of ASTM E-1681; these data points are shown with a "+" in Fig. 30a. In addition, for the Type 304 SS SMA weld HAZ specimen (data shown as triangles in Fig. 30a), the fracture plane was not normal to the stress axis but at an angle of  $45^\circ$  to the stress axis.

For nonirradiated GG Type 304L weld HAZ, although some of the data did not meet the  $K/\text{size}$  criterion of ASTM E-1681, the as-welded (right angle triangles in Fig. 30a) and as-welded plus thermally-treated (circles in Fig. 30a) materials have comparable CGRs. For both conditions, the CGRs are a factor of  $\approx 2$  lower than the NUREG-0313 curve for sensitized SSs in water with 8 ppm DO. These results are in good agreement with the CGR of  $1 \times 10^{-10}$  m/s obtained by Andresen et al.<sup>105</sup> for the GG Type 304L weld HAZ in high-DO water (2000 ppb DO) at  $288^\circ\text{C}$  and  $K_{\max} = 27.4 \text{ MPa m}^{1/2}$ . As discussed above, the CGRs for nonirradiated thermally-treated Type 304 SS weld HAZ (open triangle in Fig. 30a) should be discounted; for this material, the loading conditions did not meet the  $K/\text{size}$  criterion and fracture plane was at  $45^\circ$  to the stress axis.

The fracture morphology of the two materials is also different, e.g., TG for the Type 304L SA weld HAZ and IG for the Type 304 SMA weld HAZ. As discussed in the last section, a TG morphology is unusual in SS weld HAZ, e.g., the presence of residual strain in the material typically promotes IG crack growth even in nonsensitized SS.<sup>103,105,106</sup> An IG fracture occurred in all cold-worked SSs. Additional tests will be conducted on the nonirradiated GG Type 304L weld HAZ to establish its fracture behavior.



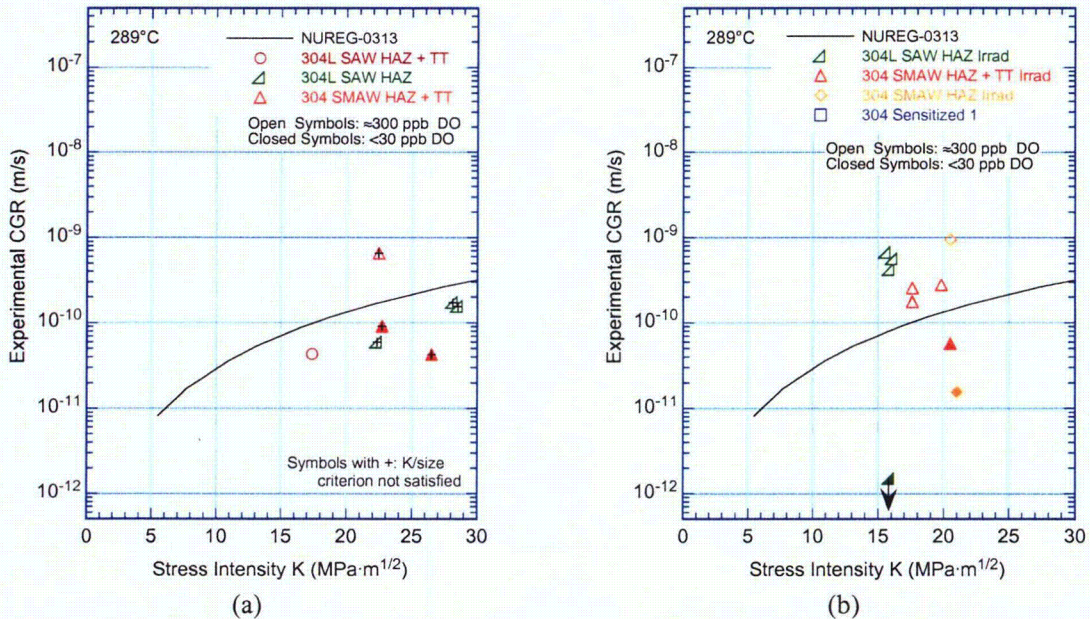


Figure 30. CGR under constant load with periodic partial unloads for (a) nonirradiated and (b) irradiated SS weld HAZ specimens in high-purity water at 289°C.

Irradiation to  $5.0 \times 10^{20} \text{ n/cm}^2$  ( $\approx 0.75 \text{ dpa}$ ) increased the growth rates of all SS weld HAZ materials. The CGRs of irradiated HAZ specimens are a factor of 2–5 higher than those predicted by the NUREG-0313 disposition curve for sensitized SSs in high-DO water. The fracture morphology for irradiated Type 304 weld HAZ is similar to the nonirradiated material, e.g., fracture morphology is IG under environmentally enhanced or SCC conditions, and TG under mechanical fatigue or conditions that show little or no environmental enhancement.

A beneficial effect of reducing the corrosion potential of the environment was observed for all materials that were tested in the BWR environment. The growth rates of irradiated or nonirradiated Type 304 weld HAZ decreased by a factor of  $\approx 8$ , and those for irradiated Type 304L weld HAZ decreased by nearly two orders of magnitude, when the DO was decreased from  $\approx 300 \text{ ppb}$  to  $<30 \text{ ppb}$ .

### 3.2.7 Fracture Toughness of Irradiated Austenitic SS Weld HAZ in High-Purity Water at 288°C

The fracture toughness J-R curve was determined for irradiated Type 304 SS SMA weld HAZ (Specimen 85-1A-TT) in high-DO water at 288°C. The experimental  $J_{Ic}$  for this material and those obtained earlier<sup>112</sup> for two commercial heats (C19 and C16) in air are plotted as a function of neutron exposure in Fig. 31. Results of tests on Type 304 SS reactor internal materials from operating BWRs<sup>86</sup> are also included in the figure. The fracture toughness  $J_{Ic}$  in high-DO water is slightly lower than that in air. Also, a significant result for the J-R curve test in high-DO water is the essentially IG fracture morphology (Figs. 21 and 22) as opposed to the ductile fracture morphology expected in a test in air.

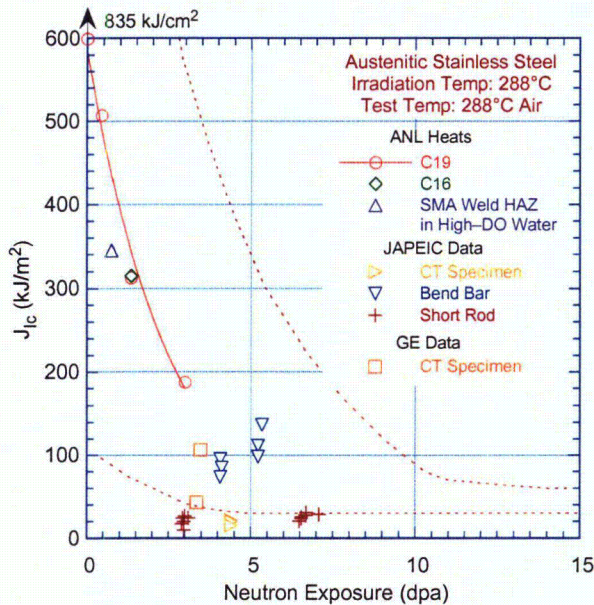


Figure 31. Fracture toughness  $J_{1c}$  as a function of neutron exposure at 288°C for austenitic SSs in air and SS SMA weld HAZ in high-purity water. Dashed lines represent upper and lower bounds for change in  $J_{1c}$  for austenitic SSs irradiated at 350–450°C. JAPEIC = Japan Power Engineering and Inspection Corporation, GE = General Electric Nuclear Energy.

### 3.2.8 Metallographic Examination of the Fracture Surface of CGR Test Specimen C3–C

Crack growth tests on Type 304L Heat C3 and Type 316L SS Heat C16 irradiated to fluence levels of 0.45, 1.35, and 3.0 dpa indicate significant enhancement of CGRs for irradiated steels in the NWC BWR environment.<sup>100</sup> The CGRs of Heat C3 irradiated to 1.35 and 3.0 dpa and of Heat C16 irradiated to 3.0 dpa are comparable and a factor of  $\approx 5$  higher than the disposition curve proposed in NUREG-0313<sup>101</sup> for sensitized austenitic SSs (Fig. 32). Also, in the HWC BWR environment, the CGRs decreased by an order of magnitude for Heat C3 irradiated to 1.35 dpa (open and closed circles in Fig. 32) and Heat C16 irradiated to 3.0 dpa (open and closed right-angle triangles). However, the benefit of HWC was not observed in a test on Heat C3 (Specimen C3–C) irradiated to 3.0 dpa (open and closed triangles).<sup>100</sup> A detailed metallographic examination of the fracture surface of Specimen C3–C was performed to determine whether the lack of beneficial effect of HWC observed for this specimen was associated with the possible loss of constraint in the specimen due to high applied load.

For this test, the environmental and loading conditions, experimental CGRs, allowed  $K_{max}$  from  $K/size$  criterion, and the deviation of applied  $K_{max}$  from the allowed value are given in Table 8. The results indicate that the applied  $K_{max}$  meets the  $K/size$  criterion for test periods 1–5 and is  $\approx 23$  and 53% higher than the allowed value for periods 6 and 7, respectively. Figure 33 shows the change in crack length and  $K_{max}$  with time during periods 6 ( $\approx 200$ –311 h) and 7 ( $\approx 400$ –540 h). The crack length vs. time plot shows little or no change in CGR during these two test periods when the DO level was decreased from  $\approx 400$  to 20 ppb. For this specimen, either there is no benefit of a low-DO environment on CGRs or, if there is a benefit, it seems to have been completely balanced by the increase in CGR because of the loss of specimen constraint due to high applied  $K_{max}$ .

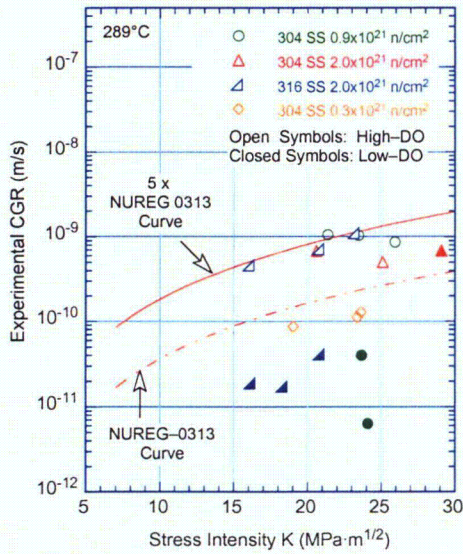


Figure 32. Crack growth rate under constant load for irradiated austenitic SSs in high-purity water at 289°C.

Table 8. Crack growth results for Specimen C3-C of Type 304 SS<sup>a</sup> in high-purity water at 289°C.

Test Period	Test Time, h	ECP, mV (SHE) <sup>b</sup>		O <sub>2</sub> Conc., <sup>b</sup> ppb	Load Ratio	Rise Time, <sup>c</sup> s	Hold Time, s	K <sub>max</sub> , MPa·m <sup>1/2</sup>	ΔK, MPa·m <sup>1/2</sup>	Growth Rate, m/s	Allowed K <sub>max</sub> , MPa·m <sup>1/2</sup>	Deviation in K <sub>max</sub> , %	Crack Length, <sup>d</sup> mm
1	46	241	164	300	0.26	2	0	19.0	14.0	2.00E-08	22.4	-15	6.702
2	71	223	155	300	0.53	30	0	19.5	9.2	2.22E-09	22.1	-12	6.830
3	99	235	167	300	0.70	300	0	20.0	6.0	1.73E-09	21.8	-9	6.977
4	142	232	164	300	0.69	1000	0	20.4	6.3	1.25E-09	21.4	-5	7.167
5	191	233	164	300	0.70	2	3600	20.6	0.0	6.83E-10	21.1	-2	7.294
6	311	-450	7	100	0.70	2	3600	25.1	0.0	5.07E-10	20.5	23	7.572
7	560	-547	-294	10	0.70	2	3600	29.1	0.0	6.91E-10	19.1	53	8.171
8	706	-551	-502	10	0.70	2	3600	36.4	0.0	2.04E-09	16.4	122	9.154
9	724	-557	-457	10	0.70	2	3600	38.6	0.0	3.70E-09	15.8	144	9.367

<sup>a</sup>Heat C3, irradiated to  $2.0 \times 10^{21}$  n/cm<sup>2</sup>.

<sup>b</sup>Represents values in the effluent. Conductivity was 0.07 and 0.3 μS/cm in feedwater and effluent, respectively. Feedwater pH at room temperature was 6.5.

<sup>c</sup>In all cases, return time was 2 s.

<sup>d</sup>Initial and final crack length of 6.000 and 10.047 mm, respectively.

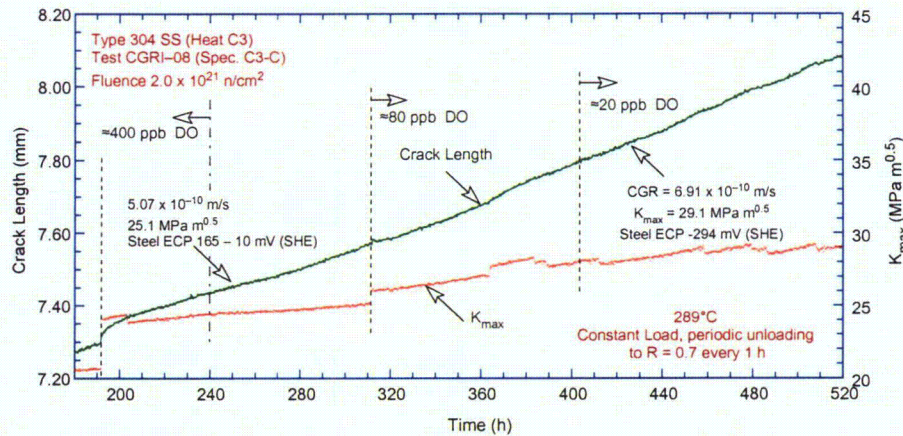


Figure 33. Plots of crack length and  $K_{max}$  vs. time for Specimen C3-C in high-purity water at 289°C during test periods 6 and 7.

Stress corrosion cracking of materials in LWR environments involves two steps: rupture of the surface oxide film to expose the underlying matrix and environmental attack of the exposed matrix by dissolution or other processes. The rupture of the surface film is controlled by mechanical factors, and environmental attack is controlled by material and environmental factors. Figure 32 shows that the CGRs of irradiated SSs typically decrease by more than an order of magnitude when the DO level is decreased from  $\approx 300$  to 20 ppb. To completely balance the decrease in growth rates from a change in environment, the increase in CGR due to loss of specimen constraint must be at least a factor of 10. A loss of specimen constraint that results in such a large increase in growth rate would also influence the fracture mode. For example, if the thickness criterion is exceeded, the crack plane will be out-of-normal near the edges of the specimen, and if the specimen ligament criterion is exceeded the crack would grow away from the normal plane.

The fracture morphology of the specimen was examined to investigate the effect of low DO on growth rates. To reduce the exposure to the SEM operator, the fracture surface was initially cut away from the fractured CT specimen using a Charmilles-Andrew Model EF330 traveling-wire electro-discharge machine (EDM). However, because activity of the thin slice of the fracture surface was still  $>20$  R/h on contact, exceeding the maximum allowable activity of 10 R/h inside the SEM, several thin (1-mm wide) slices of the fracture surface along the entire crack advance were cut from the fracture surface. Two such slices were examined in the SEM. Although precautions were taken to ensure that the specimen was square to the movement of the EDM wire, the cuts were not always straight.

Measurements of total crack extension from micrographs of the fracture surface of the two slices yielded an average value of  $\approx 4.3$  mm; this is slightly larger than the 4.06 mm obtained from the photograph, taken with a telephoto lens through the hot cell window, of the fracture surfaces of the two halves of the specimen. The difference in the two measurements is most likely due to slight variation in crack extension across the width of the specimen.

Figure 34 shows a side view of the first slice cut from Specimen C3-C. The fracture surface is towards the top, in a plane perpendicular to the picture. The fracture plane is relatively straight and normal to the stress axis for the initial  $\approx 3.5$ -mm crack extension and deviated from the normal plane for longer crack extensions. A secondary crack propagates at an angle of  $\approx 45^\circ$  to the original fracture plane. The DO level in the environment decreased from  $\approx 400$  to 20 ppb at  $\approx 1.7$ -mm crack extension, i.e., in the middle of this relatively straight crack extension that is  $\approx 3.5$  mm.

These results do not indicate any obvious loss of constraint in the specimen due to high applied load. For specimen C3-C, the water chemistry was changed from NWC to HWC (by decreasing the DO level from  $\approx 400$  to 20 ppb) at  $\approx 1.7$ -mm crack extension, i.e., in the middle of the relatively straight crack

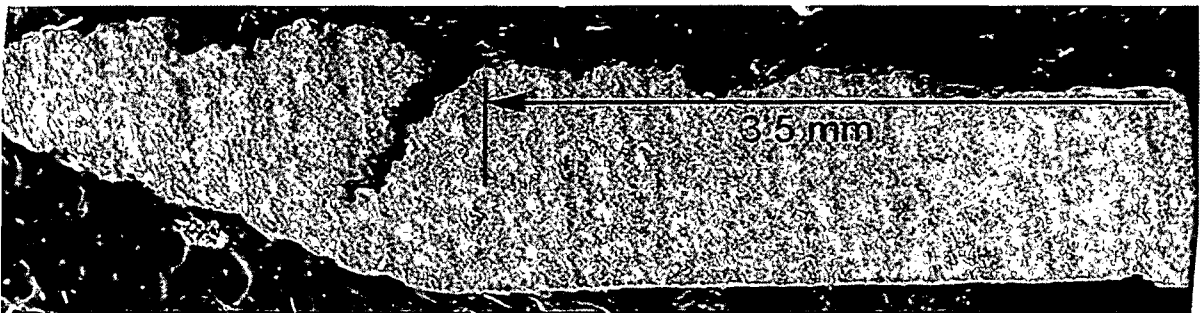


Figure 34. Side view of the first slice cut from Specimen C3-C.

extension that is  $\approx 3.5$  mm. Most likely, the specimen ligament criterion was exceeded beyond the 3.5 mm crack extension, i.e., during Test Period 9.

A collage of images taken from the entire crack extension for the first slice is shown in Fig. 35a, and high-magnification photomicrographs of the surface at locations 2 and 1 are shown in Figs. 35b and c, respectively. After the initial  $\approx 0.6$ -mm-long TG crack, the fracture morphology for the specimen is completely IG for the remainder of the test. The transition from a TG to IG fracture appears to have occurred at  $\approx 80$  h, i.e., during test period 2. Locations 1 and 2 represent regions near the end of TG fracture and start of IG fracture, respectively.

A composite photograph of the fracture surface of the second slice from Specimen C3-C is shown in Fig. 36a, and high-magnification photomicrographs of the fracture surface at locations D, C, B, and A are shown in Figs. b, c, d, and e, respectively. These locations represent the fracture morphology during test periods 2, 3, 6, and 7, respectively. Once again, after the initial TG fracture during test period 1, the fracture morphology during all other test periods is completely IG. No fractographic indication of a change in fracture mode due to a loss in constraint is evident at the  $\approx 1.6$ -mm crack advance. The fracture surface edge is also visible in Fig. 36a. The fracture plane appears to be absolutely straight and normal to the stress axis. Also, although the fracture surface is covered with oxides that seem to have been deposited from the solution, the fracture morphology for test periods 6 and 7, i.e., Figs. 36b and c, is the same.

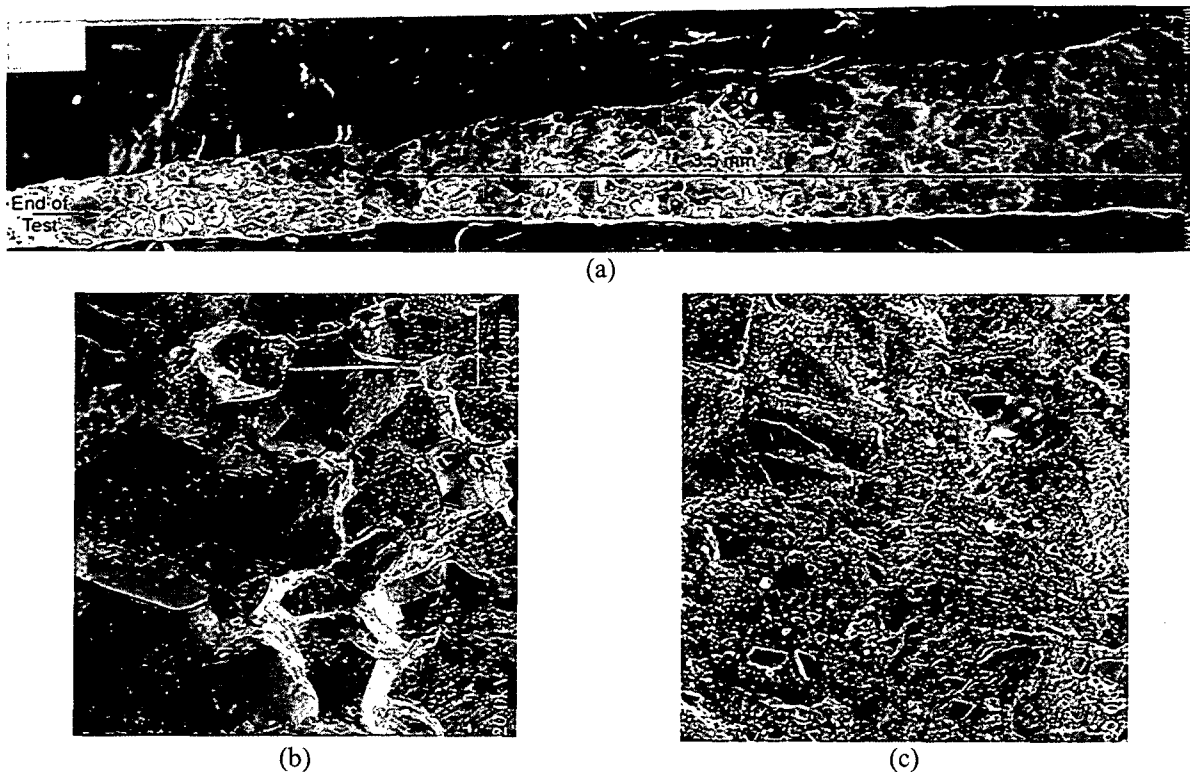


Figure 35. (a) A photograph of the entire crack extension for the first slice of Specimen C3-C and (b) and (c) high-magnification micrographs of the surface at locations 2 and 1, respectively.

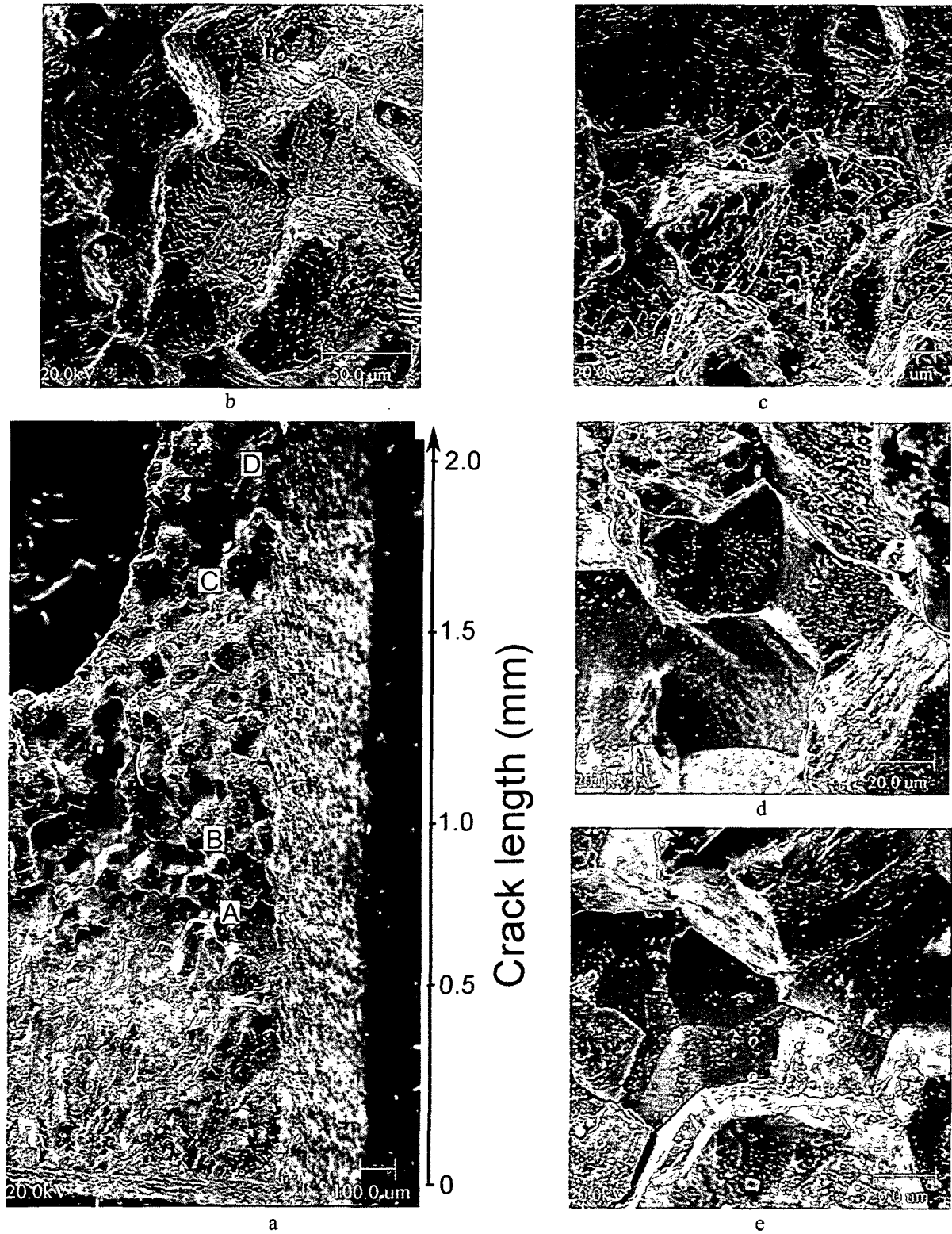


Figure 36. (a) Photograph of the fracture surface of the second slice of Specimen C3-C and high-magnification micrographs of the surface at locations (b) D, (c) C, (d) B, and (e) A.

These results suggest that although the proposed specimen size criterion of Eq. 28 was not met at the time when the DO level was decreased from  $\approx 400$  to 20 ppb, i.e., at  $\approx 1.6$ -mm crack extension between test periods 6 and 7, there is no fractographic indication of a loss in constraint in the specimen. However, the specimen constraint may have been lost at the start of test period 9, i.e., after the  $\approx 3.5$  mm crack extension. The CGR data on Specimen C3-C suggest that a low-DO environment may not be a benefit for Heat C3 irradiated to  $\approx 3.0$  dpa, at least at K values above  $25 \text{ MPa m}^{1/2}$ . Additional data on Types 304 and 316 SS irradiated to 3-5 dpa are needed to better establish the effect of decreased DO level on the CGRs of irradiated austenitic SSs.





## **4 Causes and Mechanisms of Irradiation-Assisted Cracking of Austenitic Stainless Steel in PWRs**

---

### **4.1 Introduction**

Field failures have been reported in various PWR core internal components fabricated from austenitic SSs, such as baffle bolts, control rod cladding, pins, keys, and bolts. Many of the failed components were fabricated from cold-worked materials of Types 316, 347, and 304 SS. Typically, failures of PWR core internals are IG and are observed at neutron-damage levels more than an order of magnitude higher (i.e., >10 dpa) than the threshold damage level of BWR core internals (i.e., ≈0.7 dpa). At this time, the database and mechanistic understanding of PWR core internals are very limited, and it is not clear if the failures should be classified as IASCC or IAC.

The objectives in this task are to evaluate the susceptibility of austenitic SS core internals to IAC in PWRs as a function of the fluence, water chemistry, material chemistry, and cold-work. The program will focus on: (a) evaluation of the effects of PWR-like high fluence on susceptibility to IASCC, (b) neutron irradiation embrittlement, e.g., loss of fracture toughness, (c) void swelling behavior in austenitic SSs, (d) effect of cold-work and solution anneal, (e) fracture toughness and SCC behavior of cast duplex SSs at high fluence, and (f) effectiveness of mitigative measures, such as optimization of ferrite content, grain-boundary engineering, and minimization of S concentration. Tests will be conducted on SS specimens irradiated in the BOR-60 reactor in Russia.

### **4.2 Irradiation of Austenitic Stainless Steels in the BOR-60 Reactor (H. M. Chung and W. K. Soppet)**

An experiment has been initiated to irradiate specimens of various types of materials and geometry under PWR-like conditions. The irradiation experiment is being conducted in cooperation with the CIR Program. Irradiation of the specimens is being performed in the BOR-60 Reactor, a sodium-cooled breeder reactor located in the Research Institute of Atomic Reactors (RIARs), Dimitrovgrad, Ulyansk Region, Russian Federation.

Irradiation of tensile and TEM disk specimens to ≈5, 10, and ≈20 dpa in Irradiation Cycle BORIS-6 has been completed in flowing sodium maintained at 322.1–322.6°C (611.8–612.7°F). After irradiation, 48 tensile specimens (contained in 12 bundles) and 166 disk specimens (contained in four capsules) were discharged. After the specimens were cleaned of sodium at the Westinghouse Electric Co. in Pittsburgh they were shipped to ANL in a 55-gal drum (WRD-871). The irradiated specimens were successfully unloaded from the drum and transferred to the Irradiated Materials Laboratory hot cell for testing. Further irradiation of specimens to ≈40 dpa in Irradiation Cycle BORIS-7 continues in the second part of the campaign. Eight more bundles containing 32 tensile specimens are being irradiated.

Tests performed on the materials irradiated in the Halden BWR reactor have also been used to gain some insight into potential mechanisms for IASCC that are also relevant to PWRs. After exposure to the conditions of the SSRT test in BWR water, susceptibility to IG cracking in an inert environment has been determined by rapid bending in air at 23°C (73°F). Similar tests were also performed on hydrogen-charged specimens in vacuum. Both types of bend fracture exhibited similar characteristics, suggesting that in both cases hydrogen-induced IG failure occurred. However, steels that showed high susceptibility to IGSCC in 289°C (552°F) water exhibited low susceptibility to IG cracking in the tests at 23°C air or vacuum, and vice versa. These results indicate that although IG cracking in 23°C air is dominated by H-induced embrittlement of ordinary grain boundaries, other processes control IASCC in 289°C water.

On the basis of these investigations, and studies on binary Ni-S and crack-tip microstructural characteristics of LWR core internal components reported in the literature, an initial IASCC model based on a crack-tip grain-boundary process that involves S has been proposed. In this model, several factors play key roles: grain-boundary segregation of Ni and S, formation of grain-boundary oxide in front of the crack tip, formation of Ni- and S-rich thin films, formation of islands between the oxide and metal matrix, and disorder-induced melting or amorphization of the Ni-S thin films and islands at sufficiently high concentration of S. These results were presented earlier.<sup>113</sup>

### 4.3 Assessment of Void Swelling in Austenitic Stainless Steel Core Internals (H. M. Chung)

As many PWRs age and life extension of the aged plants is considered, void swelling behavior of austenitic SS core internals has become the subject of increasing attention. Excessive void swelling can lead to dimensional instability of the component and significant degradation of fracture toughness. It could also influence or contribute to the susceptibility of the component to IASCC, stress relaxation, or irradiation embrittlement.

Because of experimental problems largely related to the salvaging and handling of large, highly irradiated reactor components, it is either very difficult or impractical to obtain directly applicable void swelling data from actual PWR internals that have reached an end-of-life (EOL) condition. Therefore, a method commonly used to infer such information is to extrapolate more abundant data obtained under liquid metal, fast breeder reactor (LMFBR) conditions to PWR EOL or life-extension conditions. Many uncertainties are involved in this process, and the outcome of such extrapolation is often considered either unconvincing or questionable. Even for a given irradiation temperature and given steel, the integral effects of dose and dose rate on void swelling cannot be separated. It is incorrect to extrapolate swelling data on the basis of "progressive compounded multiplication" of separate effects of factors such as dose, dose rate, temperature, and material composition.

Compared to LMFBRs, the neutrons resulting from the fission process in LWRs are moderated and slowed, or "thermalized", resulting in a higher probability of their capture by surrounding materials. As these thermal neutrons bombard the structural materials that support the fuel and reactor core components, the atoms of the material are displaced, often much more than just once, resulting in the production of large numbers of vacancies and interstitials, with important consequences on strength and resistance to failure of these materials. Simultaneous with the bombardment and consequent damage, the moderately high temperatures of the core internal materials [ $\approx 338^\circ\text{C}$  ( $\approx 640^\circ\text{F}$ )] produce an offsetting process of annealing and consolidation of the radiation damage into voids, dislocation loops and other microscopically faulted structures.\* In addition, many of the point defects formed through neutron bombardment simply diffuse to sinks of various types, including external surfaces, grain boundaries, or interphase surfaces. If the temperatures are high [ $400\text{--}560^\circ\text{C}$  ( $752\text{--}1040^\circ\text{F}$ )] and the irradiation damage extensive ( $>10^{23}\text{ n/cm}^2$ ), the voids that are formed could conceivably produce dimensional changes, resulting in misfitting of the components, increases in stress, and other unacceptable consequences.

The data from investigations related to LMFBR performance shows the void swelling process is divided into two phases – an incubation period, followed by a period of void formation. Once voids have started to form, a general rule of thumb is that swelling proceeds at a rate of 1% per dpa accumulated.

1. \_\_\_\_\_

\* Neutrons can also cause transmutation of some of the lighter elements such as boron, generally found in trace amounts in structural materials. However, the amounts of helium and possibly hydrogen that are produced by transmutation of light elements is not likely to contribute significantly to void formation. Thermal neutron bombardment of nickel can produce a few parts per million amounts of helium during the course of a reactor lifetime, which could contribute to void production.

However, the incubation period is influenced by a number of important variables, including cold work, which tends to extend the period of incubation, and metal chemistry, which can either extend or foreshorten the incubation period. Because cold work extends the onset of swelling, core baffle bolts are frequently fabricated from 20% cold-worked (CW), Type 316 SS.

The available database on void swelling and density change of austenitic SSs has been critically reviewed. Irradiation conditions, test procedures, and microstructural characteristics were carefully examined, and key factors that are important to determine the relevance of the database to PWR conditions were evaluated. A topical report on the subject has been prepared.

Limited swelling data are available for cold-worked (CW) Type 316 SS irradiated to 53 dpa at 376–386°C (709–727°F) and for solution-annealed (SA) Type 304 SS irradiated to 50 dpa at ≈370°C (≈698°F) in EBR-II reflector positions at dose rates comparable to those of PWR reentrant corners. As such, these data are relevant to the conditions of PWR reentrant corners. Swelling in these materials was <1%.

The low degree of void swelling observed in PWR components and in EBR-II steels under PWR-relevant dose rates appears to be associated with irradiation-induced formation of very fine precipitates (such as G phase, carbides, and  $\gamma'$  phase) in high number density. Such irradiation-induced precipitation at low temperatures (<370°C) creates an extremely large internal surface, i.e., the interface between the steel matrix and the precipitates. This interface acts as an efficient sink to irradiation-induced vacancies, thereby suppressing the agglomeration of the vacancies. Irradiation-induced precipitation is sensitive to minor alloying and impurity elements, irradiation temperature, and dose rate.

The available void swelling data for PWR core internals<sup>114–119</sup> are plotted in Fig. 37 in terms of irradiation temperature and dose (dpa); a higher level of swelling is denoted with a larger circle with a darker color. Figure 38 shows a plot of void swelling of PWR internals as function of dose. The maximum observed void swelling was 0.020–0.24% at ≈333–343°C (631–649°F) and 7.5–12.2 dpa for the flux thimble tube and baffle bolts fabricated from CW Type 316 SS. No swelling larger than 0.25% was observed. This level of swelling is insignificant.

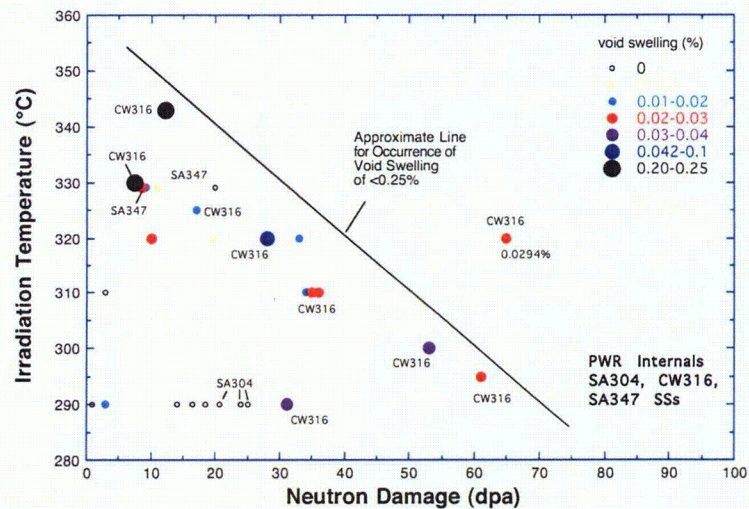


Figure 37. Range of irradiation temperature and dose for which void swelling data (in color code) have been reported for PWR core internals.

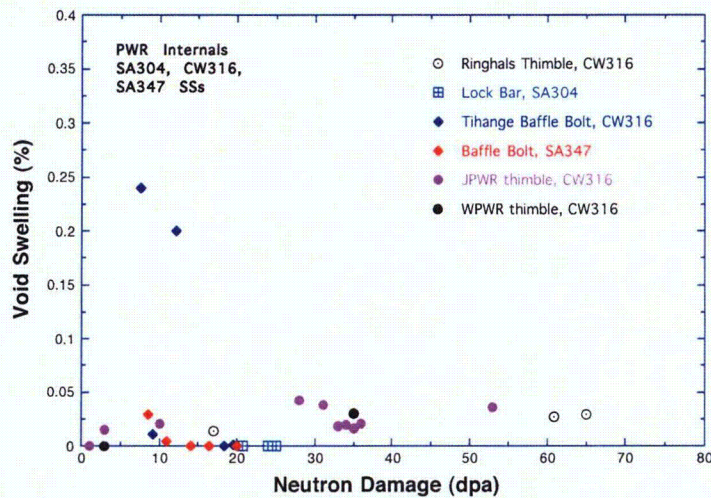


Figure 38. Void swelling of PWR internals plotted as a function of dose (dpa).

In thin-walled flux thimbles and instrument tubes, the effect of gamma heating is insignificant. The currently available database is sufficient to conclude that void swelling in this type of reactor internal, mostly fabricated from CW Type 316 SS, is not an issue.

Most PWR baffle bolts are fabricated from CW Type 316 SS. The data obtained from the industry baffle bolt program show that swelling is insignificant (<0.25%) for dose levels up to  $\approx 20$  dpa and irradiation temperatures of up to  $\approx 340^\circ\text{C}$  ( $\approx 644^\circ\text{F}$ ). Data obtained on EBR-II components irradiated at temperatures  $<380^\circ\text{C}$  ( $<716^\circ\text{F}$ ) and at comparable dose rates are consistent with the data from the industry bolt program. Microstructural characteristics of the two groups of materials are also consistent. Thus, it is not likely that void swelling in this type of reactor internal will exceed the threshold level (i.e.,  $\approx 4\%$ ) that is necessary to enter the regime of the steady-state swelling rate of  $1\%/dpa$ .

Most baffle reentrant corners are fabricated from SA Type 304 SS and are most susceptible to high swelling rates, and hence, high swelling at EOL. The maximum irradiation temperature in some regions of the reentrant corners has been estimated to be in the range of  $\approx 380\text{--}420^\circ\text{C}$  ( $716\text{--}788^\circ\text{F}$ ). Figure 39 shows the data from steels irradiated in EBR-II at  $376\text{--}460^\circ\text{C}$  ( $709\text{--}860^\circ\text{F}$ ); some data reported by Allen et al.<sup>120</sup> for CW Type 316 SS at  $376\text{--}386^\circ\text{C}$  ( $709\text{--}727^\circ\text{F}$ ) and by Chung et al.<sup>121</sup> for SA Type 304 SS at  $370^\circ\text{C}$  ( $698^\circ\text{F}$ ), are also included in the figure. The steel specimens were obtained from fuel subassemblies (1-mm-thick hex can) located in the reflector region of the reactor. In that location, the steels are irradiated at lower temperatures, and their dose rates are about one order of magnitude lower than that in the fueled region. As such, the data are more relevant to the behavior of a PWR reentrant corner than the data obtained from steels irradiated at higher temperatures in the core center.

The only investigation on void swelling for SA Type 304 SS shows that void swelling in this material after irradiation in the EBR-II reactor to  $\approx 50$  dpa at  $370^\circ\text{C}$  and a dose rate comparable to that of reentrant corners, was only 0.54%. The low swelling appears to be related to high-density irradiation-induced precipitation of very fine carbides. Therefore, it is considered unlikely that void swelling in reentrant corners will exceed the threshold level of  $\approx 4\%$ . As a consequence, the potential impact of void swelling on core flow and the structural functions of the PWR internals is believed to be negligible.

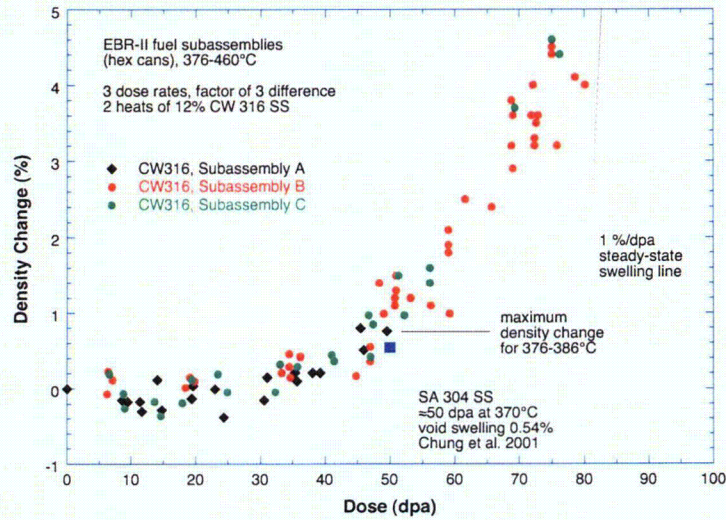


Figure 39. Density change in CW Type 316 SS fuel hex can irradiated in reflector region of EBR-II at 376-460°C to 5-80 dpa.

However, this estimation is only preliminary. More relevant swelling data, including the effects of dose rate and temperature would be extremely helpful. Analyses to compute more accurate quantification of maximum temperature at EOL and life-extension situations are needed for SA Type 304 and Type 316 SSs. A better mechanistic understanding of the roles of irradiation-induced microstructural evolution on void swelling is also needed. Several experimental programs to address these issues are underway, and are expected to produce useful data in the next few years.



## 5 Cracking of Nickel Alloys and Welds

---

### 5.1 Introduction

This part of the study consists primarily of establishing CGRs under constant and cyclic loading and evaluating Ni alloys and weld metals metallographically to develop comprehensive and statistically significant analyses that could be used to determine the dependence of the SCC of these materials on alloy composition, microstructure, water chemistry, temperature, and other factors. The Ni-base alloys used as construction material in LWRs have experienced SCC. Primary-water SCC of Alloy 600 steam generator tubes in PWRs has been studied intensively.<sup>122-124</sup> Stress corrosion cracking has also occurred in Ni alloys used in applications such as instrument nozzles and heater thermal sleeves in the pressurizer<sup>125</sup> and CRDM penetrations in the reactor vessel closure heads.<sup>126</sup> In the fall of 1991, a leak was discovered in the pressure vessel head penetration at the Bugey 3 plant in France. Metallurgical evaluations indicated that the leak was caused by primary water SCC.<sup>127</sup> The main crack had initiated in Alloy 600 base metal and propagated into the Alloy 182 weld metal. Subsequent inspections of CRDM penetrations in domestic and foreign PWRs identified a small number of penetrations (<5% of the penetrations inspected) with axial cracks. None of the cracks was through-wall, and until 2000, no more leaks were found in pressure vessel head penetrations.

Leaks from axial through-wall cracks were identified at Oconee unit 1 in November 2000 and at Arkansas Nuclear One unit 1 in February 2001.<sup>128</sup> During the next 15 months, inspections at Oconee units 2 and 3 and follow up inspection at unit 1 identified both axial and circumferential cracks in reactor vessel head penetrations.<sup>129</sup> The presence of circumferential cracks, in particular, raised concerns regarding structural integrity.<sup>130,131</sup> Also, in October 2000, significant boron deposits were discovered in the vicinity and on the Loop "A" outlet nozzle-to-pipe weld at the V. C. Summer plant.<sup>132</sup> Ultrasonic inspection of the pipe revealed an axial crack in the dissimilar metal weld at the top of the pipe. Earlier in 2000, two shallow axial flaws were found in the outlet nozzle-to-safe-end weld of Ringhals unit 3, and four axial indications were found in the same region of Ringhals unit 4, in Sweden.<sup>133</sup> Cracks have also been found in pressure vessel head penetrations at North Anna unit 2<sup>134</sup> and Davis-Besse nuclear power plant<sup>135</sup> and, more recently, in the bottom-mounted instrumentation nozzles at South Texas unit 1.<sup>136,137</sup>

Long-term operating experience indicates that although wrought Ni-base Alloy 600 is susceptible to SCC, until October 2000, the weld metal Alloys 82 and 182 used with Alloy 600 had not shown environmentally assisted cracking. However, laboratory tests indicate that in PWR coolant environments, the SCC susceptibility of Alloy 182 may be greater than Alloy 600, and that of Alloy 82 may be comparable to Alloy 600. This apparent inconsistency between field and laboratory experience has been an issue that needs further investigation.

A program is being conducted at ANL to evaluate the resistance of Ni alloys and their welds to environmentally assisted cracking in simulated LWR coolant environments. The existing CGR data for Ni alloys under cyclic and constant loads have also been analyzed to establish the effects of key parameters on CGRs; the results are presented elsewhere.<sup>138-143</sup> The fatigue crack growth data in air were analyzed to develop correlations for estimating the fatigue CGRs of Alloys 600 and 690 as a function of stress intensity factor range  $\Delta K$ , load ratio  $R$ , and temperature.<sup>144</sup> The results indicate that in air, the CGRs of these materials are relatively insensitive to changes in frequency. The CGR (m/cycle) of Alloy 600 in air is best expressed as

$$da/dN = C_{A600} (1 - 0.82 R)^{-2.2} (\Delta K)^{4.1}, \quad (29)$$

where  $\Delta K$  is in  $\text{MPa}\cdot\text{m}^{1/2}$ , and the constant  $C_{A600}$  is given by a third-order polynomial of temperature  $T$  ( $^{\circ}\text{C}$ ) expressed as

$$C_{A600} = 4.835 \times 10^{-14} + (1.622 \times 10^{-16})T - (1.490 \times 10^{-18})T^2 + (4.355 \times 10^{-21})T^3. \quad (30)$$

In high-DO water, the CGRs of Alloy 600 show frequency-dependent enhancement under cyclic loading conditions. The environmental enhancement of growth rates does not appear to depend strongly on the material condition. In contrast, environmental enhancement of CGRs of Alloy 600 in low-DO water does seem to be strongly dependent on material conditions. In the literature<sup>145-149</sup> such variability has been attributed to parameters such as yield strength and grain boundary coverage of carbides, although the evidence for this dependence has been best demonstrated for steam generator tubing rather than thicker structural materials.

In the earlier ANL work, correlations were developed to estimate the enhancement of CGRs in LWR environments relative to the CGRs in air under the same loading conditions. The best-fit-curve for Alloy 600, either in solution annealed condition or solution annealed plus thermally-treated condition, in high-DO water ( $\approx 300$  ppb DO) at  $289^{\circ}\text{C}$  is given by the expression<sup>140</sup>

$$\text{CGR}_{\text{env}} = \text{CGR}_{\text{air}} + 4.4 \times 10^{-7} (\text{CGR}_{\text{air}})^{0.33}. \quad (31)$$

In low-DO PWR water, for the alloys that show environmental enhancement, the CGRs at  $320^{\circ}\text{C}$  are comparable to that predicted by Eq. (31). Also, studies on cyclic CGRs in PWR water in Ni-alloy welds, e.g., Alloys 82 and 182, have found limited environmental enhancement,<sup>150-154</sup> although as noted previously based on laboratory tests, Alloy 182 is generally thought to be more susceptible to SCC than Alloy 600. Frequency-dependent environmental enhancement is usually associated with susceptibility to SCC under constant loading conditions.

The SCC data for Alloy 600 have been reviewed to determine the effects of critical parameters such as stress intensity factor, temperature, material heat treatment, cold work, and water chemistry on growth rates.<sup>144,155-158</sup> The CGR (m/s) under SCC conditions is represented by the correlation,

$$\text{CGR}_{\text{SCC}} = \alpha \exp \left[ -\frac{Q}{R} \left( \frac{1}{T} - \frac{1}{598} \right) \right] (K - 9)^{1.16}, \quad (32)$$

where  $Q$  is the thermal activation energy for crack growth (130 kJ/mol),  $R$  is the universal gas constant,  $T$  is the absolute operating temperature,  $K$  is the stress intensity factor ( $\text{MPa}\cdot\text{m}^{1/2}$ ), and  $\alpha$  is the crack amplitude.<sup>158</sup> At  $325^{\circ}\text{C}$  a value of  $2.67 \times 10^{-12} \text{ MPa}\cdot\text{m}^{1/2}$  has been proposed for  $\alpha$ .

This annual report presents CGR data in the PWR environment for Alloy 600 from the Davis-Besse CRDM nozzle #3, and Alloys 82 and 182 from the V. C. Summer reactor nozzle-to-pipe weld. The results have been compared with the existing CGR data for Ni-alloy welds to determine the relative susceptibility of these materials to environmentally enhanced cracking under a variety of loading conditions. Detailed metallographic examinations of the material to characterize the microstructure of the weld metal are presented.



## 5.2 Crack Growth Rates of Alloy 600 from the Davis–Besse CRDM Nozzle #3 in PWR Environment (O. K. Chopra, B. Alexandreanu, and W. J. Shack)

Crack growth tests were conducted on specimens of Alloy 600 removed from Davis–Besse (D–B) CRDM nozzle #3 in a PWR environment at 316°C under cyclic loading for a sawtooth waveform with 30–1000 s rise times and at constant load, with or without periodic partial unloading. The results are compared with the existing CGR data for Alloy 600 to determine the relative susceptibility of D–B material to environmentally assisted cracking. The results of a detailed metallographic examination of the material to characterize its microstructure and fracture morphology are presented.

### 5.2.1 Experimental

#### 5.2.1.1 Material and Specimen Geometry

At the Davis–Besse reactor, CRDM nozzles #1–5 were fabricated from Alloy 600 seamless tubing per ASME SB–167 (Heat M3935). The final mill anneal temperature is estimated to be 871–927°C (1600–1700°F). The mill–certified chemical composition of the nozzle alloy are given in Table 9. The room–temperature tensile properties for the material are yield strength of 334 MPa (48.5 ksi), tensile strength of 590 MPa (85.6 ksi), and elongation of 60%.

A ring from D–B CRDM Nozzle #3 (Fig. 40) having 102–mm (4.0–in.) outer diameter, 16–mm (0.625–in.) wall thickness, and 64–mm (2.5–in.) length was received from BWX Technologies, Inc., in Lynchburg, VA. The nozzle ring was produced from two transverse cuts made at BWXT Technologies through the nozzle at 25 and 89 mm (1 and 3.5 in.) from the bottom of the nozzle (near the J–groove weld end). It is estimated that ≈114 mm (4.5 in.) of the nozzle end was bored away during the removal process at the D–B site. To decrease the surface activity, ≈1.25 mm (≈0.05 in.) of material was machined from the ID and ≈0.50 mm (≈0.02 in.) from the OD of the nozzle ring.

Cylindrical tensile, 1/4–T CT, and 0.35 x 1/2–T CT specimens were machined from the nozzle ring. The configuration of the tensile and 1/4–T CT specimens is shown in Figs. 41 and 42, and the orientation of the specimens is shown in Fig. 43. The tensile specimens were obtained only in the longitudinal (or

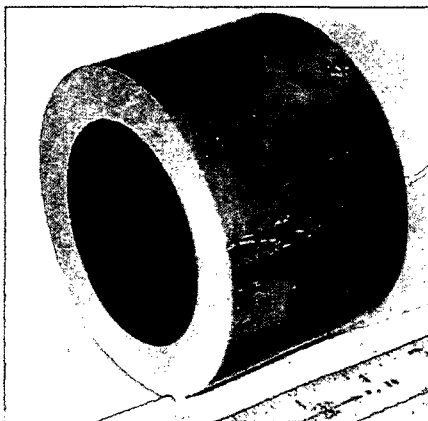


Figure 40.  
Photograph of the ring from Davis–Besse  
CRDM Nozzle #3.

Table 9. Chemical composition (wt.%) and tensile properties of Alloy 600 from D–B Nozzle #3.

C	Mn	Fe	P	S	Si	Cu	Ni	Cr	Co
0.028	0.27	6.25	0.004	0.002	0.37	0.01	77.89	15.58	0.01

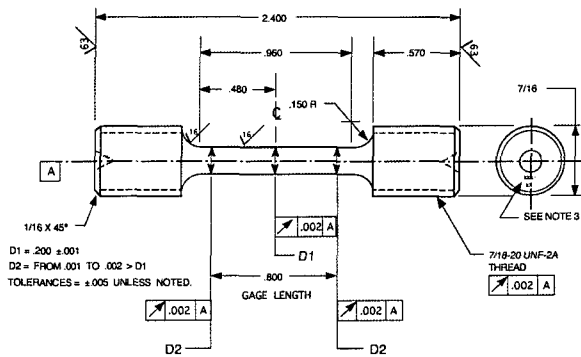


Figure 41. Configuration of the cylindrical tensile specimen.

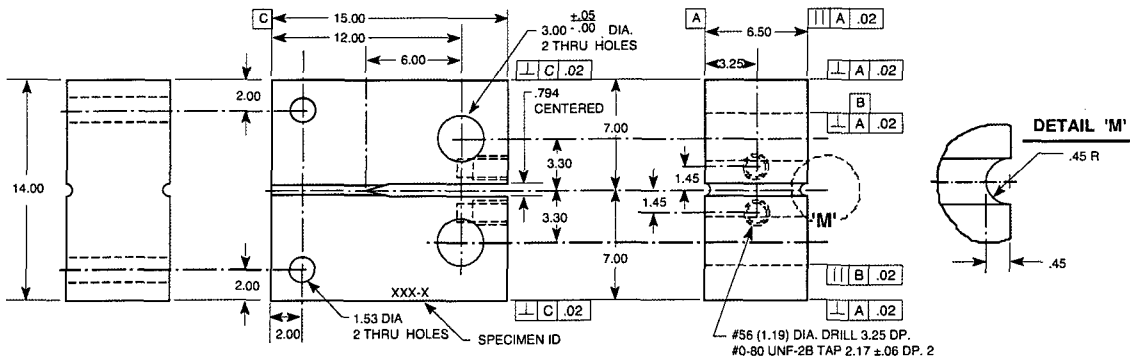


Figure 42. Configuration of the 1/4-T compact tension specimen.

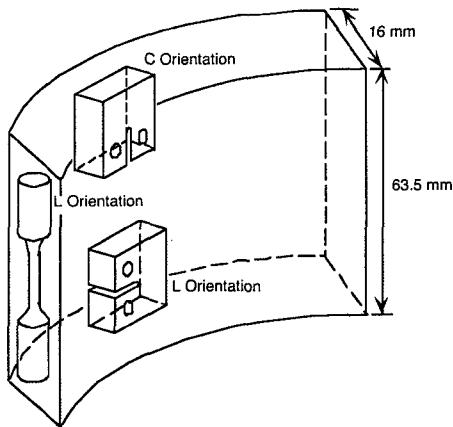


Figure 43. Orientation and location of the test specimens taken from the Davis-Besse CRDM nozzle.

axial) orientation, and the CT specimens, in both longitudinal (L) and circumferential (C) orientation (i.e., corresponding to circumferential and axial crack, respectively). For the C orientation, the direction normal to the fracture plane is in the circumferential direction, and the crack growth is in the longitudinal direction, and vice versa for the L orientation. A radiological survey of the tensile and CT specimens indicated  $<0.1$  mR/h  $\beta\gamma$  on contact and no loose activity.

### 5.2.1.2 Material Characterization

The nozzle material microstructure was characterized along the longitudinal and circumferential planes. The specimens were mechanically polished by means of 1- $\mu\text{m}$  diamond paste and etched with Marble's reagent (hydrochloric acid, copper sulfate, and distilled water solution). A typical microstructure

obtained along the longitudinal and circumferential planes is shown in Fig. 44. The grain size varies significantly, e.g., 30 to 200  $\mu\text{m}$ , with an average size of  $\approx 75 \mu\text{m}$  (ASTM grain size 4). The material shows extensive grain boundary coverage (GBC) of Cr-rich carbides and a few carbides randomly distributed in the matrix. Although in most cases the boundaries are decorated with carbides, in some cases the carbides appear to be only on one side of the boundary, e.g., the boundary going from top left to bottom right in Fig. 44. The large precipitates in the grain matrix were identified as mostly Ti carbonitrides. The average size of the grain-boundary carbides was  $\approx 0.3 \mu\text{m}$ , and the GBC was estimated to be 50–60%. Also, microhardness measurements indicated a uniform hardness across the nozzle wall.

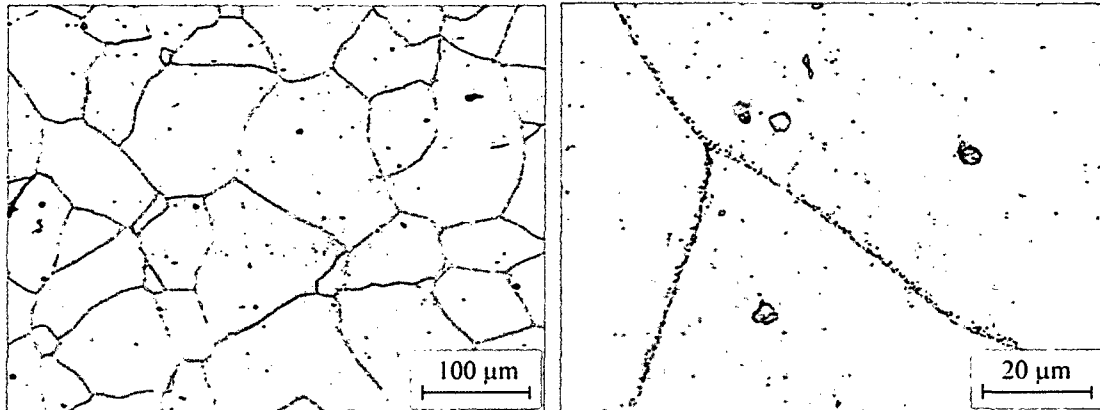


Figure 44. Typical microstructure observed along longitudinal or circumferential planes for Alloy 600 from D-B CRDM nozzle #3.

### 5.2.1.3 Crack Growth Test Facility and Procedure

The facility for conducting the CGR tests consists of a 1-L SS autoclave with a recirculating water loop. The load frame, hydraulic actuator, autoclave, and the furnace are mounted on top of a portable wheeled cart. An Instron Model 8500+ Materials Testing System is used to perform the tests. The PWR water is circulated from a 135-L SS storage tank through a high-pressure pump, regenerative heat exchanger, autoclave preheater, test autoclave, ECP cell and preheater, regenerative heat exchanger, and Mity Mite™ back-pressure regulator. This water is then returned to the storage tank. Water is circulated at flow rates of 15–40 mL/min. Also, water samples are taken periodically to measure pH, resistivity, and DO concentration in the feedwater. This facility is similar to the ANL facility used for in-cell testing of irradiated materials and is described in detail elsewhere.<sup>112</sup> The PWR water consists of high-purity water containing  $\approx 1000$  ppm B, 2 ppm Li,  $<30$  ppb DO, and  $\approx 2$  ppm dissolved hydrogen ( $\approx 23$  cc/kg). The room-temperature pH is  $\approx 6.4$ .

The CGR tests were performed in accordance with ASTM E-647 “Standard Test Method for Measurement of Fatigue Crack Growth Rates” and ASTM E-1681 “Standard Test Method for Determining a Threshold Stress Intensity Factor for Environment-Assisted Cracking of Metallic Materials under Constant Load.” Crack extension was monitored by DC potential measurements.

All specimens were fatigue precracked in PWR water at load ratio  $R = 0.3$ , frequency of  $\approx 0.5$ –2 Hz, and maximum stress intensity factor  $K_{\text{max}}$  of 19–21  $\text{MPa m}^{1/2}$ . After  $\approx 0.3$  mm extension,  $R$  was increased incrementally to 0.7, and the loading waveform changed to a slow/fast sawtooth with rise times of 30–1000 s. Constant-load tests with periodic partial unloading were conducted with the trapezoidal waveform,  $R = 0.7$ , hold period at peak of 1 or 2 h, and unload/reload period of 24 s. In all tests,  $K_{\text{max}}$  was maintained approximately constant by periodic load shedding. After the test, the final crack size was

marked by fatigue cycling at room temperature. The specimen was then fractured, and the final crack length was measured from metallographic examination of the fracture surface by optical or scanning electron microscopy. The final crack length was measured from the photograph by the 9/8 averaging technique, i.e., nine measurements were taken across the width of the specimen at equal intervals, the two near-surface measurements were averaged, and the resultant value was averaged with the remaining seven measurements.

The experimental data were consistent with the screening criteria of Ref. 159. All specimens showed 100% engagement (i.e., crack extension occurred over the entire machine notch, and the crack front was relatively straight). Also, under environmentally enhanced conditions, fracture morphology was predominantly intergranular (IG, 90% or greater). The CGR during each test period was determined from the slope of the corrected crack length vs. time plots. For cyclic loading, only the rise time was used to determine growth rate. The crack extension during each test period was at least 10 times the resolution of the DC potential drop method, i.e., typically 5  $\mu\text{m}$ . Thus, crack extensions were at least 50  $\mu\text{m}$ ; for test conditions with very low CGRs (e.g., less than  $1 \times 10^{-11}$  m/s), smaller crack extensions were used to reduce testing time.

To ensure that the experimental data obtained from differing specimen geometry, thickness, and loading conditions can be compared with each other and applied to reactor components, the CGR data were validated in accordance with the specimen size criteria of ASTM E-1681 and E-647. For high-strain-hardening materials with ultimate-to-yield-stress ratio  $\geq 1.3$ , both requirements allow the use of flow stress defined as  $\sigma_f = (\sigma_{\text{ult}} + \sigma_{\text{ys}})/2$  rather than the yield stress.

## 5.2.2 Results

### 5.2.2.1 Tensile Strength in Air

The tensile tests were performed in accordance with ASTM Specifications E8 and E21 in an Instron tensile test machine in air at 316°C and a strain rate of  $4 \times 10^{-4}$  s<sup>-1</sup>. The cross-head movement and digitized load were recorded as a function of time. The values for the 0.2% yield stress and ultimate stress are given in Table 10. The engineering stress-vs.-strain curves for the three specimens from the nozzle alloy are given in Fig. 45. The tensile strength of the material is comparable to the typical value observed for thick-section Alloy 600 products.

Table 10. Tensile test results at 316°C for Alloy 600 from D-B CRDM nozzle #3.

Specimen ID	0.2% Yield Stress, MPa	Ultimate Stress, MPa	Elongation, %	Reduction in Area, %
N3TL-1	290	549	62.3	51.8
N3TL-2	250	547	67.9	54.1
N3TL-3	283	549	63.8	54.0

### 5.2.2.2 Crack Growth Rates in PWR Environment

Crack growth tests have been completed on 1/4-T CT specimens in L and C orientations (N3CL-1 and N3CC-2, respectively) and 1/2-T CT specimen (N3CC-3) in the C orientation. The test conditions, experimental CGRs, the allowed  $K_{\text{max}}$  from K/size criterion, and the margin between the applied and allowed  $K_{\text{max}}$  are given in Tables 11-13. The allowed  $K_{\text{max}}$  was calculated using flow stress instead of yield stress. For specimen N3CL-1, the constant-load CGRs were not obtained because at 840 h the CGR increased abruptly by a factor of 5. It was assumed that the applied  $K_{\text{max}}$  may have exceeded the

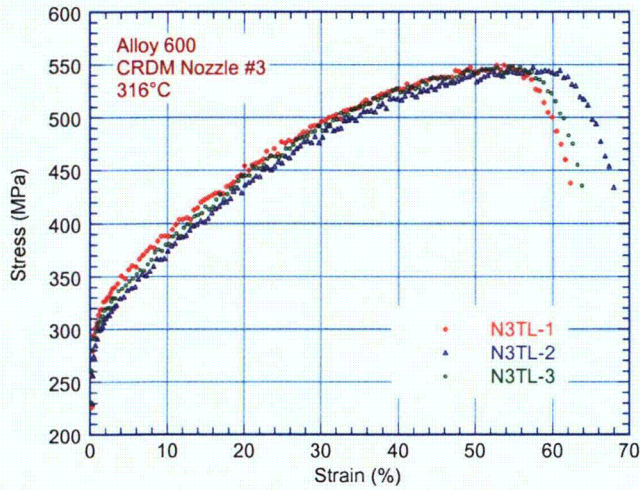


Figure 45.  
Engineering stress-vs.-strain curve at 316°C for Alloy 600 from D-B CRDM nozzle #3.

value allowed by the  $K$ /size criterion, and the test was terminated. The tests on N3CL-1 and N3CC-2 were interrupted once because of leaks: at 194 h for N3CL-1, because of a leak in the Bal-seal between the pull rod and the autoclave, and at  $\approx 1220$  h for N3CC-2, because of a leak in the ECP cell. In both cases the test was restarted, and the growth rates prior to the interruption were restored. Complete test results, including plots of the change in crack length and  $K_{max}$  with time during various test periods, are presented in a topical report entitled “Crack Growth Rates in a PWR Environment of Nickel Alloys from the Davis-Besse and V. C. Summer Power Plants.”

Micrographs of the fracture surfaces of the three specimens are shown in Figs. 46–48. The actual crack extensions were 83, 74, and 57% greater than the values determined from the DC potential drop measurements for specimens N3CL-1, N3CC-2, and N3CC-3, respectively. This difference most likely is due to the presence of unbroken ligaments on the fracture surface. Crack extensions estimated from the DC potential method were scaled proportionately; the corrected values of  $K_{max}$  and growth rate are given in Tables 11–13. The results indicate that for specimens N3CL-1 and N3CC-2, the applied  $K_{max}$  for most of the test periods was  $\approx 25\%$  higher than the value allowed by the  $K$ /size criterion; the loading conditions for specimen N3CC-3 were within the allowed values.

Table 11. Crack growth results for 1/4-T CT Specimen N3CL-1 of Alloy 600 in PWR water at 316°C.

Test Period	Test Time, h	ECP at 289°C, <sup>a</sup> mV (SHE) Pt	Conduc-tivity, A600 $\mu\text{S}/\text{cm}$ , <sup>a</sup>	R Load Ratio	Rise Time, s	Down Time, s	Hold Time, s	$K_{max}$ , $\text{MPa}\cdot\text{m}^{1/2}$	$\Delta K$ , $\text{MPa}\cdot\text{m}^{1/2}$	Growth Rate, m/s	Allowed $K_{max}$ , $\text{MPa}\cdot\text{m}^{1/2}$	Crack Length, mm	
Pre a	51	-440	-434	21.0	0.26	1	1	0	20.0	14.8	5.07E-09	20.3	5.993
Pre b	71	–	–	–	0.28	5	5	0	19.4	14.0	3.09E-09	20.1	6.117
1	115	–	–	–	0.53	30	4	0	21.2	9.9	4.30E-10	19.9	6.199
2	194	–	–	18.5	0.54	300	4	0	21.5	9.9	2.55E-10	19.9	6.240
3a	225	-584	-585	18.5	0.52	300	4	0	22.7	10.9	8.88E-11	19.8	6.269
3b	316	–	–	14.7	0.51	300	4	0	24.5	12.0	2.63E-10	19.7	6.353
4	436	–	–	12.8	0.71	300	4	0	25.3	7.3	1.10E-10	19.6	6.400
5	676	–	–	15.4	0.70	1000	12	0	24.5	7.3	negligible	19.6	6.398
6	722	–	–	15.4	0.51	300	4	0	25.1	12.3	4.42E-10	19.5	6.471
7a	818	–	–	13.0	0.50	1000	12	0	24.6	12.3	5.45E-11	19.4	6.493
7b	868	–	–	13.0	0.51	1000	12	0	25.6	12.5	3.73E-10	19.3	6.562

<sup>a</sup>Represents values in the effluent. Feedwater conductivity was about the same as in the effluent. Water flow rate was 50 cc/min.

Table 12. Crack growth data for 1/4-T CT Specimen N3CC-2 of Alloy 600 in PWR water at 316°C.

Test Period	Test Time, h	ECP at 289°C, <sup>a</sup> mV (SHE)		Conduc - tivity, μS/cm <sup>a</sup>	R Load Ratio	Rise Time, s	Down Time, s	Hold Time, s	K <sub>max</sub> , MPa·m <sup>1/2</sup>	ΔK, MPa·m <sup>1/2</sup>	Growth Rate, m/s	Allowed K <sub>max</sub> , MPa·m <sup>1/2</sup>	Crack Length, mm
Pre a	189	-	-	22	0.31	5	5	0	23.1	15.9	7.52E-10	19.9	6.243
1	383	-	-	20	0.51	300	4	0	22.3	10.9	2.13E-11	19.8	6.270
2	457	-	-	17	0.51	30	4	0	22.9	11.2	6.05E-11	19.7	6.335
3	550	-706	-704	16	0.51	300	4	0	22.8	11.2	9.46E-12	19.7	6.338
4	580	-	-	15	0.51	30	4	0	24.9	12.2	8.59E-10	19.6	6.415
5	765	-	-	15	0.50	300	12	0	24.8	12.4	8.87E-11	19.5	6.471
6	885	-	-	15	0.70	300	12	0	25.0	7.5	5.28E-11	19.4	6.492
7	912	-	-	16	0.51	300	12	0	25.1	12.3	1.01E-10	19.4	6.502
8	1197	-	-	20	0.52	300	12	3600	25.7	12.4	6.92E-11	19.3	6.541
9	1365	-	-	21	0.48	300	12	0	24.6	12.8	7.53E-11	19.2	6.617
10	1530	-	-	21	1.00	-	-	-	24.7	-	9.67E-11	19.1	6.658

<sup>a</sup>Represents values in the effluent. Feedwater conductivity was about the same as in the effluent. Water flow rate was 42 cc/min.

Table 13. Crack growth data for 1/2-T CT Specimen N3CC-3 of Alloy 600 in PWR water at 316°C.

Test Period	Test Time, h	ECP at 289°C, <sup>a</sup> mV (SHE)		Conduc - tivity, μS/cm <sup>a</sup>	R Load Ratio	Rise Time, s	Down Time, s	Hold Time, s	K <sub>max</sub> , MPa·m <sup>1/2</sup>	ΔK, MPa·m <sup>1/2</sup>	Growth Rate, m/s	Allowed K <sub>max</sub> , MPa·m <sup>1/2</sup>	Crack Length, mm
Pre a	50	-587	-585	20	0.36	0.25	0.25	0	20.8	13.3	1.35E-08	27.6	12.777
Pre b	56	-	-	20	0.35	0.25	0.25	0	20.2	13.1	8.41E-09	27.5	12.872
Pre c	71	-	-	19	0.33	5.0	5.0	0	19.9	13.3	2.03E-09	27.4	12.943
Pre d	78	-	-	19	0.32	0.5	0.5	0	20.7	14.1	1.31E-08	27.2	13.065
1	97	-	-	18	0.50	12	4	0	20.6	10.3	9.08E-10	27.1	13.157
2	122	-	-	18	0.50	60	4	0	20.8	10.6	3.55E-10	27.1	13.186
3	147	-	-	18	0.50	300	4	0	20.9	10.9	2.80E-10	27.1	13.206
4	174	-	-	17	0.70	1,000	12	0	21.2	7.8	2.18E-10	27.0	13.249
5a	230	-	-	16	1.00	-	-	-	20.5	-	7.85E-11	27.1	13.264
5b	339	-	-	15	1.00	-	-	-	20.9	-	1.25E-10	26.9	13.319
6a	386	-	-	14	1.00	-	-	-	26.4	-	2.28E-10	26.8	13.404
6b	529	-	-	12	1.00	-	-	-	26.7	-	1.55E-10	26.7	13.510
7	648	-546	-539	12	1.00	-	-	-	31.9	-	negligible	26.5	13.637

<sup>a</sup>Represents values in the effluent. Feedwater conductivity was about the same as in the effluent. Water flow rate was 40 cc/min.

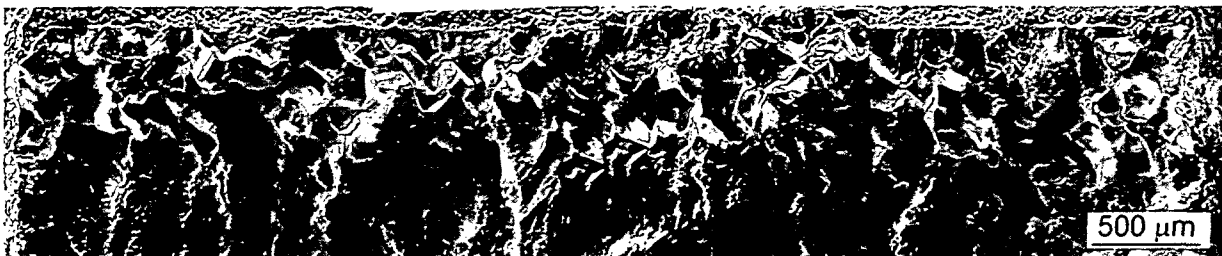


Figure 46. Micrograph of the fracture surface of Specimen N3CL-1. Crack advance from top to bottom.



Figure 47. Micrograph of the fracture surface of Specimen N3CC-2. Crack advance from bottom to top.

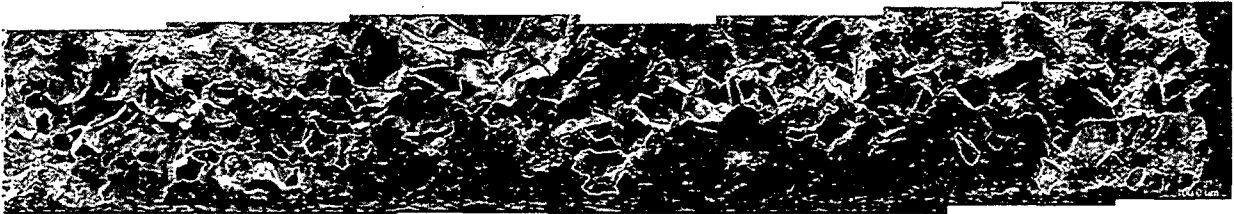


Figure 48. Micrograph of the fracture surface of Specimen N3CC-3. Crack advance from bottom to top.

The results indicate that environmental enhancement of CGRs does not occur from the start of the test. Under more rapid cyclic loading, the crack growth is dominated by mechanical fatigue. The CGRs during precracking and initial periods of cyclic loading were primarily due to mechanical fatigue. For the present tests, environmental enhancement typically was observed at load ratio  $R \geq 0.5$  and rise time  $\geq 30$  s. For example, enhancement occurred after test period 1 for specimens N3CL-1 and N3CC-3 and test period 4 for specimen N3CC-2. These results are consistent with the behavior observed in other heats of Alloy 600 tested under similar loading conditions, i.e., high load ratios and long rise times.<sup>143</sup>

### 5.2.2.3 Fracture Morphology

A unique feature of the fracture surface for the D-B nozzle #3 alloy is the predominantly IG fracture even during mechanical fatigue loading. A TG fracture is observed at the very beginning of the test (near the machine notch), but it changes to IG fracture when the first grain boundary is encountered. These features are better observed in the high magnification micrographs of the fracture surface of specimen N3CL-1 shown in Fig. 49. A slice of the entire crack extension in specimen N3CC-2 is shown in Fig. 50a, and typical fracture morphology at select locations on the surface is shown in Figs. 50b and c. The precrack area at location A shows TG fracture only up to the nearest grain boundary, and location B shows smooth IG fracture. The Ti-rich precipitates on the surface in Fig. 50c do not seem to affect the fracture mode. While the focus of this study was not on the effect of the Ti carbides on the SCC behavior of the alloy at hand, these particles can have a negative impact. As such, the precipitation of Ti carbides can reduce the concentration of free carbon retained in the matrix to a level at which it limits the precipitation of the desirable grain boundary chromium carbides. In addition, if Ti carbides precipitate at grain boundaries they oxidize when exposed to the high temperature water environment, possibly leading to grain boundary embrittlement.

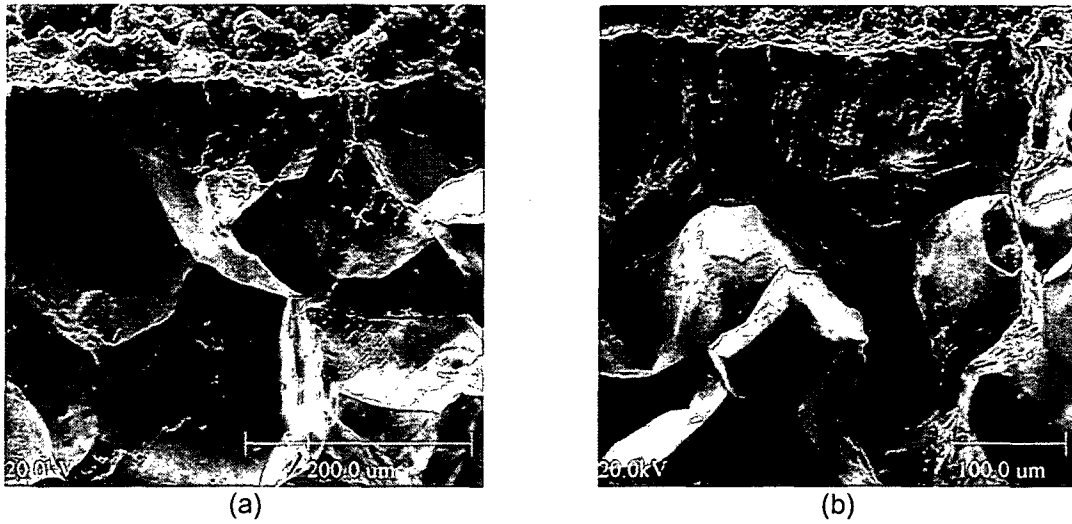


Figure 49. Examples of transition from a transgranular to an intergranular fracture in Specimen N3CL-1.

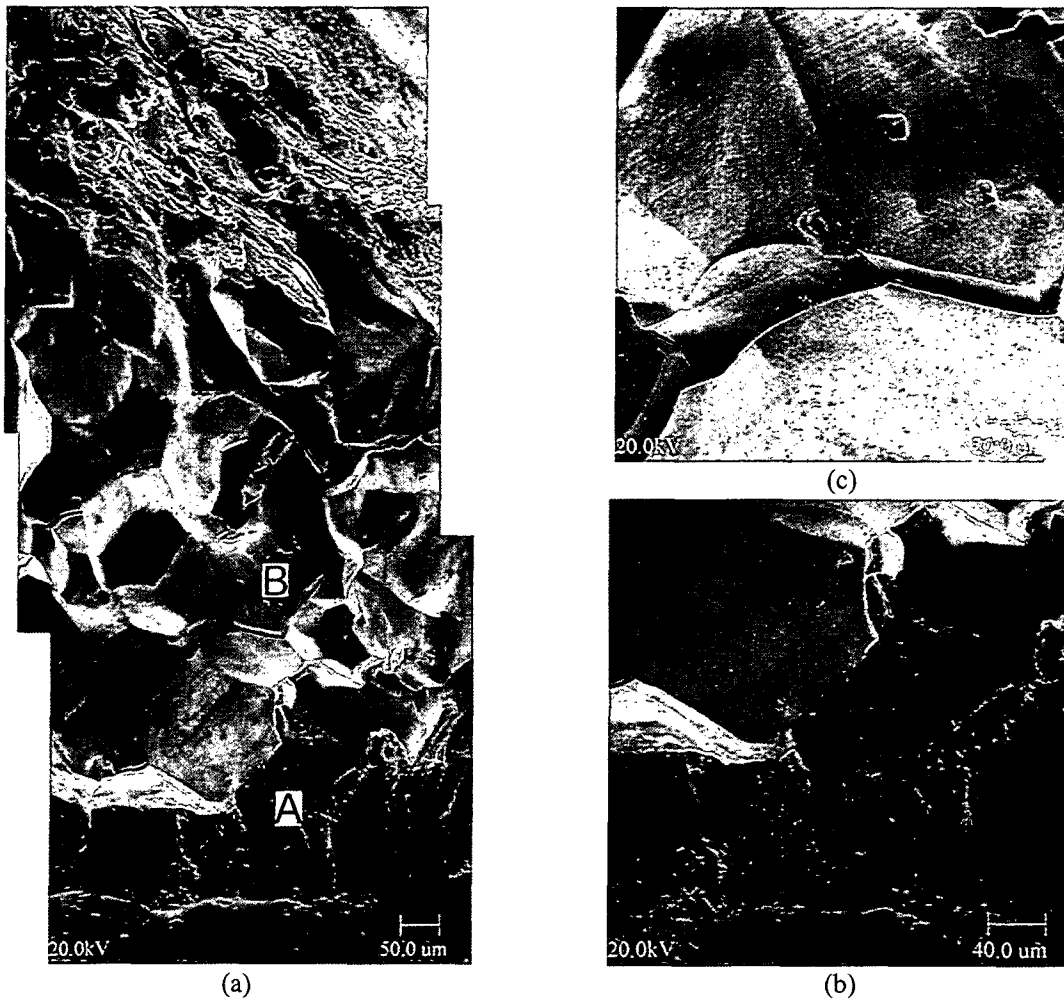


Figure 50. (a) Fracture surface of Specimen N3CC-2, and high-magnification micrographs at locations (b) A and (c) B.



### 5.2.2.3 Crack Growth Rates under Cyclic Loading

The experimental CGRs under cyclic loading are compared in Fig. 51 with those predicted in air under the same loading conditions. Such plots allow direct comparison of cyclic CGR data obtained at different test temperature, load ratio, and frequency. Although the results show considerable scatter environmental enhancement of growth rates is observed in all specimens of the D-B CRDM nozzle alloy. Also, specimen orientation does not seem to have any effect on growth rates, e.g., the CGRs for Specimens N3CL-1 and N3CC-3 are comparable, and those for Specimen N3CC-2 are slightly lower. The cyclic CGRs for the D-B CRDM nozzle Alloy 600 may be represented by the best-fit curve for Alloy 600 in the NWC BWR environment (i.e.,  $\approx 300$  ppb DO at  $289^\circ\text{C}$ ). The experimental CGRs for Specimens N3CL-1 and N3CC-3 are slightly higher than the BWR curve, and those for Specimen N3CC-2 are lower.

The fatigue CGR data obtained earlier at ANL indicated that in low-DO water, environmental enhancement of CGRs seems to depend on material conditions such as yield strength and grain boundary coverage of carbides.<sup>144</sup> Materials with high yield stress and/or poor grain-boundary carbide coverage showed environmental enhancement. The results of the D-B CRDM nozzle #3 Alloy 600 appear to be inconsistent with this trend, e.g., the nozzle #3 alloy has relatively low yield stress and good grain-boundary carbide coverage. However, the loading conditions used in the earlier tests may have influenced environmental effects; although the load ratios were in the range of 0.6–0.9 the rise time for all tests was only 12 s.

The fracture mode also does not seem to influence the cyclic CGRs of the D-B CRDM nozzle Alloy 600. Although the fracture surface of Specimen N3CC-3 (Fig. 48) shows larger fraction of TG fracture than that of Specimen N3CL-1 (Fig. 46), the CGRs for the two specimens are comparable.

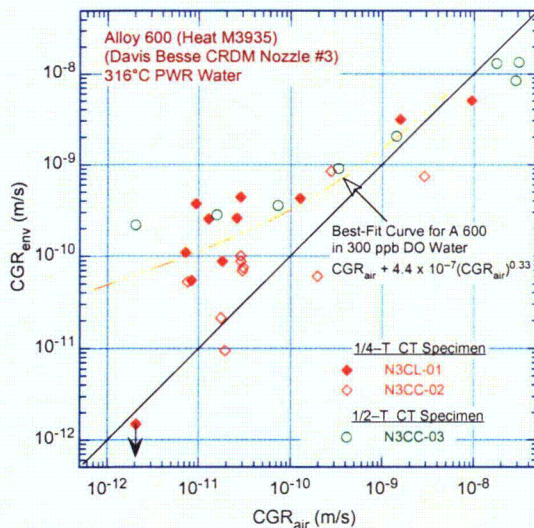


Figure 51.  
CGR data for D-B CRDM nozzle Alloy 600 in PWR water at  $316^\circ\text{C}$  under cyclic loading.

### 5.2.2.4 SCC Growth Rates

The experimental CGRs under constant load with or without partial unloading are plotted as a function of applied  $K_{\text{max}}$  in Fig. 52. The median and 75<sup>th</sup> percentile CGR curves based on the best fit of the data for 26 heats of Alloy 600 (i.e., Eq. 32) are also included in the figure. The CGR curves at  $316^\circ\text{C}$

were calculated for an activation energy of 130 kJ/mol.<sup>158</sup> The growth rates for the D-B nozzle Alloy 600 are a factor of 4–8 higher than the median curve.

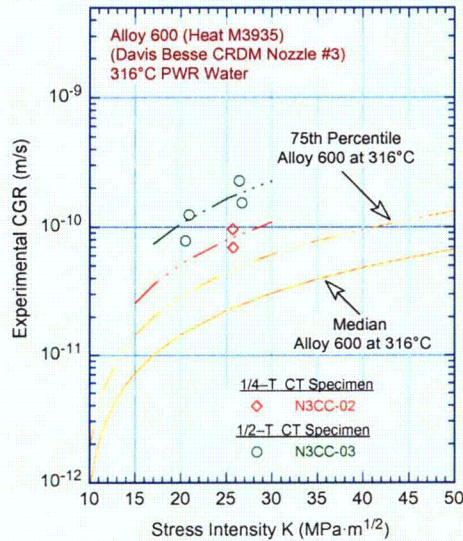


Figure 52.  
CGR data for D-B CRDM nozzle Alloy 600 in PWR water at 316°C under constant load.

Based on the observed microstructure and tensile strength of nozzle Alloy 600, the experimental CGRs are somewhat of a surprise. Materials with good GBC of carbides (Fig. 44) and relatively low or average tensile yield stress (Table 10) are generally considered to have low susceptibility to SCC in PWR water.<sup>144–149</sup> The cumulative distribution of the log-normal fit to the ordered median ranking of the constant  $\alpha$  for various data sets of Alloy 600 is shown in Fig. 53. The experimental CGRs for Alloy 600 from CRDM nozzle #3 correspond to  $\approx 95$  percentile of the distribution fitted to the various data sets, i.e., the nozzle material exhibits very high susceptibility to SCC.

The high susceptibility for the material to SCC cannot be reconciled in terms of the tensile strength or microstructure of the alloy. The extent of IG fracture, particularly under predominantly mechanical fatigue loading, is very unusual for Alloy 600.

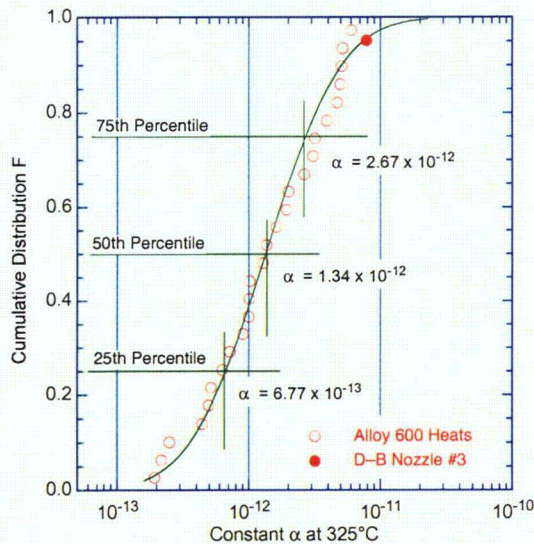


Figure 53.  
Log-normal distribution of constant  $\alpha$  in Eq. 32 for 26 heats of Alloy 600 [158].

### 5.3 Crack Growth Rates of A182 and A82 Alloys from the Vessel Nozzle-to-Pipe Weld of V.C. Summer Reactor (B. Alexandreanu, O. K. Chopra, and W. J. Shack)

This section presents experimental data on CGR of weld butter and weld alloys from the nozzle-to-pipe weld spool piece removed from the hot-leg of the V.C. Summer reactor. To date, two specimens have been tested, one from the butter (Alloy 182) and one from the weld (Alloy 82). In preparation for CGR testing, both butter and weld alloys were characterized metallographically and mechanically at the temperature of interest (320°C). The CGR testing was conducted in a simulated primary water environment, and was complemented by post-test fractographic examinations.

#### 5.3.1 Experimental

This section describes the alloys used, the geometry of the 1/2-T CT specimens, and the apparatus and conditions used for crack growth testing in a primary water environment.

##### 5.3.1.1 Material and Specimen Geometry

The spool piece was contaminated with  $\beta$ - and  $\gamma$ -emitting radionuclides. The radiological survey conducted at ANL found a  $\beta/\gamma$  activity of 885 dpm/100 cm<sup>2</sup> on the inner surface and an activity of 1980 dpm/100 cm<sup>2</sup> on the outer surface. All work described herein was performed in accordance with procedures for handling radioactive materials.

Compact tension specimens were machined from the as-received piece; the configuration of the specimens is shown in Fig. 54. Two specimens have been tested to date, one weld (WCR-01) and one butter (BCR-01). The orientations of these two specimens relative to the as-received piece are shown in Fig. 55. The fracture planes for these tests are highlighted. The first letter in the specimen ID represents weld (W) of butter (B), and the second and third letters represent the orientation of the fracture plane and direction of crack growth, respectively. For the WCR weld specimen, the direction normal to the fracture plane is in the circumferential (C) direction, and the crack growth is in the radial (R) direction. As discussed later, the columnar grains were in the radial direction in the weld and longitudinal direction in the butter. Thus, although the orientation of fracture plane is the same in weld and butter specimens, crack growth was along the columnar grains in WCR-01 and across in BCR-01. A radiological survey of the tensile and CT specimens indicated less than 0.1 mR/h  $\beta/\gamma$  on contact and no loose activity.

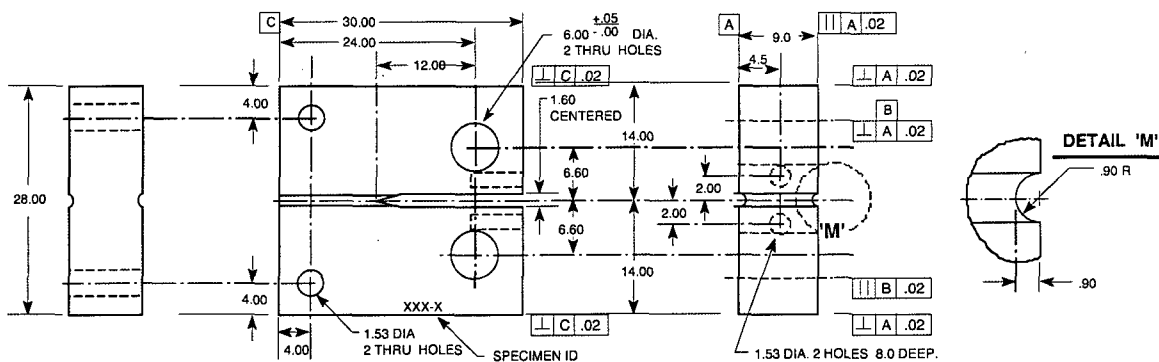


Figure 54. Configuration of the 1/2-T compact tension specimen.

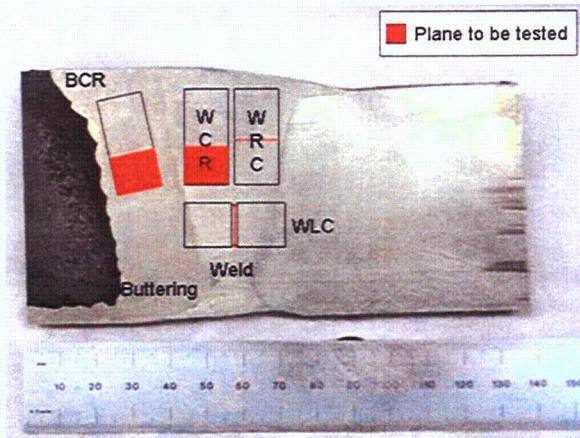
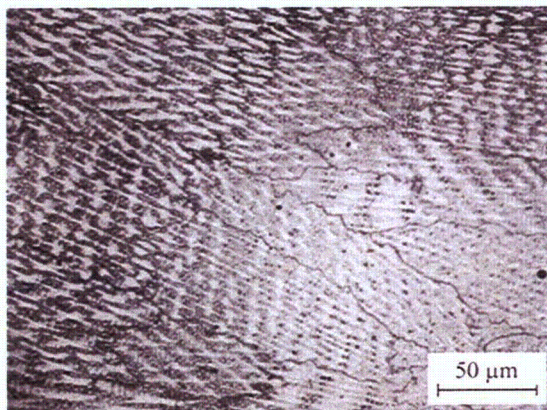
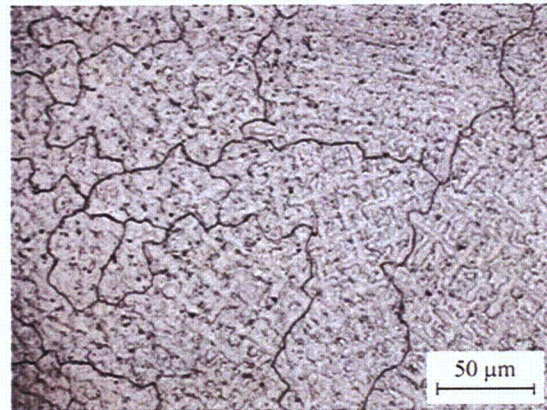


Figure 55. Orientation and location of the test specimens taken from the V.C. Summer piece. Note that relative to the plane of this figure, the longitudinal (L), radial (R), and circumferential (C) directions, respectively, are horizontal, vertical, and into the page.

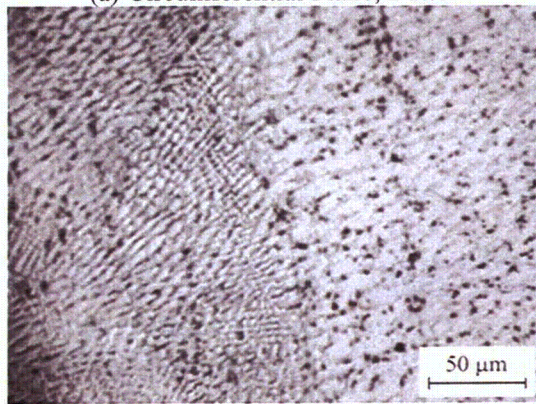
For the examination of the microstructure, coupons representative of both alloys were cut from the piece, mechanically polished through 1- $\mu\text{m}$  diamond paste, and electrochemically etched in a 70%  $\text{H}_3\text{PO}_4$  and water solution at 5 V. The microstructure was observed on planes representative of the CT specimens to be tested. Figure 56 shows micrographs of typical weld microstructures along and across the columnar grains for both, the Alloy 82 weld and Alloy 182 butter. Although the microstructure in the center of the weld along the circumferential plane is not shown in Fig. 56, it was similar to that observed for the butter,



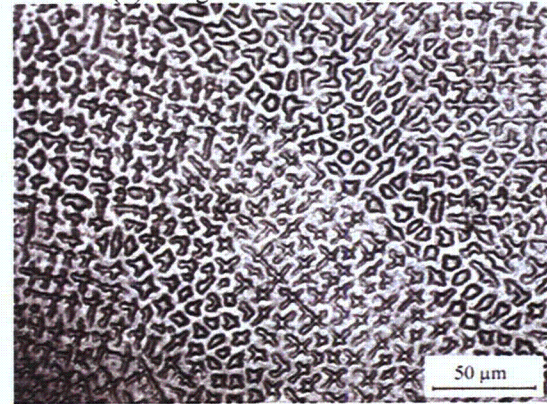
(a) Circumferential Plane, Butter



(b) Longitudinal Plane, Butter



(c) Circumferential Plane, Butter/Weld Interface



(d) Radial Plane, Weld

Figure 56. Microstructure of the V.C. Summer Alloy 82 weld and Alloy 182 butter.

except the columnar grains were vertical. The average size of the columnar grains was  $\approx 50\ \mu\text{m}$  across and  $\approx 150\ \mu\text{m}$  along the length of the grains.

During the microstructural examination, defects were also found in the V.C. Summer weld and weld butter alloys near the ID of the pipe (Fig. 57). Note that this region had gone through weld repairs; all test specimens were obtained from material away from this region. The defects in the weld butter consisted mostly of pores and precipitates distributed uniformly in the microstructure (Fig. 57a). Fewer pores and precipitates were observed in the weld material, but grain boundary sliding was observed at the weld-pipe interface. Several examples of grain boundary sliding are indicated with white arrows in Fig. 57b. Sliding was observed exclusively at the weld fusion line, at grain boundaries extending from the pipe alloy to the weld alloy. This finding is potentially interesting because grain boundary sliding is believed to be a precursor to SCC initiation.<sup>160</sup> In addition, cracks were found at several locations in the weld, sometimes spanning several tens of microns (Fig. 57c). The upper-left insert of Fig. 57c shows the location of this crack in the as-received piece. However, these cracks were not open to the reactor coolant environment, and most probably originated during the cooling of the weld deposit.

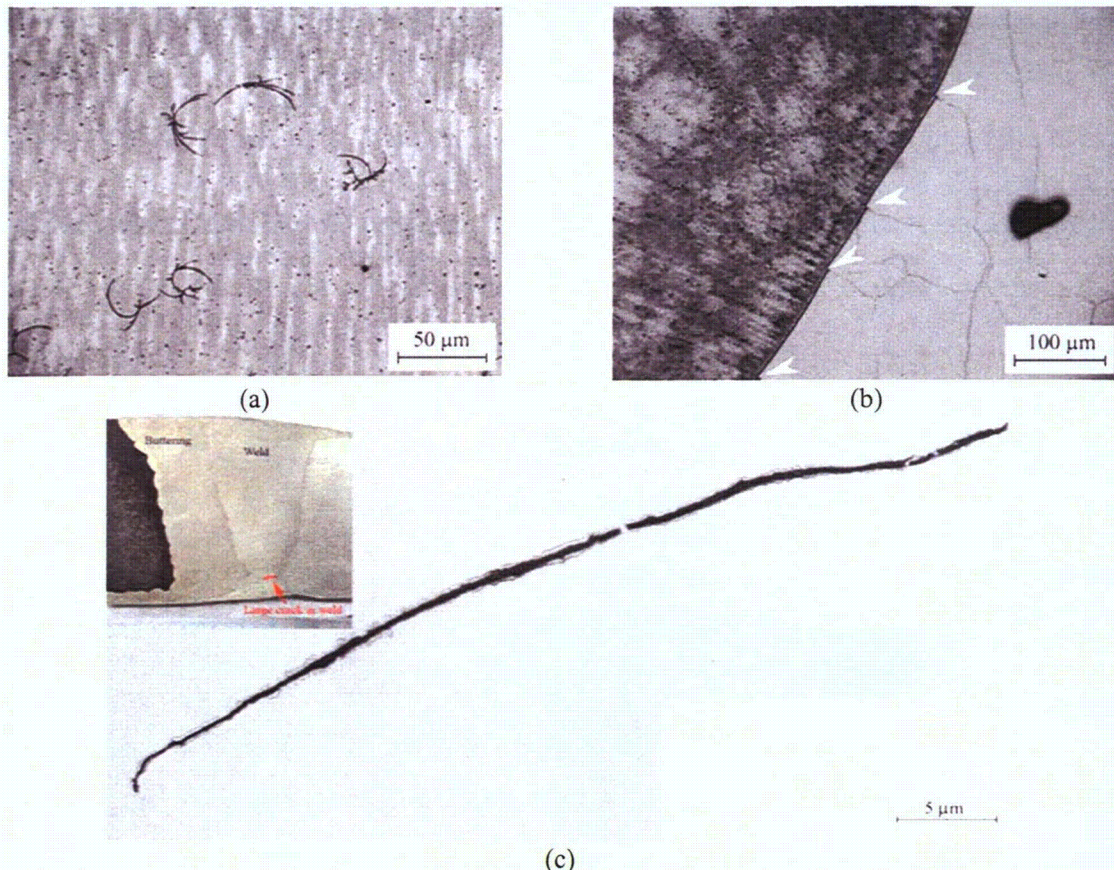


Figure 57. Defects found in the V.C. Summer weld and butter alloys: (a) precipitates in the butter, (b) grain boundary sliding at the weld-pipe interface, and (c) cracks in the weld.

#### 5.3.1.2 Crack Growth Test Facility and Procedure

The CGR tests were conducted in a 5.7-L SS autoclave mounted on an MTS extra high load frame with an MTS 810 control console, and a recirculating water loop. The PWR water is circulated from a

130-L SS storage tank through a high-pressure pump, regenerative heat exchanger, autoclave preheater, test autoclave, ECP cell and preheater, regenerative heat exchanger, and Tescom™ back-pressure regulator, and it is then returned to the storage tank. The PWR water is high purity, containing only ≈1000 ppm B, 2 ppm Li, <10 ppb DO, and ≈2 ppm dissolved hydrogen (≈23 cc/kg). Water is circulated at flow rates of 15–40 mL/min. Water samples are taken periodically to measure pH, resistivity, and DO concentration in the feedwater.

The CGR tests were performed in accordance with ASTM E-647 “Standard Test Method for Measurement of Fatigue Crack Growth Rates” and ASTM E-1681 “Standard Test Method for Determining a Threshold Stress Intensity Factor for Environment-Assisted Cracking of Metallic Materials under Constant Load.” All specimens were fatigue precracked in PWR water at load ratio  $R = 0.3$ , frequency of ≈0.5–2 Hz, and maximum stress intensity factor  $K_{max}$  of 19–24 MPa m<sup>1/2</sup>. After ≈0.3–mm extension,  $R$  was increased incrementally to 0.5, and the loading waveform changed to a slow/fast sawtooth with rise times of 30–300 s. In all tests,  $K_{max}$  was maintained approximately constant by periodic load shedding. After the test, the final crack size was marked by fatigue cycling at room temperature. The specimen was then fractured, and the fracture surfaces of both halves of the specimen were examined by SEM. The final crack length was measured from the SEM images by the 9/8 averaging technique.

To ensure that the experimental data obtained from differing specimen geometry, thickness, and loading conditions can be compared with each other and applied to reactor components, the CGR data were validated in accordance with the specimen size criteria of ASTM E-1681 and E-647. For high-strain-hardening materials with ultimate-to-yield-stress ratio ≥1.3, both requirements allow the use of flow stress defined as  $\sigma_f = (\sigma_{ult} + \sigma_{ys})/2$  rather than the yield stress.

### 5.3.2 Results

#### 5.3.2.1 Crack Growth Rates in PWR Environment

The crack growth data along with the test conditions, resulting stress intensity factors  $K_{max}$ , and experimental and estimated CGRs for the two specimens are given in Tables 14 and 15, respectively. For specimen WCR-01, testing concluded with a constant-load period at  $K_{max} = 23$  MPa·m<sup>1/2</sup>. For specimen BCR-01 the test protocol consisted of four constant load periods at  $K_{max}$  values up to 33 MPa·m<sup>1/2</sup>.

Table 14. Crack growth results for Specimen WCR-01 of Alloy 82 SMA weld in PWR water<sup>a</sup> at 320°C.

Test Period	Test Time, h	Cond., <sup>b</sup> μS/cm	O <sub>2</sub> Conc., <sup>b</sup> ppb	Load Ratio R	Rise Time, s	Down Time, s	Hold Time, s	$K_{max}$ , MPa·m <sup>1/2</sup>	$\Delta K$ , MPa·m <sup>1/2</sup>	CGR <sub>env</sub> , m/s	Estimated CGR <sub>air</sub> , m/s	Crack Length, mm
Pre a	100	23	<10	0.32	1	1	0	24.14	16.42	2.8E-09	1.70E-08	12.289
Pre b	124	23	<10	0.31	0.5	0.5	0	24.14	16.66	4.9E-09	3.52E-08	12.351
Pre c	140	23	<10	0.29	5	5	0	23.18	16.46	1.7E-09	3.19E-09	12.379
Pre d	146	23	<10	0.30	0.25	0.25	0	23.96	16.77	9.3E-09	7.06E-08	12.484
1	258	23	<10	0.50	30	2	0	24.12	12.06	1.4E-10	2.61E-10	12.649
2	380	23	<10	0.51	30	2	0	23.69	11.61	2.1E-10	2.30E-10	12.736
3	523	23	<10	0.50	300	12	0	23.76	11.88	3.2E-11	2.45E-11	12.779
4	593	23	<10	1.00	–	–	–	22.42	0.00	7.5E-11	–	12.789

<sup>a</sup>Simulated PWR water with 2 ppm Li, 1100 ppm B, and 2 ppm dissolved hydrogen (≈23 cc/kg). Measured pH was 6.4.

Table 15. Crack growth data for Specimen BCR-01 of Alloy 182 SMA weld in PWR water<sup>a</sup> at 320°C.

Test Period	Test Time, h	Cond., <sup>b</sup> $\mu\text{S}/\text{cm}$	O <sub>2</sub> Conc., <sup>b</sup> ppb	Load Ratio R	Rise Time, s	Down Time, s	Hold Time, s	K <sub>max</sub> , MPa·m <sup>1/2</sup>	$\Delta K$ , MPa·m <sup>1/2</sup>	CGR <sub>env</sub> , m/s	Estimated CGR <sub>air</sub> , m/s	Crack Length, mm
Pre a	31.0	26	<10	0.30	0.25	0.25	0	21.07	14.75	4.00E-09	4.17E-08	12.046
Pre b	54.0	26	<10	0.30	0.25	0.25	0	21.91	15.34	1.82E-08	4.89E-08	12.269
Pre c	71.0	26	<10	0.31	0.25	0.25	0	22.42	15.47	2.50E-08	5.19E-08	12.407
Pre d	75.0	26	<10	0.31	0.25	0.25	0	21.91	15.12	2.42E-08	2.36E-08	12.573
1	386.0	26	<10	1.00	–	–	–	22.06	–	2.35E-11	–	12.616
2a	389.0	26	<10	0.50	0.25	0.25	0	25.63	12.82	1.49E-08	4.02E-08	12.715
2b	413.0	26	<10	0.50	0.25	0.25	0	25.81	12.91	1.25E-08	4.14E-08	12.905
3	507.0	26	<10	0.50	50	2	0	26.73	13.36	3.16E-10	2.39E-10	13.041
4	839.0	26	<10	1.00	–	–	–	26.97	–	2.34E-11	–	13.057
5	842.0	26	<10	0.30	1	1	0	29.67	20.77	5.04E-08	4.24E-08	13.291
6a	845.0	26	<10	0.50	1	1	0	29.60	14.80	8.18E-09	1.81E-08	13.369
6b	869.0	26	<10	0.50	1	1	0	30.44	15.22	9.17E-09	2.03E-08	13.514
7	939.0	26	<10	0.50	300	12	0	30.60	15.30	2.79E-10	6.92E-11	13.569
8	1,340.0	26	<10	1.00	–	–	–	32.01	–	4.49E-11	–	13.594
9	1,343.0	26	<10	0.30	1	1	0	35.05	24.53	5.73E-08	8.39E-08	13.791
10	1344.0	26	<10	0.50	1	1	0	35.70	17.85	1.44E-08	3.91E-08	13.869
11	1346.0	26	<10	0.50	300	12	0	35.21	17.61	5.78E-10	1.23E-10	13.901
12	1702.0	26	<10	1.00	–	–	–	36.03	–	4.14E-11	–	13.930

<sup>a</sup>Simulated PWR water with 2 ppm Li, 1100 ppm B, and 2 ppm dissolved hydrogen ( $\approx 23$  cc/kg). Measured pH was 6.4.

<sup>b</sup>Represents values in the effluent. Feedwater conductivity was about the same as in the effluent. The ECPs of a Pt electrode and a companion Alloy 600 electrode downstream from the autoclave were  $-620$  and  $-650$  mV (SHE), respectively.

The final crack lengths were determined from metallographic examination of the fractured specimens by SEM. The entire fracture surface of WCR-01 is shown in Fig. 58. The first (green) line designates the region where IG features start to be observed, and the second line (red) shows the final crack extension. The crack front is relatively straight. The observed features are consistent with the testing parameters. These features can be better seen in the higher magnification micrographs of Fig. 59. Figure 59a corresponds to the boxed area in Fig. 58. A mixture of TG and IG fracture is observed during precracking and cyclic loading (Fig. 59a), and a predominantly IG fracture during the final constant load test (Fig. 59c).

Based on the image shown in Fig. 58, the crack extension for the entire test was measured to be 0.782 mm, 2.63 times larger than the value obtained from DC potential measurements. Because of the complex nature of the IG fracture morphology observed in Alloy 182 welds in the PWR environment, the DC potential drop measurements typically underestimate the crack length by a factor of 2 or even 3.<sup>161</sup> The very wavy grain boundary surface, elongated grains, and several unbroken ligaments (Fig. 59) all contribute to the measurement differential between the two techniques. It appears that some IG crack fronts propagated independently of each other, leaving behind unbroken ligaments. Because IG features appeared on the fracture surfaces starting from the early stages of testing, all crack results, including precracking, were corrected by a factor of 2.63. The corrected values of crack length, CGR, and K<sub>max</sub> are listed in Table 14.

Figure 60 shows the fracture surface of specimen BCR-01. For this specimen, a different approach for the testing protocol was undertaken: the constant load periods were separated by mechanical fatigue periods to physically separate the IG regions from the TG regions, and thus to reduce the correction factors. As a result, the DC potential measurement and the direct measurements agreed well, with no correction being needed.

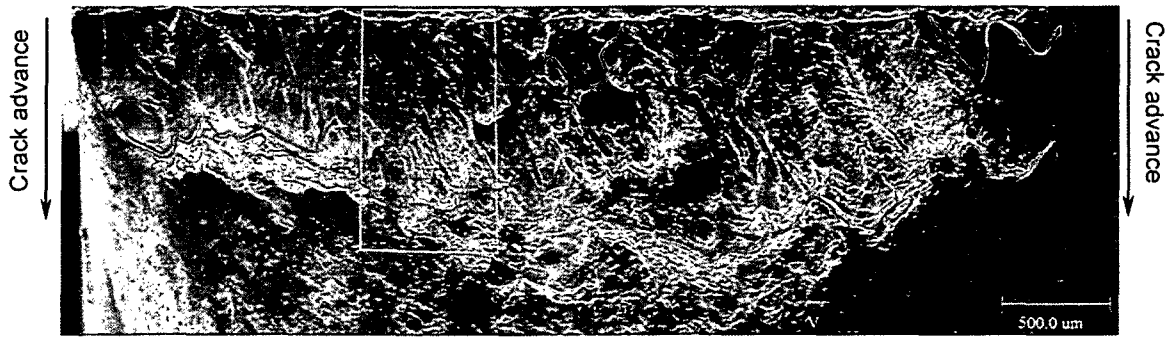


Figure 58. Micrograph of the fracture surface of Specimen WCR-01. Crack advance from top to bottom.

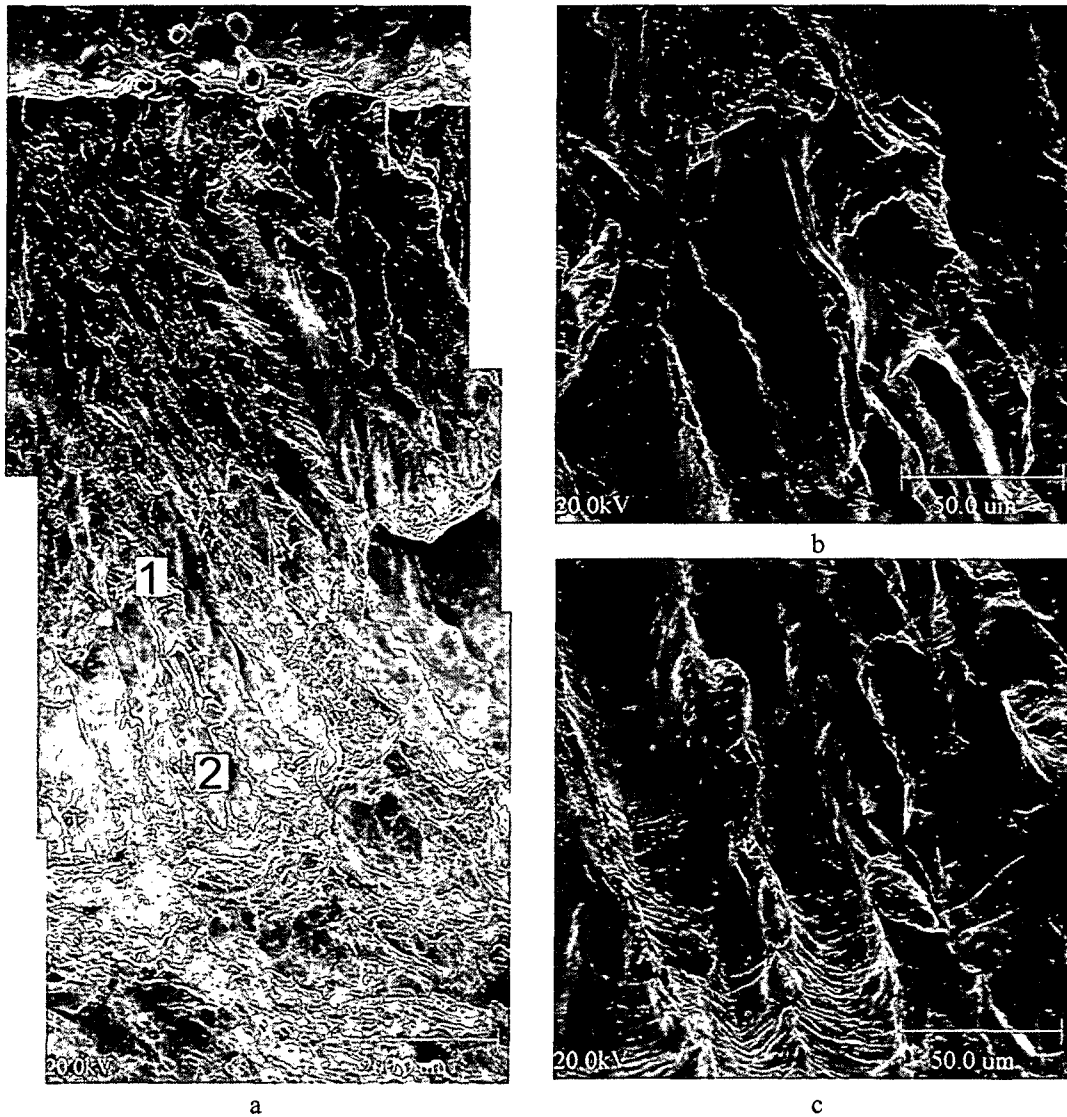


Figure 59. Micrographs of (a) a portion of the fracture surface of specimen WCR-01 (crack advance is from top to bottom) and higher magnification of position (b) 1 and position (c) 2.



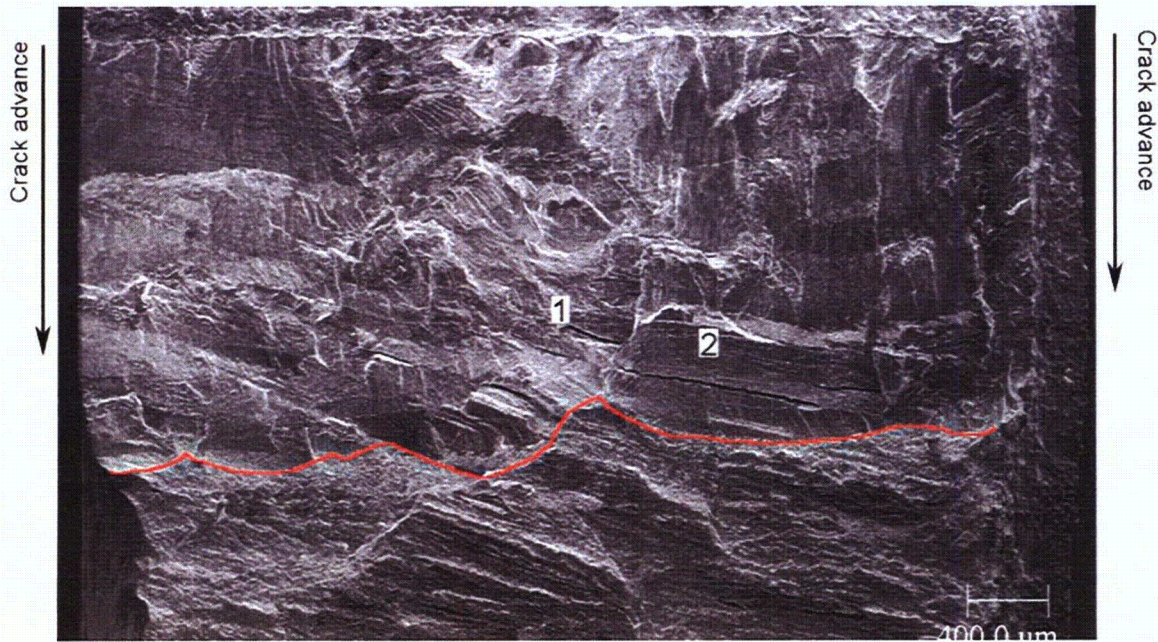


Figure 60. Micrograph of the fracture surface of Specimen BCR-01. Crack advance from top to bottom.

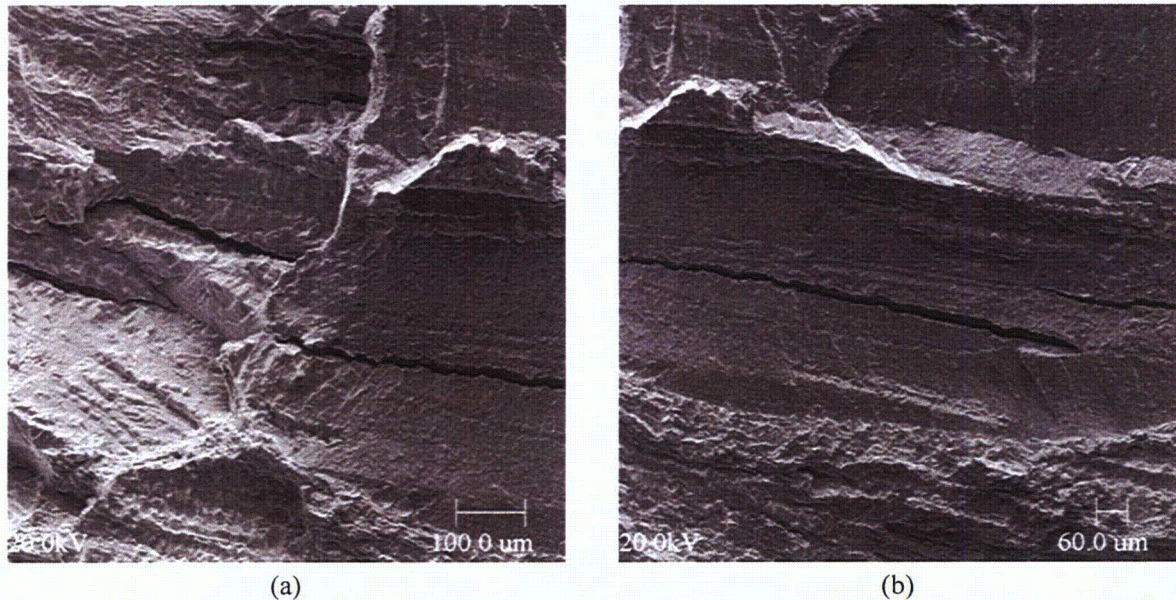


Figure 61. Micrographs of the fracture surface of Specimen BCR-01 at locations (a) 1 and (b) 2 in Fig. 60.

As with the previous example, a fairly straight crack front was obtained (red line in Fig. 60), although the appearance of the front suggests that some pinning occurred, presumably associated with the defects found in these alloys. Figure 61 shows two additional, high-magnification micrographs of the fracture surface taken at locations 1 (Fig. 61a) and 2 (Fig. 61b) in Fig. 60. In both micrographs the IG fracture mode appears to be interrupted at cracks developing across the crack front. The significance of the secondary cracks across the crack front and in a plane normal to the fracture plane is not well understood.

### 5.3.2.2 Crack Growth Rates under Cyclic Loading

Figure 62 shows the CGR rates under cyclic loading for the two specimens, WCR-01 and BCR-01, as a function of the CGRs obtained from Eqs. 29 and 30 for Alloy 600 in air under the same loading conditions. Note that because correlations are not available to estimate cyclic CGRs of Alloy 182/82 weld metal in air, the CGRs for these alloys in PWR environment are compared to those for Alloy 600 in air to establish possible environmental effects on growth rates. Experimental data obtained by Amzallag et al.,<sup>150</sup> Van Der Sluys et al.,<sup>151,152</sup> Lindstrom et al.,<sup>153</sup> and James and Mills<sup>154</sup> are also included in the figure. The results indicate that with the exception of the two V.C. Summer welds (WCR-01 and BCR-01), the CGR data are bound by the rates in air for Alloy 600 (solid line) and eight times those (dotted line). The two V. C. Summer welds appear to be more resistant to fatigue than the laboratory-prepared welds used for obtaining the data from the literature. Ideally in Fig. 62 the data on the weld metals in the PWR environment should be compared with CGRs in air for the weld metals, not Alloy 600. Although the CGRs in the PWR environment are in most cases higher than those in air, much of this difference may not be due to environmental effects, but rather may simply reflect differences in the fatigue crack growth rates of Alloys 182 and 82 compared with that of Alloy 600.

When environmental enhancement occurs, the relative CGRs in the PWR environment compared with those in air should be increasing with decreasing CGRs in air. It is not clear whether all the data of Fig. 62 show this behavior; however, most of the data were obtained under loading conditions where the crack growth is either controlled primarily by mechanical fatigue or, as is the case of James and Mills,<sup>154</sup> obtained at 243°C, a temperature where environmental effects are expected to be small. For the V. C. Summer Alloy 182 specimen, those loading conditions resulting in CGRs less than  $1 \times 10^{-9}$  m/s in air, i.e., load ratios greater than 0.5 and rise times greater than 30 s, appear to have resulted in enhanced CGRs. On the fracture surface, these conditions are expected to correspond to the transition between TG and IG fracture modes.

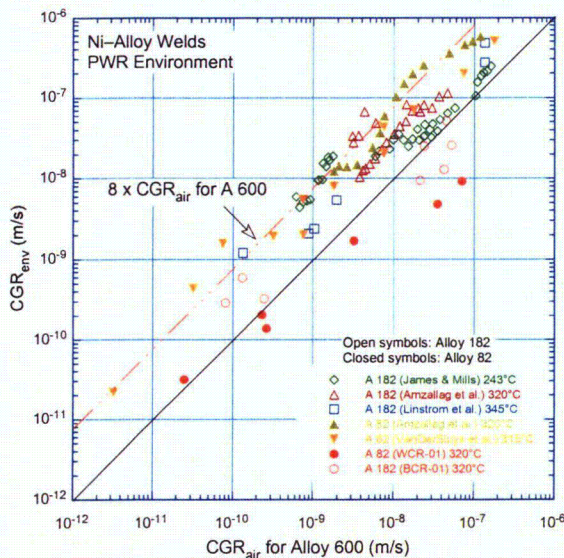


Figure 62.  
Fatigue CGR data for Ni-alloy welds in PWR environment plotted as a function of the growth rate for Alloy 600 in air under the same loading conditions.

### 5.3.2.3 SCC Growth Rates

Although each test period at constant load lasted in excess of 200 h (Tables 14 and 15), the crack advanced quite slowly, hence the relatively small crack length increments. Thus, in the direction of crack

advance, the crack typically grew less than a grain size in the allotted time period. Nevertheless, based on an average size of  $\approx 50 \mu\text{m}$  across and  $\approx 150 \mu\text{m}$  along the length of the columnar grains, it is estimated that across the full width of the sample, the crack advanced along  $\approx 300$  grain boundaries during each constant-load test period in Specimen WCR-01, where the crack front was along the columnar grains, and along  $\approx 45$  grain boundaries in Specimen BCR-01, where the crack front was across the columnar grains. A simple statistical formalism by Alexandreanu and Was<sup>162</sup> was used to analyze how well these samples of boundaries describe the material being tested, i.e., how representative are these samples of the full spectrum of boundary types in the material – the grain boundary character distribution (GBCD). Specifically, the fractional errors associated with the cracking-susceptible random boundaries that would result from boundary populations of these sizes were estimated. Assuming a random boundary fraction of 70%, typical for a weld alloy, the errors for the fractions of (cracked) random boundaries are  $\approx 3.8\%$  in WCR-01 and  $\approx 9.7\%$  in BCR-01. Both of these numbers are comparable with the degree of homogeneity of random boundaries in a Ni-base alloy, thus, as far as GBCD is concerned, no additional benefit can be obtained by considering larger populations of boundaries. Using the same approach, the benefit of doubling the test time, i.e., 400 h instead of 200 h, was also estimated. In such a case, assuming a similar CGR, the population of cracked boundaries in BCR-01, for example, would double to approximately 90 in each constant load period. As a result, the error in the fraction of random boundaries would drop to  $\approx 6.9\%$ . These results were somewhat expected: because random boundaries are quite abundant in Ni-alloy weld, fractional errors cannot be significantly improved by increasing the sample size, i.e., doubling the number of boundaries. From a crack advance viewpoint, it appears unlikely that minor changes, such as 9.7% vs. 6.9% in the population of random boundaries, would impact significantly the observed cracking behavior.

The experimental CGRs resulting from constant load for the two V.C. Summer weld and butter alloys are plotted as a function of applied  $K_{\text{max}}$  in Figs. 63 and 64. Also shown is the disposition curve proposed for Alloy 182 welds in PWR environment.<sup>159</sup> The CGR curve for Ni-alloy welds in PWR environments has been represented by a modified relationship between  $\text{CGR}_{\text{env}}$  (m/s) and stress intensity factor  $K$  ( $\text{MPa m}^{1/2}$ ) originally developed by Scott<sup>155</sup> to describe CGRs in steam generator tubing.

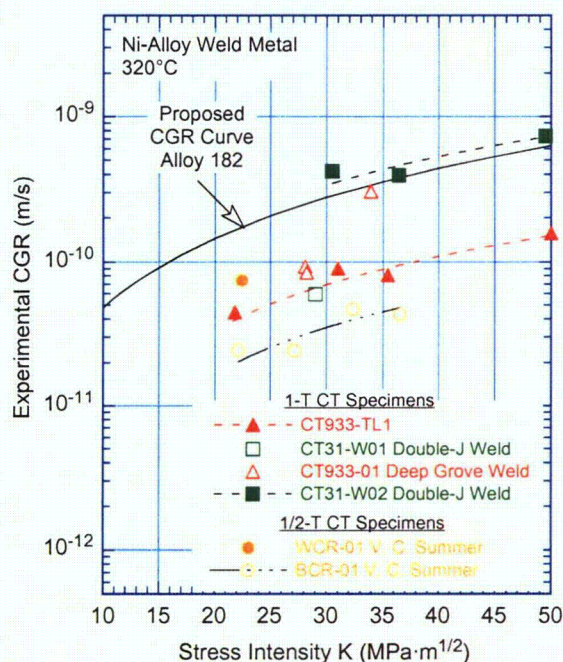


Figure 63.  
Crack growth data for the V. C. Summer alloys and laboratory-prepared welds in PWR environment at 320°C under constant load as a function of applied  $K_{\text{max}}$  compared with the proposed disposition curve for Alloy 182 [Ref. 159].

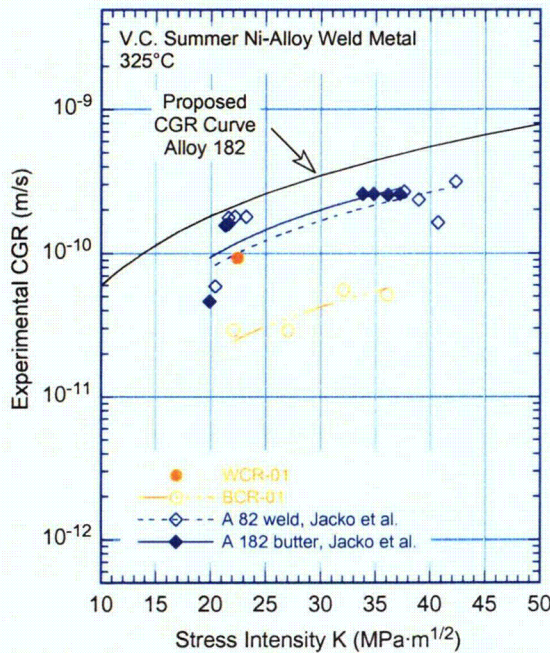


Figure 64.  
Crack growth data in PWR environment under constant load for the V. C. Summer weld alloys obtained in the present study and by Jacko et al. (Ref. 163).

However, unlike the CGR relationship for Alloy 600, the CGR relationship for Ni-alloy welds has no threshold value for K (in Alloy 600 the threshold is  $9 \text{ MPa m}^{1/2}$ ),

$$\text{CGR}_{\text{env}} = A(K)^{1.6}. \quad (33)$$

The term A depends on the material and temperature. The temperature dependence is usually assumed to follow an Arrhenius behavior:

$$A = \alpha \exp \left[ -\frac{Q}{R} \left( \frac{1}{T} - \frac{1}{T_{\text{ref}}} \right) \right], \quad (34)$$

- where
- Q = activation energy for crack growth  
= 130 kJ/mol (31.1 kcal/mol) for Ni-alloy welds
  - R = universal gas constant  
=  $8.314 \times 10^{-3} \text{ kJ/mol}\cdot\text{K}$  ( $1.103 \times 10^{-3} \text{ kcal/mol}\cdot\text{°R}$ )
  - T = absolute operating temperature in K (or °R)
  - $T_{\text{ref}}$  = absolute reference temperature used to normalize the CGR data  
= 598 K (1076.67°R)
  - $\alpha$  =  $1.5 \times 10^{-12}$  at 325°C.

In Fig. 63 the disposition curve was adjusted to 320°C, while in Fig. 64 the CGR data were adjusted to 325°C, in both cases an activation energy of 130 kJ/mole was used. Crack growth data obtained in the present study on laboratory-prepared welds,<sup>161</sup> with a double-J weld design or deep-groove filled weld,\* are also included in Fig. 63. The results show that cracking propagated faster in the V. C. Summer weld specimen WCR-01 having the columnar grains parallel to the crack front than in the butter specimen

1. \_\_\_\_\_

\* Unpublished data, present study.

BCR-01, where the columnar grains were across the crack propagation front. However, weld specimen WCR-01 is Alloy 82, and the butter specimen BCR-01 is Alloy 182; the growth rates for the former are generally a factor of  $\approx 2.5$  lower than those of Alloy 182.<sup>159</sup> Thus, the lower growth rates of BCR-01 vs. WCR-01 may primarily be an effect of orientation. A similar orientation effect is observed for the laboratory-prepared welds.<sup>161</sup> In specimen CT31-W02, which appears to be the most susceptible to crack propagation, the columnar grains are parallel to the crack front.

Figure 64 shows the same V.C. Summer CGR data plotted along with data obtained by Jacko et al. on similar V. C. Summer weld and butter alloys.<sup>163</sup> While the WCR-01 data appear to be consistent with Jacko's measurements, the BCR-01 data are not. The reason(s) for this difference is unclear at this point.



## 6 Summary

---

### 6.1 Environmental Effects on Fatigue $\epsilon$ - $N$ Behavior

The existing fatigue  $\epsilon$ - $N$  data for carbon and low-alloy steels and wrought and cast austenitic stainless steels in LWR environments have been reviewed. The fatigue lives of both carbon and low-alloy steels and austenitic SSs are decreased in LWR environments; the magnitude of the reduction depends on temperature, strain rate, DO level in water, and, for carbon and low-alloy steels, S content in steel. For all steels, environmental effects on fatigue life are significant only when critical parameters (e.g., temperature, strain rate, DO level, and strain amplitude) meet certain threshold values. Environmental effects are moderate, e.g., less than a factor of 2 decrease in life, when any one of the threshold conditions is not satisfied. The threshold values of the critical parameters and the effects of other parameters (such as water conductivity, water flow rate, and material heat treatment) on the fatigue life of the steels are summarized.

Statistical models are presented for estimating the fatigue life of carbon and low-alloy steels and wrought and cast austenitic SSs as a function of material, loading, and environmental parameters. Two approaches are presented for incorporating the effects of LWR environments into ASME Section III fatigue evaluations.

Data available in the literature have been reviewed to evaluate the conservatism in the existing ASME Code fatigue evaluations. Much of the conservatism in these evaluations arises from current design procedures, e.g., stress analysis rules and cycle counting. However, the ASME Code permits alternative approaches, such as finite-element analyses, fatigue monitoring, and improved  $K_e$  factors, all of which can significantly decrease the conservatism in the current fatigue evaluation procedures.

Because of material variability, data scatter, and component size and surface finish, the fatigue life of actual components is different from that of laboratory test specimens under a similar loading history, and the mean  $\epsilon$ - $N$  curves for laboratory test specimens must be adjusted to obtain design curves for components. These design margins are another source of possible conservatism. The factors of 2 on stress and 20 on cycles used in the Code were intended to cover the effects of variables that can influence fatigue life but were not investigated in the tests that provided the data for the curves. Data available in the literature have been reviewed to evaluate the margins on cycles and stress that are needed to account for the differences and uncertainties. The results indicate that the current ASME Code requirements of a factor of 2 on stress and 20 on cycle are quite reasonable, and do not contain excess conservatism that can be assumed to account for the effects of LWR environments. They thus provide appropriate design margins for the development of design curves from mean data curves for small specimens in LWR environments.

### 6.2 Irradiation-Assisted Stress Corrosion Cracking of Austenitic Stainless Steel in BWRs

Slow-strain-rate tensile tests have been completed in high-purity 289°C water on steels irradiated up to  $\approx 3$  dpa in 289°C helium in the Halden Reactor. Susceptibility of the steels to IASCC was determined on the basis of the degree of intergranular fracture surface morphology. At  $\approx 0.4$  dpa, IASCC susceptibility was negligible for all tested heats, with the exception of a 316L-like high-purity alloy that contained 0.003 wt.% C and 0.004 wt.% S. At 0.4 and 1.4 dpa, significant TG fracture was mixed with IG fracture. At 3 dpa, the tendency to TGSCC was negligible, and fracture surface morphology was

either dominantly IG, as in field-cracked core internal components, or dominantly ductile or mixed. This behavior indicates that percent IGSCC determined at  $\approx 3$  dpa is a good measure of IASCC susceptibility.

Excellent resistance to IASCC was observed up to  $\approx 3$  dpa for seven heats of Types 304 and 316 SS that contain very low S concentrations of  $\leq 0.002$  wt.% and for one heat of Type 348 SS that contains 0.005 wt.% S. Susceptibility of Types 304 and 316 steel that contain  $> 0.003$  wt.% S increased drastically. A sufficiently low concentration of S (i.e.,  $< 0.002$  wt.%) is the primary material factor necessary to ensure good resistance to IASCC. At sufficiently low concentrations of S, a high concentration of C is beneficial. However, at S concentrations  $> 0.003$  wt.%, the deleterious effect of S is so dominant that a high concentration of C is not an important factor.

A two-dimensional map was developed in which susceptibility or resistance to IASCC is shown as a function of bulk concentrations of S and C. Data reported in the literature are consistent with the map. The map is helpful to predict relative IASCC susceptibility of Types 304 and 316 SS.

Based on the results of this study, an IASCC model has been developed. The model is based on several key steps known or postulated to occur at the crack-tip grain boundary, i.e., grain-boundary segregation of Ni and S, preferential oxidation of Cr and Fe atoms over Ni atoms by oxygen that diffuses along the grain boundary, formation of a Cr-Fe spinel oxide ahead of the crack tip, formation of Ni- and S-rich thin films and islands at the metal/spinel boundary, and melting or amorphization of the Ni- and S-rich thin films and islands. The model also predicts that the thickness and morphology of the Cr oxide that covers the crack-tip grain boundary strongly influence the rate of oxygen permeation and diffusion along the grain boundary.

Crack growth rate tests have been conducted in BWR environments on austenitic SS weld HAZ specimens that were irradiated to  $\approx 0.75$  dpa at  $\approx 288^\circ\text{C}$  in a helium environment in the Halden boiling heavy water reactor. The specimens were obtained from a Type 304L SS HAZ of the H5 SA weld of the GG reactor core shroud and Type 304 SS HAZ of a laboratory-prepared SMA weld. The materials were tested in two conditions: as-welded and as-welded plus thermally treated for 24 h at  $500^\circ\text{C}$ . For nonirradiated material, under cyclic loading conditions that resulted in predominantly mechanical fatigue (i.e., no environmental enhancement), experimental CGRs for the GG Type 304L weld HAZ were lower than those for the Type 304 SMA weld HAZ. Thermal treatment of the material for 24 h at  $500^\circ\text{C}$  to simulate low-temperature sensitization had little or no effect on mechanical fatigue growth rates.

In the high-DO NWC BWR environment (i.e., with environmental enhancement), the cyclic CGRs of laboratory-prepared Type 304 SS SMA weld HAZ are comparable to those of the GG Type 304L SA weld HAZ. Also, thermal treatment of the material for 24 h at  $500^\circ\text{C}$  had little or no effect on mechanical fatigue growth rates. For both the GG and the laboratory-prepared weld HAZ, irradiation to  $\approx 0.75$  dpa appears to increase the CGRs marginally.

For nonirradiated GG Type 304L weld HAZ, the CGRs under constant load of as-welded and as-welded plus thermally-treated material are comparable. For both conditions, the CGRs are a factor of  $\approx 2$  lower than the NUREG-0313 curve for sensitized SSs in water with 8 ppm DO. The SCC growth rates for the as-welded Type 304 SS SMA weld HAZ were not obtained and those for thermally treated SMA weld HAZ were not valid, e.g., the loading conditions did not meet the  $K/\text{size}$  criterion and fracture plane was at  $45^\circ$  to the stress axis.

Irradiation to  $5.0 \times 10^{20}$  n/cm<sup>2</sup> ( $\approx 0.75$  dpa) increased the growth rates of all SS weld HAZ materials. The CGRs of irradiated HAZ specimens are a factor of 2-5 higher than those predicted by the



NUREG-0313 disposition curve for sensitized SSs in high-DO water. The fracture morphology for irradiated Type 304 weld HAZ is similar to the nonirradiated material, e.g., fracture morphology is IG under environmentally enhanced or SCC conditions, and TG under mechanical fatigue or conditions that show little or no environmental enhancement. Reducing the corrosion potential of the environment decreased the growth rates for all materials that were tested in the BWR environment.

### **6.3 Irradiation-Assisted Cracking of Austenitic Stainless Steel in PWRs**

A comprehensive irradiation experiment in the BOR-60 sodium-cooled breeder reactor is under way to obtain a large number of tensile and disk specimens irradiated under PWR-like conditions at  $\approx 325^\circ\text{C}$  to 5, 10, 20, and 40 dpa. Irradiations to  $\approx 5$ , 10, and 20 dpa at  $\approx 322^\circ\text{C}$  during irradiation cycle BORIS-6 have been completed. After irradiation, 48 tensile specimens and 166 disk specimens were discharged; the SSRT specimens were irradiated to  $\approx 5$  and 10 dpa and TEM disk specimens irradiated to  $\approx 5$ , 10, and 20 dpa. The specimens have been cleaned of sodium and are available for testing.

The available database on void swelling and density change of austenitic SSs was critically reviewed. Irradiation conditions, test procedures, and microstructural characteristics were carefully examined, and key factors that are important to determine the relevance of the database to PWR conditions were evaluated. Most swelling data were obtained from steels irradiated in fast breeder reactors at temperatures  $>385^\circ\text{C}$  and at dose rates that are orders of magnitude higher than PWR dose rates. These data cannot be extrapolated to determine credible void swelling behavior for PWR end-of-life (EOL) or life-extension conditions. A limited amount of swelling data and information on microstructural characteristics are available that were obtained from discharged PWR internals or steels irradiated at temperatures and at dose rates comparable to those of a PWR. Based on that information, swelling in thin-walled tubes and baffle bolts in a PWR is not considered a concern. PWR baffle reentrant corners are most susceptible to high swelling rates, and hence, high swelling at EOL, especially in limited regions where irradiation temperature is high. However, it is considered unlikely that void swelling in a reentrant corner will exceed the threshold level of  $\approx 4\%$  beyond which the swelling rate reaches the steady state rate of  $1\%/dpa$ . This estimation is only preliminary, and a more accurate quantification of maximum temperature of reentrant corners is needed.

### **6.4 Environmentally Assisted Cracking of Alloys 600 and 690 in LWR Water**

The resistance of Ni alloys to EAC in simulated LWR environments is being evaluated. Crack growth tests are being conducted to establish the effects of relevant material, environmental, and loading conditions on the CGRs of Ni alloys and their welds. During the current reporting period, CGR tests were completed in the PWR environment on Alloy 600 from the D-B CRDM nozzle #3 and Alloys 82 and 182 from the nozzle-to-pipe weld of the V. C. Summer reactor. The results are compared with the existing CGR data for Ni alloys and welds to determine the relative susceptibility of these materials to environmentally enhanced cracking under a variety of loading conditions.

Crack growth tests on Alloy 600 removed from the D-B CRDM nozzle #3 were conducted in the PWR environment at  $316^\circ\text{C}$ . The tensile properties, microstructure, and fracture morphology of the nozzle material have also been characterized. The microstructure along the longitudinal plane of the nozzle material is similar to that along the circumferential plane; the grain size varies from 30 to 200  $\mu\text{m}$  with an average value of  $\approx 75 \mu\text{m}$ . The material appears to have good GBC of Cr-rich carbides and a few Ti carbides randomly distributed in the matrix. The tensile strength of the alloy is comparable to the typical value observed for thick-section Alloy 600 products; the average tensile yield and ultimate stress were 274 and 548 MPa, respectively.

For the D-B nozzle Alloy 600, the cyclic CGRs in PWR water show significant environmental enhancement of growth rates. Although the results show considerable scatter, specimen orientation does not seem to have any effect on CGRs. The cyclic CGRs in PWR water at 316°C may be represented by the curve obtained for Alloy 600 in the NWC BWR environment at 289°C. Under constant load, the CGRs of the nozzle alloy are a factor of 4–8 higher than the median curve for Alloy 600. The growth rates correspond to ≈95 percentile of the various data sets used in developing the median curve, i.e., the nozzle material exhibits very high susceptibility to SCC. The material exhibits predominantly IG fracture, even during predominantly mechanical fatigue loading. A TG fracture is observed at the very beginning of the test, i.e., near the machine notch, but, in most cases, it changes to IG fracture when the first grain boundary is encountered.

Crack growth tests on the nozzle-to-pipe weld specimens from the V.C. Summer reactor were conducted in a PWR environment at 320°C. A specimen each from the butter (Alloy 182) and the weld (Alloy 82) has been tested to date. The results indicate that cyclic loading with high load ratios and long rise times preceding the constant-load test initiates IG fracture and ensures a relatively straight crack front. Defects in the form of pores, cracks, and precipitates are present in the V.C. Summer alloys and may impede crack propagation. The fatigue CGRs of both Alloy 82 weld and Alloy 182 butter from the V. C. Summer weld spool piece are significantly lower than those typically observed for these alloys in air. The SCC growth rates of the two alloys are also lower than the proposed CGR curve for nickel-alloy welds. The relative susceptibility of the two alloys, e.g., Alloy 82 weld and Alloy 182 butter, to SCC cannot be determined accurately because they were tested in different orientations.

## References

---

1. Ranganath, S., J. N. Kass, and J. D. Heald, "Fatigue Behavior of Carbon Steel Components in High-Temperature Water Environments," BWR Environmental Cracking Margins for Carbon Steel Piping, EPRI NP-2406, Electric Power Research Institute, Palo Alto, CA, Appendix 3 (1982).
2. Higuchi, M., and K. Iida, "Fatigue Strength Correction Factors for Carbon and Low-Alloy Steels in Oxygen-Containing High-Temperature Water," Nucl. Eng. Des. 129, 293-306 (1991).
3. Katada, Y., N. Nagata, and S. Sato, "Effect of Dissolved Oxygen Concentration on Fatigue Crack Growth Behavior of A533 B Steel in High-Temperature Water," ISIJ Intl. 33 (8), 877-883 (1993).
4. Kanasaki, H., M. Hayashi, K. Iida, and Y. Asada, "Effects of Temperature Change on Fatigue Life of Carbon Steel in High Temperature Water," Fatigue and Crack Growth: Environmental Effects, Modeling Studies, and Design Considerations, PVP Vol. 306, S. Yukawa, ed., American Society of Mechanical Engineers, New York, pp. 117-122 (1995).
5. Nakao, G., et al., "Effects of Temperature and Dissolved Oxygen Content on Fatigue Life of Carbon and Low-Alloy Steels in LWR Water Environment," Fatigue and Crack Growth: Environmental Effects, Modeling Studies, and Design Considerations, PVP Vol. 306, S. Yukawa, ed., American Society of Mechanical Engineers, New York, pp. 123-128 (1995).
6. Higuchi, M., K. Iida, and Y. Asada, "Effects of Strain Rate Change on Fatigue Life of Carbon Steel in High-Temperature Water," Effects of the Environment on the Initiation of Crack Growth, ASTM STP 1298, W. A. Van Der Sluys, R. S. Piascik, and R. Zawierucha, eds., American Society for Testing and Materials, Philadelphia, pp. 216-231 (1997).
7. Iida, K., et al., "Comparison of Japanese MITI Guideline and Other Methods for Evaluation of Environmental Fatigue Life Reduction," Pressure Vessel and Piping Codes and Standards, PVP Vol. 419, M. D. Rana, ed., American Society of Mechanical Engineers, New York, pp. 73-82 (2001).
8. Chopra, O. K., and W. J. Shack, "Effects of LWR Coolant Environments on Fatigue Design Curves of Carbon and Low-Alloy Steels," NUREG/CR-6583, ANL-97/18 (March 1998).
9. Chopra, O. K., and W. J. Shack, "Overview of Fatigue Crack Initiation in Carbon and Low-Alloy Steels in Light Water Reactor Environments," J. Pressure Vessel Technol. 121, 49-60 (1999).
10. Chopra, O. K., and W. J. Shack, "Environmental Effects on Fatigue Crack Initiation in Piping and Pressure Vessel Steels," NUREG/CR-6717, ANL-00/27 (May 2001).
11. Higuchi, M., and K. Iida, "Reduction in Low-Cycle Fatigue Life of Austenitic Stainless Steels in High-Temperature Water," Pressure Vessel and Piping Codes and Standards, PVP Vol. 353, D. P. Jones, B. R. Newton, W. J. O'Donnell, R. Vecchio, G. A. Antaki, D. Bhavani, N. G. Cofie, and G. L. Hollinger, eds., American Society of Mechanical Engineers, New York, pp. 79-86 (1997).
12. Kanasaki, H., et al., "Effect of Strain Rate and Temperature Change on the Fatigue Life of Stainless Steel in PWR Primary Water," Trans. 14th Intl. Conf. on Structural Mechanics in Reactor Technology (SmiRT) 14, Lyon, France, pp. 485-493 (1997).

13. Kanasaki, H., et al., "Fatigue Lives of Stainless Steels in PWR Primary Water," Trans. 14th Intl. Conf. on Structural Mechanics in Reactor Technology 14, Lyon, France, pp. 473–483 (1997).
14. Tsutsumi, K., et al., "Fatigue Life Reduction in PWR Water Environment for Stainless Steels," Assessment Methodologies for Preventing Failure: Service Experience and Environmental Considerations, PVP Vol. 410-2, R. Mohan, ed., American Society of Mechanical Engineers, New York, pp. 23–34 (2000).
15. Tsutsumi, K., et al., "Fatigue Behavior of Stainless Steel under Conditions of Changing Strain Rate in PWR Primary Water," Pressure Vessel and Piping Codes and Standards, PVP Vol. 419, M. D. Rana, ed., American Society of Mechanical Engineers, New York, pp. 135–141 (2001).
16. Higuchi, M., et al., "A Proposal of Fatigue Life Correction Factor  $F_{en}$  for Austenitic Stainless Steels in LWR Water Environments," J. Pressure Vessel Technol., ASME, 125, 403 (2003).
17. Chopra, O. K., "Effects of LWR Coolant Environments on Fatigue Design Curves of Austenitic Stainless Steels," NUREG/CR-5704, ANL-98/31 (1999).
18. Chopra, O. K., "Mechanism and Estimation of Fatigue Crack Initiation in Austenitic Stainless Steels in LWR Environments," NUREG/CR-6787, ANL-01/25 (2002).
19. Gavenda, D. J., P. R. Luebbbers, and O. K. Chopra, "Crack Initiation and Crack Growth Behavior of Carbon and Low-Alloy Steels," Fatigue and Fracture 1, Vol. 350, S. Rahman, K. K. Yoon, S. Bhandari, R. Warke, and J. M. Bloom, eds., American Society of Mechanical Engineers, New York, pp. 243–255 (1997).
20. Miller, K. J., "Damage in Fatigue: A New Outlook," International Pressure Vessels and Piping Codes and Standards: Volume 1 – Current Applications, PVP Vol. 313-1, K. R. Rao and Y. Asada, eds., American Society of Mechanical Engineers, New York, pp. 191–192 (1995).
21. Hickling, J., "Strain-Induced Corrosion Cracking of Low-Alloy Reactor Pressure Vessel Steels under BWR Conditions," Proc. of the Tenth Intl. Symp. on Environmental Degradation of Materials in Nuclear Power Systems–Water Reactors, The Minerals, Metals, and Materials Society, Warrendale, PA, CD-ROM, paper #0156 (2001).
22. Solomon, H. D., R. E. DeLair, and A. D. Unruh, "Crack Initiation in Low-Alloy Steel in High-Temperature Water," Effects of the Environment on the Initiation of Crack Growth, ASTM STP 1298, W. A. Van Der Sluys, R. S. Piascik, and R. Zawierucha, eds., American Society for Testing and Materials, Philadelphia, pp. 135–149 (1997).
23. Solomon, H. D., R. E. DeLair, and E. Tolksdorf, "LCF Crack Initiation in WB36 in High Temperature Water," Proc. of the Ninth Intl. Symp. on Environmental Degradation of Materials in Nuclear Power Systems–Water Reactors, Steve Bruemmer, Peter Ford, and Gary Was, eds., The Minerals, Metals, and Materials Society, Warrendale, PA, pp. 865-872 (1999).
24. Chopra, O. K., and W. J. Shack, "Review of the Margins for ASME Code Fatigue Design Curve – Effects of Surface Roughness and Material Variability," NUREG/CR-6815, ANL-02/39 (2003).

25. Hirano, A., et al., "Effects of Water Flow Rate on Fatigue Life of Carbon Steel in High-Temperature Pure Water Environment," *Assessment Methodologies for Predicting Failure: Service Experience and Environmental Considerations*, PVP Vol. 410-2, R. Mohan, ed., American Society of Mechanical Engineers, New York, pp. 13-18 (2000).
26. Hirano, A., et al., "Effects of Water Flow Rate on Fatigue Life of Ferritic and Austenitic Steels in Simulated LWR Environment," *Pressure Vessel and Piping Codes and Standards - 2002*, PVP Vol. 439, R. D. Rana, ed., American Society of Mechanical Engineers, NY, pp. 143-150 (2002).
27. Hirano, A., et al., "Effects of Water Flow Rate on Fatigue Life of Carbon and Stainless Steels in Simulated LWR Environment," *Pressure Vessel Code and Standards - 2004*, PVP-Vol. 480, American Society of Mechanical Engineers, NY, Paper 2004-2680, pp. 109-119 (2004).
28. Lenz, E., N. Wieling, and H. Muenster, "Influence of Variation of Flow Rates and Temperature on the Cyclic Crack Growth Rate under BWR Conditions," *Environmental Degradation of Materials in Nuclear Power Systems – Water Reactors*, The Metallurgical Society, Warrendale, PA (1988).
29. Amzallag, C., P. Rabbe, G. Gallet, and H. -P. Lieurade, "Influence des Conditions de Sollicitation sur le Comportement en Fatigue Oligocyclique d'Aciers Inoxydables Austénitiques," *Memoires Scientifiques Revue Metallurgie Mars*, pp. 161-173 (1978).
30. Jaske, C. E., and W. J. O'Donnell, "Fatigue Design Criteria for Pressure Vessel Alloys," *Trans. ASME J. Pressure Vessel Technol.* 99, 584-592 (1977).
31. Hale, D. A., et al., "Low Cycle Fatigue Evaluation of Primary Piping Materials in a BWR Environment," GEAP-20244, U.S. Nuclear Regulatory Commission (1977).
32. Chopra, O. K., Chopra, B. Alexandreanu, and W. J. Shack, "Effect of Material Heat Treatment on Fatigue Crack Initiation in Austenitic Stainless Steels in LWR Environments," NUREG/CR-6878, ANL-03/35 (2005).
33. Mehta, H. S., "An Update on the EPRI/GE Environmental Fatigue Evaluation Methodology and its Applications," *Probabilistic and Environmental Aspects of Fracture and Fatigues*, PVP Vol. 386, S. Rahman, ed., American Society of Mechanical Engineers, New York, pp. 183-193 (1999).
34. Wire, G. L., T. R. Leax, and J. T. Kandra, "Mean Stress and Environmental Effects on Fatigue in Type 304 Stainless Steel," *Probabilistic and Environmental Aspects of Fracture and Fatigues*, PVP Vol. 386, S. Rahman, ed., American Society of Mechanical Engineers, New York, pp. 213-228 (1999).
35. Yukawa, S., "Meeting of the Steering Committee for Cyclic Life and Environmental Effects (CLEE)," *Pressure Vessel Research Council*, Columbus, OH (June 1999).
36. Mayfield, M. E., E. C. Rodabaugh, and R. J. Eiber, "A Comparison of Fatigue Test Data on Piping with the ASME Code Fatigue Evaluation Procedure," ASME Paper 79-PVP-92, American Society of Mechanical Engineers, New York (1979).
37. Heald, J. D., and E. Kiss, "Low Cycle Fatigue of Nuclear Pipe Components," *J. Pressure Vessel Technol.* 74, PVP-5, 1-6 (1974).

38. Kooistra, L. F., E. A. Lange, and A. G. Pickett, "Full-Size Pressure Vessel Testing and Its Application to Design," *J. Eng. Power* 86, 419-428 (1964).
39. Scott, P. M., and G. M. Wilkowski, "A Comparison of Recent Full-Scale Component Fatigue Data with the ASME Section III Fatigue Design Curves," *Fatigue and Crack Growth: Environmental Effects, Modeling Studies, and Design Considerations*, PVP Vol. 306, S. Yukawa, ed., American Society of Mechanical Engineers, New York, pp. 129-138 (1995).
40. Hechmer, J., "Evaluation Methods for Fatigue - A PVRC Project," *Fatigue, Environmental Factors, and New Materials*, PVP Vol. 374, H. S. Mehta, R. W. Swindeman, J. A. Todd, S. Yukawa, M. Zako, W. H. Bamford, M. Higuchi, E. Jones, H. Nickel, and S. Rahman, eds., American Society of Mechanical Engineers, New York, pp. 191-199 (1998).
41. Indig, M. E., J. L. Nelson, and G. P. Wozadlo, "Investigation of Protection Potential against IASCC," *Proc. 5th Intl. Symp. on Environmental Degradation of Materials in Nuclear Power Systems - Water Reactors*, D. Cubicciotti, E. P. Simonen, and R. Gold, eds., American Nuclear Society, LaGrange Park, IL, pp. 941-947 (1992).
42. Kanasaki, H., T. Okubo, I. Satoh, M. Koyama, T. R. Mager, and R. G. Lott, "Fatigue and Stress Corrosion Cracking Behavior of Irradiated Stainless Steels in PWR Primary Water," *Proc. 5th Intl. Conf. on Nuclear Engineering*, March 26-30, Nice, France (1997).
43. Kasahara, S., K. Nakata, K. Fukuya, S. Shima, A. J. Jacobs, G. P. Wozadlo, and S. Suzuki, "The Effects of Minor Elements on IASCC Susceptibility in Austenitic Stainless Steels Irradiated with Neutrons," *Proc. 6th Intl. Symp. on Environmental Degradation of Materials in Nuclear Power Systems - Water Reactors*, R. E. Gold and E. P. Simonen, eds., The Minerals, Metals, and Materials Society, Warrendale, PA, pp. 615-623 (1993).
44. Kodama, M., S. Nishimura, J. Morisawa, S. Shima, S. Suzuki, and M. Yamamoto, "Effects of Fluence and Dissolved Oxygen on IASCC in Austenitic Stainless Steels," *Proc. 5th Intl. Symp. on Environmental Degradation of Materials in Nuclear Power Systems - Water Reactors*, D. Cubicciotti, E. P. Simonen, and R. Gold, eds., American Nuclear Society, LaGrange Park, IL, pp. 948-954 (1992).
45. Chung, H. M., W. E. Ruther, J. E. Sanecki, A. G. Hins, and T. F. Kassner, "Effects of Water Chemistry on Intergranular Cracking of Irradiated Austenitic Stainless Steels," *Proc. 7th Intl. Symp. on Environmental Degradation of Materials in Nuclear Power Systems - Water Reactors*, G. Airey et al., eds., NACE International, Houston, pp. 1133-1143 (1995).
46. Jacobs, A. J., G. P. Wozadlo, K. Nakata, T. Yoshida, and I. Masaoka, "Radiation Effects on the Stress Corrosion and Other Selected Properties of Type-304 and Type-316 Stainless Steels," *Proc. 3rd Intl. Symp. Environmental Degradation of Materials in Nuclear Power Systems - Water Reactors*, G. J. Theus and J. R. Weeks, eds., The Metallurgical Society, Warrendale, PA, pp. 673-680 (1988).
47. Garzarolli, F., D. Alter, P. Dewes, and J. L. Nelson, "Deformability of Austenitic Stainless Steels and Ni-Base Alloys," *Proc. 3th Intl. Symp. on Environmental Degradation of Materials in Nuclear Power Systems - Water Reactors*, G. J. Theus and J. R. Weeks, eds., The Metallurgical Society, Warrendale, PA, pp. 657-664 (1988).

48. Garzarolli, F., P. Dewes, R. Hahn, and J. L. Nelson, "Deformability of High-Purity Stainless Steels and Ni-Base Alloys in the Core of a PWR," Proc. 6th Intl. Symp. on Environmental Degradation of Materials in Nuclear Power Systems - Water Reactors, R. E. Gold and E. P. Simonen, eds., The Minerals, Metals, and Materials Society, Warrendale, PA, pp. 607-613 (1993).
49. Fukuya, K., K. Fuji, M. Nakano, N. Nakajima, and M. Kodama, "Stress Corrosion Cracking on Cold-Worked Stainless Steels Irradiated to High Fluence," Proc. 10th Intl. Conf. on Environmental Degradation of Materials in Nuclear Power Systems - Water Reactors, August 5-9, 2001, Lake Tahoe, Nevada, G. S. Was and J. L. Nelson, eds., NACE International CD-ROM.
50. Chung, H. M., W. E. Ruther, J. E. Sanecki, and T. F. Kassner, "Grain-Boundary Microchemistry and Intergranular Cracking of Irradiated Austenitic Stainless Steels," Proc. 6th Intl. Symp. on Environmental Degradation of Materials in Nuclear Power Systems - Water Reactors, R. E. Gold and E. P. Simonen, eds., The Minerals, Metals, and Materials Society, Warrendale, PA, pp. 511-519 (1993).
51. Kodama, M., R. Katsura, J. Morisawa, S. Nishimura, S. Suzuki, K. Asano, K. Fukuya, and K. Nakata, "IASCC Susceptibility of Austenitic Stainless Steels Irradiated to High Neutron Fluence," Proc. 6th Intl. Symp. on Environmental Degradation of Materials in Nuclear Power Systems - Water Reactors, R. E. Gold and E. P. Simonen, eds., The Minerals, Metals, and Materials Society, Warrendale, PA, pp. 583-588 (1993).
52. Fukuya, K., K. Nakata, and A. Horie, "An IASCC Study Using High Energy Ion Irradiation," Proc. 5th Intl. Symp. on Environmental Degradation of Materials in Nuclear Power Systems - Water Reactors, August 25-29, 1991, Monterey, CA, D. Cubicciotti, E. P. Simonen, and R. Gold, eds., American Nuclear Society, La Grange Park, IL, pp. 814-820 (1992).
53. Fukuya, K., S. Shima, K. Nakata, S. Kasahara, A. J. Jacobs, G. P. Wozadlo, S. Suzuki, and M. Kitamura, "Mechanical Properties and IASCC Susceptibility in Irradiated Stainless Steels," Proc. 6th Intl. Symp. on Environmental Degradation of Materials in Nuclear Power Systems - Water Reactors, R. E. Gold, and E. P. Simonen, eds., The Minerals, Metals, and Materials Society, Warrendale, PA, pp. 565-572 (1993).
54. Chung, H. M., W. E. Ruther, J. E. Sanecki, A. G. Hins, and T. F. Kassner, "Stress Corrosion Cracking Susceptibility of Irradiated Type 304 Stainless Steels," in Effects of Radiation on Materials: 16th Int. Symp., ASTM STP 1175, A. S. Kumar, D. S. Gelles, R. K. Nanstad, and T. A. Little, eds., American Society for Testing and Materials, Philadelphia, pp. 851-869 (1993).
55. Cookson, J. M., D. L. Damcott, G. S. Was, and P. L. Anderson, "The Role of Microchemical and Microstructural Effects in the IASCC of High-Purity Austenitic Stainless Steels," Proc. 6th Intl. Symp. on Environmental Degradation of Materials in Nuclear Power Systems - Water Reactors, R. E. Gold, and E. P. Simonen, eds., The Minerals, Metals, and Materials Society, Warrendale, PA, pp. 573-580 (1993).
56. Jacobs, A. J., G. P. Wozadlo, T. Okada, S. Kawano, K. Nakata, S. Kasahara, and S. Suzuki, "The Correlation of Grain Boundary Composition in Irradiated Stainless Steels with IASCC Resistance," Proc. 6th Intl. Symp. on Environmental Degradation of Materials in Nuclear Power Systems - Water Reactors, R. E. Gold and E. P. Simonen, eds., The Minerals, Metals, and Materials Society, Warrendale, PA, pp. 597-604 (1993).

57. Kodama, M., J. Morisawa, S. Nishimura, K. Asano, S. Shima, and K. Nakata, "Stress Corrosion Cracking and Intergranular Corrosion of Austenitic Stainless Steels Irradiated at 323 K," *J. Nucl. Mater.*, 212–215, 1509 (1994).
58. Tsukada, T., and Y. Miwa, "Stress Corrosion Cracking of Neutron Irradiated Stainless Steels," *Proc. 7th Int. Symp. on Environmental Degradation of Materials in Nuclear Power Systems - Water Reactors*, G. Airey et al., eds., NACE International, Houston, pp. 1009–1018 (1995).
59. Tsukada, T., Y. Miwa, H. Nakajima, and T. Kondo, "Effects of Minor Elements on IASCC of Type 316 Model Stainless Steels," *Proc. 8th Int. Symp. on Environmental Degradation of Materials in Nuclear Power Systems - Water Reactors*, Aug. 10-14 (1997, Amelia Island, FL, S. M. Bruemmer, ed., American Nuclear Society, La Grange Park, IL, pp. 795-802 (1997).
60. Katsura, S., Y. Ishiyama, N. Yokota, T. Kato, K. Nakata, K. Fukuya, H. Sakamoto, and K. Asano, "Post-Irradiation Annealing Effects of Austenitic SS in IASCC," *Corrosion 98*, NACE International, Houston, Paper #0132 (1998).
61. Jenssen, A., and L. G. Ljungberg, "Irradiation-Assisted Stress Corrosion Cracking - Postirradiation CERT Tests of Stainless Steels in a BWR Test Loop," *Proc. 7th Intl. Symp. on Environmental Degradation of Materials in Nuclear Power Systems - Water Reactors*, G. Airey et al., eds., NACE International, Houston, pp. 1043–1052 (1995).
62. Jenssen, A., P. Efsing, K. Gott, and P.-O. Andersson, "Crack Growth Behavior of Irradiated Type 304L Stainless Steel in Simulated BWR Environment," CD, *Proc. 11th Intl. Conf. on Environmental Degradation of Materials in Nuclear Power Systems - Water Reactors*, Stevenson, WA, Aug. 10-14 (2003, pp. 1015-1026.
63. Tanaka, Y., S. Suzuki, K. Fukuya, H. Sakamoto, M. Kodama, S. Nishimura, K. Nakata, and T. Kato, "IASCC Susceptibility of Type 304, 304L, and 316 Stainless Steels," *Proc. 8th Int. Symp. on Environmental Degradation of Materials in Nuclear Power Systems - Water Reactors*, S. M. Bruemmer, ed., American Nuclear Society, LaGrange Park, IL, pp. 803-811 (1997).
64. Busby, J. T., and G. S. Was, "Irradiation-Assisted Stress Corrosion Cracking in Model Austenitic Alloys with Solute Additions," CD-ROM, *Proc. 11th Intl. Conf. on Environmental Degradation of Materials in Nuclear Power Systems - Water Reactors*, Stevenson, WA, Aug. 10-14, pp. 995-1014 (2003).
65. Karlsen, T. M., and E. Hauso, "Qualification and Application of Instrumented Specimens for In-Core Studies on Cracking Behavior of Austenitic Stainless Steels," *Proc. 9th Intl. Symp. on Environmental Degradation of Materials in Nuclear Power Systems - Water Reactors*, August 1-5, 1999, Newport Beach, CA, S. Bruemmer, P. Ford, and G. Was, eds., The Metallurgical Society, Warrendale, PA, pp. 951-961 (1999).
66. Garzarolli, F., P. Dewes, R. Hahn, and J. L. Nelson, "In-Reactor Testing of IASCC Resistant Stainless Steels," *Proc. 7th Intl. Symp. on Environmental Degradation of Materials in Nuclear Power Systems - Water Reactors*, G. Airey et al., eds., NACE International, Houston, pp. 1055–1065 (1995).



67. Chung, H. M., W. E. Ruther, J. E. Sanecki, A. G. Hins, N. J. Zaluzec, and T. F. Kassner, "Irradiation-Assisted Stress Corrosion Cracking of Austenitic Stainless Steels: Recent Progress and New Approaches," *J. Nucl. Mater.* 239, 61 (1996).
68. Chung, H. M., R. V. Strain, and W. J. Shack, "Irradiation-Assisted Stress Corrosion Cracking of Model Austenitic Stainless Steel Alloys," in CD-ROM, Proc. 10th Intl. Conf. on Environmental Degradation of Materials in Nuclear Power Systems - Water Reactors, Lake Tahoe, NV (Aug. 2001).
69. Chung, H. M., R. V. Strain, and R. W. Clark, "Irradiation-Assisted Stress Corrosion Cracking of Austenitic Stainless Steel in BWRs," in Environmentally Assisted Cracking in Light Water Reactors, NUREG/CR-4667, Vol. 32, ANL-02/33, Annual Report, Argonne National Laboratory, pp.19-28 (June 2003).
70. Chung, H. M., R. V. Strain, and R. W. Clark, "Irradiation-Assisted Stress Corrosion Cracking of Austenitic Stainless Steel in BWRs," in Environmentally Assisted Cracking in Light Water Reactors, NUREG/CR-4667, Vol. 33, ANL-03/36, Annual Report, Argonne National Laboratory, pp.21-33 (June 2005).
71. Heuer, J. K., P. R. Okamoto, N. Q. Lam, J. F. Stubbins, "Disorder-Induced Melting in Nickel: Implication to Intergranular Sulfur Embrittlement," *J. Nucl. Mater.* 301, 129-141 (2002).
72. Okamoto, P. R., J. K. Heuer, and N. Q. Lam, "Is Segregation-Induced Grain Boundary Embrittlement a Polymorphous Melting Process?" CD-ROM, Proc. 2003 TMS Spring Meeting, March 2-6, 2003, San Diego, California, NACE International, Houston, Texas.
73. Hide, K., T. Onchi, M. Mayazumi, and S. Dumbill, "Correlation of Microstructure and IGSCC Behavior for Irradiated Thermally Sensitized Type 304 Stainless Steels," CD-ROM, Proc. 10th Intl. Conf. on Environmental Degradation of Materials in Nuclear Power Systems - Water Reactors, Aug. 5-9, 2001, Lake Tahoe, Nevada.
74. Onchi, T., K. Dohi, and N. Soneda, "Neutron Fluence Dependent Intergranular Cracking of Thermally Sensitized Type 304 Stainless Steel at 290°C in Inert Gas and in Water," CD-ROM, Proc. 11th Intl. Conf. on Environmental Degradation of Materials in Nuclear Power Systems - Water Reactors, Aug. 10-14, 2003, Stevenson, WA, pp. 1111-1120.
75. Bruemmer, S., and L. Thomas, "Stress Corrosion Crack-Tip Characteristics in Austenitic Stainless Steels Exposed to High-Temperature Water Environments," Handout presented at the International Cooperative Group on Environmentally Assisted Cracking, Kyungju, South Korea, April 2001.
76. Thomas, L., and S. Bruemmer, "Analytical Transmission Microscopy (ATEM) Characterization of Stress Corrosion Cracks in LWR-Irradiated Austenitic Stainless Steel Components," EPRI-1003422, Electric Power Research Institute, Palo Alto, CA (May 2002).
77. Thomas, L., and S. Bruemmer, "Analytical Transmission Microscopy (ATEM) Characterization of Stress Corrosion Cracks in LWR-Irradiated Austenitic Stainless Steel Components," CD-ROM, Proc. 11th Intl. Conf. on Environmental Degradation of Materials in Nuclear Power Systems - Water Reactors, Aug. 10-14, 2003, Stevenson, WA, pp. 1049-1061.

78. Dumbill, S., "Examination of Stress Corrosion Crack Tip Microstructures in Stainless Steel," SKI Report 01:35, Swedish Nuclear Power Inspectorate, (September 2001).
79. Chung, H. M., J.-H. Park, J. E. Sanecki, N. J. Zaluzec, M. S. Yu, and T. T. Yang, "Cracking Mechanism of Type 304L Stainless Steel Core Shroud Welds," Proc. 9th Intl. Symp. on Environmental Degradation of Materials in Nuclear Power Systems - Water Reactors, August 1-5, 1999, Newport Beach, CA, S. Bruemmer, P. Ford, and G. Was, eds., The Metallurgical Society, Warrendale, PA, pp. 973-985 (1999).
80. Chung, H. M., J.-H. Park, W. E. Ruther, J. E. Sanecki, R. V. Strain, and N. J. Zaluzec, "Stress Corrosion Cracking Of Austenitic Stainless Steel Core Internal Welds," Corrosion '99, San Antonio, TX, Paper No. 443 (1999).
81. Chung, H. M., D. L. Perry, and W. J. Shack, "Sulfur in Austenitic Stainless Steel and Irradiation-Assisted Stress Corrosion Cracking," Corrosion 2003, San Diego, CA, Paper No. 3662 (2003).
82. de Barbadillo, J. J., and E. Snape, eds., Proc. Intl. Symposium on Sulfide Inclusions in Steel, November 7-8, 1974, Port Chester, New York, American Society of Metals, Warrendale, PA.
83. Chung, H. M., J. E. Sanecki, and F. A. Garner, "Radiation-Induced Instability of MnS Precipitates and Its Possible Consequences on Irradiation-Induced Stress Corrosion Cracking of Austenitic Stainless Steels," in Effects of Radiation on Materials: 18th Intl. Symp., June 23-25, 1996, Hyannis, MA, ASTM STP 1325, R. K. Nanstad, M. L. Hamilton, A. S. Kumar, and F. A. Garner, eds., American Society for Testing and Material, pp. 647-658 (1999).
84. Ashby, M. F., and F. Spaegen, "A New Model for the Structure of Grain Boundaries: Packing of Polyhedra," Scripta Met. 12, 193 (1978).
85. Bruemmer, S. M., et al., "Critical Issue Reviews for the Understanding and Evaluation of Irradiation-Assisted Stress Corrosion Cracking," EPRI TR-107159, Electric Power Research Institute, Palo Alto, CA (1996).
86. Herrera, M. L., et al., "Evaluation of the Effects of Irradiation on the Fracture Toughness of BWR Internal Components," Proc. ASME/JSME 4th Intl. Conf. on Nucl. Eng. (ICONE-4), Vol. 5, A. S. Rao, R. M. Duffey, and D. Elias, eds., American Society of Mechanical Engineers, New York, pp. 245-251 (1996).
87. Mills, W. J., "Fracture Toughness of Type 304 and 316 Stainless Steels and their Welds," Intl. Mater. Rev. 42, 45-82 (1997).
88. Kanasaki, H., I. Satoh, M. Koyama, T. Okubo, T. R. Mager, and R. G. Lott, "Fatigue and Stress Corrosion Cracking Behaviors of Irradiated Stainless Steels in PWR Primary Water," Proc. 5th Intl. Conf. on Nuclear Engineering, ICONE5-2372, pp. 1-7 (1997).
89. Andresen, P. L., F. P. Ford, S. M. Murphy, and J. M. Perks, "State of Knowledge of Radiation Effects on Environmental Cracking in Light Water Reactor Core Materials," Proc. 4th Intl. Symp. on Environmental Degradation of Materials in Nuclear Power Systems - Water Reactors, NACE, pp. 1.83-1.121 (1990).

90. Jenssen, A., and L. G. Ljungberg, "Irradiation Assisted Stress Corrosion Cracking of Stainless Alloys in BWR Normal Water Chemistry and Hydrogen Water Chemistry," Proc. Sixth Intl. Symp. on Environmental Degradation of Materials in Nuclear Power Systems – Water Reactor, R. E. Gold and E. P. Simonen, eds., Minerals, Metals & Materials Society, pp. 547–553 (1993).
91. Brown, K. S., and G. M. Gordon, "Effects of BWR Coolant Chemistry on the Propensity for IGSCC Initiation and Growth in Creviced Reactor Internals Components," Proc. Third Intl. Symp. on Environmental Degradation of Materials in Nuclear Power Systems – Water Reactor, AIME, pp. 243–248 (1987).
92. Gordon, G. M., and K. S. Brown, "Dependence of Creviced BWR Component IGSCC Behavior on Coolant Chemistry," Proc. 4th Intl. Symp. on Environmental Degradation of Materials in Nuclear Power Systems – Water Reactor, Daniel Cubicciotti, ed., NACE, pp. 14.46–14.61 (1990).
93. Garzarolli, F., D. Alter, and P. Dewes, "Deformability of Austenitic Stainless Steels and Nickel–Base Alloys in the Core of a Boiling and a Pressurized Water Reactor," Proc. Intl. Symp. on Environmental Degradation of Materials in Nuclear Power Systems – Water Reactor, American Nuclear Society, pp. 131–138 (1986).
94. Kodama, M., et al., "IASCC Susceptibility of Austenitic Stainless Steels Irradiated to High Neutron Fluence," Proc. Sixth Intl. Symp. on Environmental Degradation of Materials in Nuclear Power Systems – Water Reactor, R. E. Gold and E. P. Simonen, eds., Minerals, Metals & Materials Society, pp. 583–588 (1993).
95. Kodama, M., et al., "Effects of Fluence and Dissolved Oxygen on IASCC in Austenitic Stainless Steels," Proc. Fifth Intl. Symp. on Environmental Degradation of Materials in Nuclear Power Systems – Water Reactor, American Nuclear Society, pp. 948–954 (1991).
96. Clark, W. L., and A. J. Jacobs, "Effect of Radiation Environment on SCC of Austenitic Materials," Proc. First Intl. Symp. on Environmental Degradation of Materials in Nuclear Power Systems – Water Reactor, NACE, p. 451 (1983).
97. Andresen, P. L., and F. P. Ford, "Irradiation Assisted Stress Corrosion Cracking: From Modeling and Prediction of Laboratory & In-Core Response to Component Life Prediction," Corrosion/95, NACE, Houston TX, Paper No. 419 (1995).
98. Jenssen, A., and L. G. Ljungberg, "Irradiation Assisted Stress Corrosion Cracking of Stainless Alloys in BWR Normal Water Chemistry and Hydrogen Water Chemistry," Proc. Sixth Intl. Symp. on Environmental Degradation of Materials in Nuclear Power Systems – Water Reactor, R. E. Gold and E. P. Simonen, eds., Minerals, Metals & Materials Society, pp. 547–553 (1993).
99. Jenssen, A., and L. G. Ljungberg, "Irradiation Assisted Stress Corrosion Cracking: Post Irradiation CERT Tests of Stainless Steels in a BWR Test Loop," Proc. Seventh Intl. Symp. on Environmental Degradation of Materials in Nuclear Power Systems – Water Reactor, G. Airey et al., eds., NACE, pp. 1043–1052 (1995).
100. Gruber, E. E., and O. K. Chopra, "Crack Growth Rate Test of Austenitic Stainless Steels Irradiated in the Halden Reactor," Environmentally Assisted Cracking in Light Water Reactors, Annual Report, January–December 2002, NUREG/CR-4667 Vol. 33, ANL-03/36, pp. 34-43 (2004).

101. Hazelton, W. S., and W. H. Koo, "Technical Report on Material Selection and Processing Guidelines for BWR Coolant Pressure Boundary Piping, Final Report," NUREG-0313, Rev. 2 (1988).
102. Gruber, E. E., and O. K. Chopra, "Crack Growth Rate Test of Austenitic Stainless Steels Irradiated in the Halden Reactor," Environmentally Assisted Cracking in Light Water Reactors, Annual Report, January-December 2003, NUREG/CR-4667 Vol. 34, ANL-05/17, pp. 32-61 (2005).
103. Angeliu, T. M., P. L. Andresen, E. Hall, J. A. Sutliff, and S. Sitzman, "Strain and Microstructure Characterization of Austenitic Stainless Steel Weld HAZs," Corrosion/2000, NACE, Paper No. 00186 (2000).
104. Angeliu, T. M., P. L. Andresen, J. A. Sutliff, and R. M. Horn, "Intergranular Stress Corrosion Cracking of Unsensitized Stainless Steels in BWR Environments," Proc. Ninth Intl. Symp. on Environmental Degradation of Materials in Nuclear Power Systems - Water Reactor, AIME, pp. 311-318 (1999).
105. Andresen, P. L., T. M. Angeliu, W. R. Catlin, L. M. Young, and R. M. Horn, "Effect of Deformation on SCC of Unsensitized Stainless Steel," Corrosion/2000, NACE, Paper No. 00203 (2000).
106. Andresen, P. L., T. M. Angeliu, L. M. Young, W. R. Catlin, and R. M. Horn, "Mechanism and Kinetics of SCC in Stainless Steels," Proc. Tenth Intl. Symp. on Environmental Degradation of Materials in Nuclear Power Systems - Water Reactor, NACE (2001).
107. Odette, G. R., and G. E. Lucas, "The Effects of Intermediate Temperature Irradiation on the Mechanical Behavior of 300-Series Austenitic Stainless Steels," J. Nucl. Mater. 179-181, pp. 572-576 (1991).
108. Chung, H. M., R. V. Strain, and R. W. Clark, "Slow-Strain-Rate-Tensile Test of Model Austenitic Stainless Steels Irradiated in the Halden Reactor," Environmentally Assisted Cracking in Light Water Reactors Semiannual Report July 2000 - December 2000, NUREG/CR-4667, Vol. 31, ANL-01/09, pp. 22-32 (2002).
109. James, L. A., and D. P. Jones, "Fatigue Crack Growth Correlation for Austenitic Stainless Steels in Air," Proc. Conf. on Predictive Capabilities in Environmentally-Assisted Cracking, PVP Vol. 99, R. Rungta, ed., American Society of Mechanical Engineers, New York, pp. 363-414 (1985).
110. Shack, W. J., and T. F. Kassner, "Review of Environmental Effects on Fatigue Crack Growth of Austenitic Stainless Steels," NUREG/CR-6176, ANL-94/1 (May 1994).
111. Andresen, P. L., "Similarity of Cold Work and Radiation Hardening in Enhancing Yield Strength and SCC Growth of Stainless Steel in Hot Water," Corrosion/02, NACE, Paper No. 02509 (2002).
112. Chopra, O. K., E. E. Gruber, and W. J. Shack, "Fracture Toughness and Crack Growth Rates of Irradiated Austenitic Stainless Steels," NUREG/CR-6826, ANL-03/22 (2003).

113. Chung, H. M., and W. K. Soppet, "Evaluation of Causes and Mechanisms of Irradiation-Assisted Cracking of Austenitic Stainless Steel in PWRs," *Environmentally Assisted Cracking in Light Water Reactors, Annual Report, January-December 2003, NUREG/CR-4667, Vol. 34, ANL-05/17, pp. 63-95 (2005).*
114. Byrne, S., F. A. Garner, S. Fyfe, and I. L. Wilson, "Application of Void Swelling Data to Evaluation of Pressurized Water Reactor Components," *Proc. 10th Intl. Conf. on Environmental Degradation of Materials in Nuclear Power Systems - Water Reactors, NACE/ANS/TMS, Aug. 5-9, 2001, Lake Tahoe, NV.*
115. Edwards, D. J., F. A. Garner, B. A. Oliver, and S. M. Bruemmer, "Microstructural Evaluation of a Cold-Worked 316SS Baffle Bolt Irradiated in a Commercial PWR," *Proc. 10th Intl. Conf. on Environmental Degradation of Materials in Nuclear Power Systems - Water Reactors, NACE/ANS/TMS, Aug. 5-9, 2001, Lake Tahoe, NV.*
116. Thomas, L., and S. Bruemmer, "Analytical Transmission Microscopy (ATEM) Characterization of Stress Corrosion Cracks in LWR-Irradiated Austenitic Stainless Steel Components," *EPR-1003422, Electric Power Research Institute, Palo Alto, CA, May 2002.*
117. Garner, F. A., B. M. Oliver, L. B. Greenwood, D. J. Edwards, S. Bruemmer, and M. L. Grossbeck "Generation and Retention of Helium and Hydrogen in Austenitic Steels Irradiated in a Variety of LWR and Test-Reactor Spectral Environments," *Proc. 10th Intl. Conf. on Environmental Degradation of Materials in Nuclear Power Systems - Water Reactors, NACE/ANS/TMS, Aug. 5-9, 2001, Lake Tahoe, NV.*
118. Fujii, K., K. Fukuya, G. Furutani, T. Torimaru, A. Kohyama, and Y. Katoh, "Swelling in 316 Stainless Steel Irradiated to 53 dpa in a PWR," *Proc. 10th Intl. Conf. on Environmental Degradation of Materials in Nuclear Power Systems - Water Reactors, NACE/ANS/TMS, Aug. 5-9, 2001, Lake Tahoe, NV.*
119. Foster, J. P., D. L. Potter, D. L. Harrod, T. R. Mager, and M. G. Burke, "316 Stainless Steel Cavity Swelling in a PWR," *J. Nucl. Mater. 224, p. 207 (1995).*
120. Allen, T. R., H. Tsai, R. S. Daum, D. L. Porter, J. I. Cole, T. Yoshitake, N. Akasaka, T. Donomae, S. Mizuta, J. Ohta, K. Dohi, and H. Kusanagi, "Effects of Irradiation on the Swelling and Mechanical Properties of 316 Stainless Steel," *Proc. 11th Intl. Conf. on Environmental Degradation of Materials in Nuclear Power Systems - Water Reactors, Aug. 10-14, 2003, Stevenson, WA.*
121. Chung, H. M., R. V. Strain, and W. J. Shack, "Tensile and Stress Corrosion Cracking of Type 304 Stainless Steel Irradiated to Very High Dose," *Nucl. Eng. Design, 208, pp. 221-234 (2001).*
122. Scott, P., "An Analysis of Primary Water Stress Corrosion Cracking in PWR Steam Generators," *Proc. of the Specialists Meeting on Operating Experience with Steam Generators, Brussels, Belgium, pp. 5-6 (1991).*
123. Cattant, F., "Lessons Learnt from the Examination of Tubes Pulled from Electricite de France Steam Generators," *Nucl. Eng. Des. 168, 241-253 (1997).*
124. Diercks, D. R., W. J. Shack, and J. Muscara, "Overview of Steam Generator Tube Degradation and Integrity Issues," *Nucl. Eng. Des. 194, 19-30 (1999).*

125. USNRC Information Notice No. 90-10, "Primary Water Stress Corrosion Cracking (PWSCC) of Inconel 600," Feb. 1990.
126. USNRC Generic Letter 97-01, "Degradation of Control Rod Drive Mechanism and Other Vessel Closure Head Penetrations," April 1, 1997.
127. Economou, J., A. Assice, F. Cattant, J. Salin, and M. Stindel, "NDE and Metallurgical Examination of Vessel Head Penetrations," 3rd Intl. Symp. of Fontevraud, Sept. 12-16, 1994.
128. Robinson, M. R., "Oconee Unit 1 and Unit 3 Reactor Vessel Head Leakage, Cracking of RV Head Penetrations due to Primary Water Stress Corrosion Cracking," presented at the NRC Meeting with the NEI EPRI Material Reliability Program Regarding CRDM Nozzle Cracking Issues, Rockville, MD (April 2001).
129. Frye, C. R., T. Alley, M. L. Arey, Jr., and M. R. Robinson, "Cracking in Alloy 600/182 Reactor Vessel Head Penetrations," PVP-Vol. 437, Service Experience and Failure Assessment Applications ASME 2002, P. S. Lam, ed., American Society of Mechanical Engineers, New York, pp. 171-178 (2002).
130. USNRC Information Notice 2001-05, "Through-Wall Circumferential Cracking of Reactor Pressure Vessel Head Control Rod Driver Mechanism Penetration Nozzle at Oconee Nuclear Station, Unit 3," April 30, 2001.
131. USNRC Bulletin 2001-01, "Circumferential Cracking of Reactor Pressure Vessel Head Penetration Nozzles," Aug. 3, 2001.
132. USNRC Information Notice 2000-17, "Crack in Weld Area of Reactor Coolant System Hot Leg Piping at V. C. Summer," Oct. 18, 2000; Suppl. 1, Nov. 16, 2000; Suppl. 2, Feb. 28, 2001.
133. Jenssen, A., K. Norrgard, J. Lagerstrom, G. Embring, and D. Tice, "Assessment of Cracking in Dissimilar Metal Welds," Proc. of the Tenth Intl. Conf. on Environmental Degradation of Materials in Nuclear Power Systems-Water Reactors, NACE International, Houston, TX (2001).
134. Bennetch, J. I., G. E. Modzelewski, L. L. Spain, and G. V. Rao, "Root Cause Evaluation and Repair of Alloy 82/182 J-Groove Weld Cracking of Reactor Vessel Head Penetrations at North Anna Unit 2," PVP-Vol. 437, Service Experience and Failure Assessment Applications ASME 2002, P. S. Lam, ed., American Society of Mechanical Engineers, New York, pp. 179-185 (2002).
135. USNRC Information Notice 2002-11, "Recent Experience with Degradation of Reactor Pressure Vessel Head," March 12, 2002.
136. USNRC Information Notice 2003-11, "Leakage Found on Bottom-Mounted Instrumentation Nozzles," Aug. 13, 2003; Suppl. 1, Jan. 8, 2004.
137. USNRC Bulletin 2003-02, "Leakage from Reactor Pressure Vessel Lower Head Penetrations and Reactor Coolant Pressure Boundary Integrity," Aug. 21, 2003.
138. Ruther, W. E., W. K. Soppet, and T. F. Kassner, "Corrosion Fatigue of Alloys 600 and 690 in Simulated LWR Environments," NUREG/CR-6383, ANL-95/37 (April 1996).

139. Ruther, W. E., W. K. Soppet, and T. F. Kassner, "Environmentally Assisted Cracking of Alloys 600 and 690 in Simulated LWR Water," *Environmentally Assisted Cracking in Light Water Reactors, Semiannual Report, July 1997–December 1997*, NUREG/CR-4667 Vol. 25, ANL-98/18, pp. 42–75 (Sept. 1998).
140. Ruther, W. E., W. K. Soppet, T. F. Kassner, and W. J. Shack, "Environmentally Assisted Cracking of Alloys 600 and 690 in Simulated LWR Water," *Environmentally Assisted Cracking in Light Water Reactors, Semiannual Report, January 1998–July 1998*, NUREG/CR-4667 Vol. 26, ANL-98/18, pp. 25–32 (March 1999).
141. Ruther, W. E., W. K. Soppet, T. F. Kassner, and W. J. Shack, "Environmentally Assisted Cracking of Alloys 600 and 690 in Simulated LWR Water," *Environmentally Assisted Cracking in Light Water Reactors, Semiannual Report, July 1998–December 1998*, NUREG/CR-4667 Vol. 27, ANL-99/11, pp. 45–54 (October 1999).
142. Soppet, W. K., O. K. Chopra, and W. J. Shack, "Environmentally Assisted Cracking of Alloys 600 and 690 in Simulated LWR Water," *Environmentally Assisted Cracking in Light Water Reactors, Semiannual Report, July 1999–December 1999*, NUREG/CR-4667 Vol. 29, ANL-00/23, pp. 39–45 (November 2000).
143. Soppet, W. K., O. K. Chopra, and W. J. Shack, "Cracking of Nickel Alloys and Welds," *Environmentally Assisted Cracking in Light Water Reactors, Annual Report, January–December 2002*, NUREG/CR-4667 Vol. 33, ANL-03/36, pp. 51–61 (June 2005).
144. Chopra, O. K., W. K. Soppet, and W. J. Shack, "Effects of Alloy Chemistry, Cold Work, and Water Chemistry on Corrosion Fatigue and Stress Corrosion Cracking of Nickel Alloys and Welds," NUREG/CR-6721, ANL-01/07 (April 2001).
145. Cassagne, T. B., and A. Gelpi, "Crack Growth Rate Measurements on Alloy 600 Steam Generator Tubes in Steam and Primary Water," *Proc. of the Fifth Intl. Symp. on Environmental Degradation of Materials in Nuclear Power Systems–Water Reactors*, American Nuclear Society, La Grange Park, IL, pp. 518–524 (1991).
146. Foster, J. P., W. H. Bamford, and R. S. Pathania, "Initial Results of Alloy 600 Crack Growth Rate Testing in a PWR Environment," *Proc. of the Seventh Intl. Symp. on Environmental Degradation of Materials in Nuclear Power Systems–Water Reactors*, NACE International, Houston, TX, pp. 25–39 (1995).
147. Magdowski, R., F. Vaillant, C. Amzallag, and M. O. Speidel, "Stress Corrosion Crack Growth Rates of Alloy 600 in Simulated PWR Coolant," *Proc. of the 8th Intl. Symp. on Environmental Degradation of Materials in Nuclear Power Systems–Water Reactors*, S. M. Bruemmer, ed., American Nuclear Society, La Grange Park, IL, pp. 333–338 (1997).
148. Le Hong, S., C. Amzallag, and A. Gelpi, "Modeling of Stress Corrosion Crack Initiation on Alloy 600 in Primary Water of PWRs," *Proc. of the Ninth Intl. Symp. on Environmental Degradation of Materials in Nuclear Power Systems–Water Reactors*, F. P. Ford, S. M. Bruemmer, and G. S. Was, eds., The Minerals, Metals, and Materials Society, Warrendale, PA, pp. 115–122 (1999).

149. Raquet, O., and G. Santarini, "Stress Corrosion Crack Propagation Rate of Alloy 600 in the Primary Water of PWR Influence of a Cold Worked Layer," Proc. of the Ninth Intl. Symp. on Environmental Degradation of Materials in Nuclear Power Systems–Water Reactors, F. P. Ford, S. M. Bruemmer, and G. S. Was, eds., The Minerals, Metals, and Materials Society, Warrendale, PA, pp. 207–213 (1999).
150. Amzallag, C., G. Baudry, and J. L. Bernard, "Effects of PWR Environment on the Fatigue Crack Growth of Different Stainless Steels and Inconel Type Alloy," Proc. IAEA-Specialists Meeting on Subcritical Crack Growth, NUREG/CP-0044, Vol. 1, pp. 263–294 (1983).
151. Van Der Sluys, W. A., B. A. Young, and D. Doyle, "Corrosion Fatigue Properties on Alloy 690 and some Nickel–Based Weld Metals," in Assessment Methodologies for Preventing Failure: Service Experience and Environmental Considerations, PVP Vol. 410-2, R. Mohan, ed., American Society of Mechanical Engineers, New York, pp. 85–91 (2000).
152. Psaila–Dombrowski, M. J., C. S. Wade, J. M. Sarver, W. A. Van Der Sluys, and P. E. Doherty, "Evaluation of Weld Metals 82, 152, 52, and Alloy 690 Stress Corrosion Cracking and Corrosion Fatigue Susceptibility," Proc. of the 8th Intl. Symp. on Environmental Degradation of Materials in Nuclear Power Systems-Water Reactors, S. M. Bruemmer, ed., American Nuclear Society, La Grange Park, IL, pp. 412–421 (1997).
153. Lindstrom, R., P. Lidar, and J. Lagerstrom, "Crack Growth of Alloy 182 in Simulated Primary Side PWR Environment," Proc. of the 8th Intl. Symp. on Environmental Degradation of Materials in Nuclear Power Systems-Water Reactors, S. M. Bruemmer, ed., American Nuclear Society, La Grange Park, IL, pp. 422–429 (1997).
154. James, L. A., and W. J. Mills, "Fatigue–Crack Propagation Behavior of Wrought Alloy 600 and Weld–Deposited EN82H in an Elevated Temperature Aqueous Environment," in Service Experience, Structural Integrity, Severe Accident, and Erosion in Nuclear and Fossil Plants, PVP Vol. 303, The American Society of Mechanical Engineers, pp. 21–36 (1995).
155. Scott, P. M., "Prediction of Alloy 600 Component Failures in PWR Systems," Proc. of Corrosion'96 Research Topical Symposia, Part 1 – Life Prediction of Structures Subject to Environmental Degradation, NACE, International, Houston, TX, pp. 135–160 (1996).
156. Scott, P. M., and C. Benhamou, "An Overview of Recent Observations and Interpretations of IGSCC in Ni–Base Alloys in PWR Primary Water," Proc. of the 10th Intl. Symp. on Environmental Degradation of Materials in Nuclear Power Systems-Water Reactors, NACE International, Houston, TX (2001).
157. Amzallag, C., S. Le Hong, C. Benhamou, and A. Gelpi, "Methodology used to Rank the Stress Corrosion Susceptibility of Alloy 600 PWR Components," Assessment Methodologies for Preventing Failures: Service Experience and Environmental Considerations, PVP Vol. 410–2, Vol. 2, ASME 2000, R. Mohan, ed., American Society of Mechanical Engineers, New York, pp. 163–170 (2000).
158. White, G. A., J. Hickling, and L. K. Mathews, "Crack Growth Rates for Evaluating PWSCC of Thick–Wall Alloy 600 Material," Proc. of the 11th Intl. Symp. on Environmental Degradation of Materials in Nuclear Power Systems-Water Reactors, NACE International, Houston, TX, pp. 166–179 (2003).



159. White, G., J. Hickling, and C. Harrington, MRP Development of Crack Growth Rate Disposition Curves for Primary Water Stress Corrosion Cracking (PWSCC) of Thick-Section Alloy 600 Components and Alloy 82, 182 and 132 Weldments, EPRI International PWSCC of Alloy 600 Conference, Santa Ana Pueblo, NM, March 7-10, 2005.
160. Alexandreanu, B., and G. S. Was, "Grain Boundary Deformation-Induced Intergranular Stress Corrosion Cracking of Ni-16Cr-9Fe in 360°C Water," *Corrosion* 59 (8), pp. 705-720 (2003).
161. Alexandreanu, B., O. K. Chopra, and W. J. Shack, "Cracking of Nickel Alloys and Welds," Environmentally Assisted Cracking in Light Water Reactors, Annual Report, January–December 2003, NUREG/CR-4667 Vol. 34, ANL-05/17, pp. 67-98 (2005).
162. Alexandreanu, B., and G. S. Was, "A Priori Determination of the Sampling Size for Grain Boundary Character Distribution and Grain Boundary Degradation Analysis," *Philosophical Magazine A* 81 (8), pp. 1951–1965 (2001).
163. Jacko, R. J., R. E. Gold, G. V. Rao, K. Koyama, and A. Kroes, "Results of Accelerated SCC Testing of Alloy 82, Alloy 182 and Alloy 52M Weld Metals," presented at The Vessel Penetration Inspection, Crack Growth and Repair Conference, Oct. 2, 2003, Gaithersburg, MD.



<b>NRC FORM 335</b> (9-2004) NRCMD 3.7  <p style="text-align: center;"><b>BIBLIOGRAPHIC DATA SHEET</b>          (See instructions on the reverse)</p>	<b>U. S. NUCLEAR REGULATORY COMMISSION</b>  1. REPORT NUMBER  NUREG/CR-4667. Vol. 35 ANL-05/31				
2. TITLE AND SUBTITLE  Environmentally Assisted Cracking in Light Water Reactors, Annual Report, January-December 2004	3. DATE REPORT PUBLISHED <table border="1" style="width: 100%;"> <tr> <td style="text-align: center;">MONTH</td> <td style="text-align: center;">YEAR</td> </tr> <tr> <td style="text-align: center;">November</td> <td style="text-align: center;">2006</td> </tr> </table> 4. FIN OR GRANT NUMBER Y6388	MONTH	YEAR	November	2006
MONTH	YEAR				
November	2006				
5. AUTHOR(S)  B. Alexandreanu, O. K. Chopra, H. M. Chung, E. E. Gruber, W. K. Soppet, and W. J. Shack	6. TYPE OF REPORT Technical  7. PERIOD COVERED (Inclusive Dates)				
8. PERFORMING ORGANIZATION - NAME AND ADDRESS (If NRC, provide Division, Office or Region, U.S. Nuclear Regulatory Commission, and mailing address; if contractor, provide name and mailing address.)  Argonne National Laboratory 9700 South Cass Avenue Argonne, IL 60439					
9. SPONSORING ORGANIZATION - NAME AND ADDRESS (If NRC, type "Same as above"; if contractor, provide NRC Division, Office or Region, U.S. Nuclear Regulatory Commission, and mailing address.)  Division of Fuel, Engineering & Radiological Research Office of Nuclear Regulatory Research U.S. Nuclear Regulatory Commission Washington, DC 20555-0001					
10. SUPPLEMENTARY NOTES W. H. Cullen, Jr., NRC Project Manager					
11. ABSTRACT (200 words or less)  This report summarizes work performed from January to December 2004 by Argonne National Laboratory on fatigue and environmentally assisted cracking in light water reactors. Topics include: (a) environmental effects on fatigue crack initiation in carbon and low-alloy steels and austenitic stainless steels (SSs), (b) irradiation-assisted stress corrosion cracking (IASCC) of austenitic SSs in boiling water reactors, (c) causes and mechanisms of irradiation-assisted cracking of austenitic SS in pressurized water reactors, and (d) cracking in Ni alloys and welds. The existing fatigue strain vs. life data are used to establish the effects of various material and loading parameters, such as steel type, material heat treatment, strain range, strain rate, temperature, dissolved-oxygen level in water, and flow rate, on the fatigue lives of the steels. A two-dimensional map of bulk S and C contents is presented to show the range in which austenitic SSs are either susceptible or resistant to IASCC. Based on the results of this study, an IASCC model has been proposed. Crack growth rate data are presented on Types 304L and 304 SS weld heat affected zone specimens before and after they were irradiated to a fluence of $\approx 0.75$ dpa. The effects of material composition, irradiation, and water chemistry on growth rates are discussed. Crack growth rate (CGR) data obtained in the pressurized water reactor environment are also presented for Alloy 600 removed from the control rod drive mechanism nozzle #3 of the Davis-Besse reactor and Alloys 182 and 82 from the vessel nozzle-to-pipe weld of the V. C. Summer reactor. The experimental CGRs under cyclic and constant load are compared with the existing CGR data for Alloy 600 to determine the relative susceptibility of these alloys to environmentally enhanced cracking.					
12. KEY WORDS/DESCRIPTORS (List words or phrases that will assist researchers in locating this report.)  Fatigue Crack Initiation Crack Growth Rate Irradiation-Assisted Stress Corrosion Cracking Radiation-Induced Segregation Stress Corrosion Cracking Nickel Alloys	13. AVAILABILITY STATEMENT unlimited  14. SECURITY CLASSIFICATION (This Page) unclassified  (This Report) unclassified  15. NUMBER OF PAGES  16. PRICE				



Federal Recycling Program